UC Santa Cruz
UC Santa Cruz Electronic Theses and Dissertations

Title

Phase-Doppler Interferometry: Characterization and Emerging Applications

Permalink

https://escholarship.org/uc/item/2df8w1zt

Author

Leandro, Mason Douglas

Publication Date

2023

Peer reviewed|Thesis/dissertation

eScholarship.org Powered by the California Digital Library
University of California

UNIVERSITY OF CALIFORNIA
SANTA CRUZ

PHASE-DOPPLER INTERFEROMETRY: CHARACTERIZATION AND EMERGING APPLICATIONS

A dissertation submitted in partial satisfaction
of the requirements for the degree of

DOCTOR OF PHILOSOPHY

in

EARTH SCIENCES

by

Mason Douglas Leandro

September 2023

The Dissertation of Mason Douglas Leandro is approved:

Professor Patrick Chuang, Chair

Professor Nicole Feldl

William Bachalo, Ph.D.

Jan Kazil, Ph.D.

Peter Biehl
Vice Provost and Dean of Graduate Studies

Copyright © by

Mason Douglas Leandro

2023

Table of Contents

List of Figures **v**

List of Tables **xvii**

Abstract **xviii**

Dedication **xxi**

Acknowledgments **xxii**

1 Introduction **1**

1.1 Aircraft Observations Used in this Study 7

2 An automated method for probe volume diameter characterization in phase-Doppler interferometry **9**

2.1 Introduction 10
  2.1.1 Theoretical Framework 10
  2.1.2 Deviations from Theoretical Behavior 14
2.2 Applications of Standard Algorithm 18
  2.2.1 Examples from Laboratory Data 18
  2.2.2 Examples from Flight Data 20
2.3 Algorithm with Gate Chop and Short Gate Events 23
  2.3.1 Accounting for Gate Chop 23
  2.3.2 Accounting for Short Gates 24
  2.3.3 Examples from Flight data 26
2.4 Variability in Probe Volume Diameter 29
2.5 Error Analysis 33
  2.5.1 Artificially-generated Data 33
  2.5.2 Accuracy of Methods 34
2.6 Conclusions 37

3 A Novel Technique to Characterize Phase-Doppler Interferometer Probe Volume Width from Laboratory Measurements 39
3.1 Introduction 40
3.2 Theoretical Calculations 42
3.3 Experimental Methods 45
  3.3.1 Overall Approach 45
  3.3.2 Measurement Technique 47
3.4 Results and Discussion 49
  3.4.1 Laboratory measurements 49
  3.4.2 Application to Aircraft Measurements 55
3.5 Conclusions 59

4 Particulate Matter Emissions from Cooling Tower Drift Droplets 61
4.1 Introduction 62
4.2 Methods 66
  4.2.1 Instrumentation and Deployment 66
  4.2.2 Estimation of PM Emissions 68
4.3 Results and Discussion 72
  4.3.1 Plume Measurements 72
  4.3.2 Environmental Conditions During Sampling 74
  4.3.3 Comparison with Previous Studies 78
  4.3.4 Drift Eliminator Efficiency 80
  4.3.5 PM Emissions from Drift 81
4.4 Summary and Conclusions 85

5 Summary and Conclusions 87

List of Figures

1.1 Image of a phase-Doppler interferometer. 3

1.2 Diagram of the signal measured by a detector when a drop transits the measurement region. Top panel shows the intersection of the two beams, middle panel shows a cross-section of the intersecting beams, and bottom panel shows the time-varying intensity measured by a single detector. . 5

1.3 PDI effective sample area. Angle in the vertical axis is due to the collection angle in the receiver. 6

2.1 Vertical cross section of the intersecting lasers taken parallel to the direction of travel (i.e., an end view of the measurement region). The beam is most intense in the center and decreases in intensity moving radially away from the center. A population of a) large drops and b) small drops passes through the measurement region from left to right with different trajectories (blue dotted lines). A red "X" depicts a situation in with a drop is not detected and the red dashed line represents the detectable diameter of the laser for each drop size, illustrating the functional dependence of D_{beam} on d. 11

2.2 Cross section of the measurement region with six drops transiting the probe volume from left to right at different locations. The schematic illustrates that the $l_{transit}$ distribution will be strongly weighted in favor of $l_{transit}$ close to the maximum possible value, $D_{transit}$. The theoretical probability distribution is given by Eq. 2.1. D_{beam} is the desired dimension of the measurement region, and is obtained assuming $D_{transit} = D_{beam}$. 12

2.3 Theoretical a) PDF and b) CDF of $l_{transit}$ given by Eqs. 2.1 and 2.2, respectively, plotted as solid line, where the specified view volume diameter is 100 µm (dashed vertical line). 13

2.4 Time-varying intensity and gate state for three drops traversing the probe volume for a) an idealized case and b) a case with gate chop and short gate events. Each top panel represents the time-varying intensity as measured by and individual detector and each bottom panel represents the gate state, with a value of 0 corresponding to the gate being closed and a value of 1 corresponding to the gate being open. The gate time of each event is annotated in blue and the inter-occurrence time between each event is annotated in red. 15

2.5 Probability distribution of transit lengths which displays bimodality due to gate chop and/or short gate for 16.9 µm $\leq d <$ 18.9 µm. Data displayed is from the Nov-10 2008 flight of the VOCALS-REx field campaign. 16

2.6 Flowchart describing our recommended pathway for determining $D_{beam}(d)$. 17

2.7 Cumulative distribution of $l_{transit}$ for each d bin used to determine $D_{beam}(d)$. Data was collected in a laboratory setting using a conical spray. Drop size bins increase from left-to-right and top-to-bottom. Black dots represent the measured cumulative distribution of $l_{transit}$ for each bin. Solid white line represents fitted curve and dashed white line represents D_{beam} for each d bin. Colored background in each plot represents relative frequency of drops for each bin. Of the $\sim 4.3 \times 10^4$ drops measured, $\sim 95.4\%$ were used for $D_{beam}(d)$ characterization. 19

2.8 Determined $D_{beam}(d)$ relationship for data collected in a laboratory setting using a conical spray. Each point is derived from a single panel in Fig 2.7. Symbol colors represent relative frequency of drops for each bin. Of the $\sim 4.3 \times 10^4$ drops measured, $\sim 95.4\%$ were used for $D_{beam}(d)$ characterization. Black dashed line represents the theoretical fit to data. 20

2.9 Cumulative distribution of $l_{transit}$ for each d bin used to determine D_{beam}. Data was collected on July-21, 2008, during the POST field campaign. Drop size bins increase from left-to-right and top-to-bottom. Black dots represent the measured cumulative distribution of $l_{transit}$ for each bin. Solid white line represents fitted curve and dashed white line represents D_{beam} for each bin. Colored background in each plot represents relative frequency of drops for each bin. Of the $\sim 1.5 \times 10^6$ drops measured, $\sim 97.5\%$ were used for $D_{beam}(d)$ characterization. 21

2.10 Determined $D_{beam}(d)$ relationship for data collected on July-17, 2008, during the POST field campaign. Each point is derived from a single panel in Fig 2.9. Symbol colors represent relative frequency of drops for each bin. Of the $\sim 1.5 \times 10^6$ drops measured, $\sim 97.5\%$ were used for $D_{beam}(d)$ characterization. Black dashed line represents the theoretical fit to data. 22

2.11 Probability distribution of inter-occurrence time for various narrow drop size ranges. Vertical black dashed line represents the threshold to identify gate chop events. Data displayed is from the Nov-10 2008 flight of the VOCALS-REx field campaign. 24

2.12 Theoretical a) PDF and b) CDF of $l_{transit}$ with varying levels of α, plotted as solid line, where the specified view volume diameter is 100 µm (dashed vertical line). 26

2.13 Cumulative distribution of $l_{transit}$ for each d bin used to determine D_{beam}. Data was collected on November-10, 2008, during the VOCALS-REx field campaign. Instrument encountered frequent gate chop and short gate events during this campaign. Drop size bins increase from left-to-right and top-to-bottom. Black dots represent the measured cumulative distribution of $l_{transit}$ for each bin. Solid white line represents fitted curve and dashed white line represents D_{beam} for each bin. Colored background in each plot represents relative frequency of drops for each bin. $\sim 2.9 \times 10^6$ drops were recorded, with 95.5% of data used for $D_{beam}(d)$ characterization. 28

2.14 Determined $D_{beam}(d)$ relationship for data collected on November-10, 2008, during the VOCALS-REx field campaign. Each point is derived from a single panel in Fig 2.13. Symbol colors points represent relative frequency of drops for each bin. $\sim 2.9 \times 10^6$ drops were recorded, with 95.5% of data used for $D_{beam}(d)$ characterization. Black dashed line represents the theoretical fit to data. 29

2.15 Daily variability in $D_{beam}(d)$ during the VOCALS-REx field campaign. Cooler colors represent days earlier in the campaign and warmer colors represent days later in the campaign. 31

2.16 Daily variability in $D_{beam}(d)$ during the MASE field campaign. Cooler colors represent days earlier in the campaign and warmer colors represent days later in the campaign. 31

2.17 Daily variability in $D_{beam}(d)$ during the POST field campaign. Cooler colors represent days earlier in the campaign and warmer colors represent days later in the campaign. 32

2.18 Target function chosen to generate artificial data set used to evaluate robustness and accuracy of methodology. K_0 and K_1 (Eq. 2.3) were chosen such that the minimum detectable drop size is 2 µm and D_{beam} reaches a value of 500 µm at a drop size of 100 µm. 34

2.19 Results of methodology for determining probe volume diameter with random error introduced to each variable, displayed as % error from the target, D_{target}. Beige line and envelope represents the case where 4% error is introduced in $l_{transit}$, blue line and envelope represents the case where 20% error is introduced in d, and red line and envelope represents the case where 4% is introduced in $l_{transit}$ and 20% error is introduced in d. Solid lines represent the mean from all 100 simulations and the envelope surrounding each line displays the range of outcomes for the 100 simulations. 35

2.20 Percent error from the target function with various levels of proportional error applied to d and $l_{transit}$ for a) no gate chop or short gate events, b) 25% gate chop events and 25% short gate events. Red represents an overestimate of D_{beam} and blue represents an underestimate of D_{beam}. Black contour lines represent percent error from the target in 1% intervals and grey contour lines represent percent error from the target in 0.2% intervals for values $< 0\%$ and 0.5% intervals for values $> 0\%$. . . . 36

3.1 Diagram illustrating how a slit aperture is used to limit the spatial extent at which drops may be detected. The drop in a) transits the probe volume near the center of the intersecting beams and scattered light is allowed to pass through the aperture and the drop is detected. The drop in b) transits the probe volume further from the center of the intersecting beams and scattered light is blocked by the aperture and the drop is not detected. 41

3.2 Intersection of two beams in the defined coordinate system. Two identical beams intersect each other at the origin of the coordinate system. Each beam axis is on the x-z plane with each respective beam intersecting the x-axis at an angle of φ and $-\varphi$. Using this coordinate system, the fringe plane is parallel to the x-y plane and drops transit the probe volume in the z-dimension. 43

3.3 Intensity distribution of the effect sample area of a PDI. Black dashed lines represent contours of intensity in 10% intervals. Red dashed lines represent arbitrary aperture boundaries. 45

3.4 Probe Volume Scanner schematic displaying key components. 48

3.5 Diagram showing the raster pattern performed by the Scanner relative to the PDI sample area. Blue dotted line and arrows represent the pathway taken by the Scanner. 49

3.6 Time series of data rate measured by a PDI instrument as a percentage of MDG frequency for one scan leg. For this scan, the MDG was projecting a stable stream of 191 µm drops. Red points represent times when the measured data rate of the PDI was below 50% of f_{MDG} and green points represent times when the measured data rate of the PDI was above 50% of f_{MDG}. Vertical dotted lines represent the time stamps associated with the stream entering and exiting the probe volume according to our methods. 50

3.7 Time series of retrieved drop intensities from a single scan on Channel 2. Each "spike" is a single transit across the view volume, i.e., the width of each spike is a separate determination of W. 51

3.8 Measured and fitted relationship between W and I_{max} for Channel 1. Fitted relationship was obtained by performing piecewise linear regression with the boundary point set to 150 mV. 52

3.9 Measured and fitted relationship between W and I_{max} for Channel 2. Red dashed line represents the best fit to observations using Eq. 3.6. Blue points and dashed line represents interpolated values based on the red fitting and I_{max} for the smallest detectable drop. 53

3.10 Bivariate histogram of drop counts in drop size-scattering intensity space for Channel 1 for data collected of the June 15, 2023, flight of the SCILLA field campaign. Red points represent the 99^{th} percentile for each d bin and red dashed line represent the best fit 2^{nd} degree polynomial to the points. 56

3.11 Bivariate histogram of drop counts in drop size-scattering intensity space for Channel 2 for data collected of the June 15, 2023, flight of the SCILLA field campaign. Red points represent the 99^{th} percentile for each d bin and red dashed line represent the best fit 2^{nd} degree polynomial to the points. 57

3.12 PDI-measured number concentration for each respective channel averaged over the June 15, 2023, flight of the SCILLA field campaign. Vertical dashed lines represent the upper and lower bounds for each respective channel and the shaded area represents the overlap region. Upper boundaries were determined as the drop size in which I_{max} reaches saturation at 1000 mV in Figs. 3.10 and 3.11. Lower boundaries were determined estimated as 4 µm and 35µm for Channels 1 and 2, respectively, from $D_{beam}(d)$ analysis. 58

4.1 Schematic of an induced-draft counter flow cooling tower. 64

4.2 Bird's-eye view of idealized positions sampled over a cooling tower. Each position, denoted P1-P9, is assumed to represent the emissions for the area in which that position is bounded by dashed lines. 70

4.3 Radial dependence of measured properties for Tower 1. Color bars and corresponding colored points represent the frequency of droplets encountered at each position, for each tower, with N total droplets observed at each tower. Error bars in the first row represent ± one standard deviation in V_{up} and the solid line represents a 4^{th}-degree polynomial fit to the points. Error bars in the second row represent the 25^{th} and 75^{th} percentiles of median volume diameter at each position. Error bars in the third and fourth rows represent error in liquid water content and number concentration, respectively, relating to Poisson counting uncertainty for each position. 72

4.4 Radial dependence of measured properties for Tower 2. Color bars and corresponding colored points represent the frequency of droplets encountered at each position, for each tower, with N total droplets observed at each tower. Error bars in the first row represent ± one standard deviation in V_{up} and the solid line represents a 4^{th}-degree polynomial fit to the points. Error bars in the second row represent the 25^{th} and 75^{th} percentiles of median volume diameter at each position. Error bars in the third and fourth rows represent error in liquid water content and number concentration, respectively, relating to Poisson counting uncertainty for each position. 73

4.5 Wind roses during sampling for each tower. Wind direction is indicating where the wind originates, concentric circles indicate the frequency of wind, and the color scale on the left-hand side indicates wind speed. The direction of transit across each tower is indicated by the circled arrow in the lower right of each plot. 77

4.6 Representative size distribution for drift droplets at each tower compared to size distributions reported in previous studies. 79

4.7 PM emission rate from drift droplets for each tower as a function of drift droplet diameter. Vertical dashed lines represent the threshold for drift droplets which would produce $PM_{2.5}$ upon evaporating based on measured TDS concentration at each respective tower. Total PM_{10} and $PM_{2.5}$ emission rates are summarized in text. 82

List of Tables

1.1 Field campaigns in which PDI data were acquired to be used for this work. 8

3.1 Relevant optical properties of the dual-range PDI instrument used in this study. 50

4.1 Summary table of cooling tower properties relevant to drift emissions. . 68

4.2 Summary table of environmental and plume conditions averaged over the sampling period for each tower.
*data reported by nearest weather station 75

Abstract

PHASE-DOPPLER INTERFEROMETRY: CHARACTERIZATION AND EMERGING APPLICATIONS

by

Mason Douglas Leandro

Clouds play a critical role in regulating Earth's climate. Despite their importance, cloud representation in climate models remains a challenge and the response of clouds to warming is a primary factor governing our estimates of climate sensitivity (Bony et al. 2017; Medeiros et al. 2014; Medeiros et al. 2008; Vial et al. 2013; Webb et al. 2006). This is partly because cloud drops can not be represented explicitly so parameterization schemes are used to represent clouds statistically. These schemes are often poorly constrained due to the complexity of cloud microphysical processes and a lack of observational measurements (see Morrison et al. 2020). Detailed and precise measurements of cloud properties are needed to better constrain parameterization schemes and improve our understanding of cloud microphysical processes.

A phase-Doppler interferometer (PDI) is an optical instrument (Bachalo 1980) used to measure individual cloud drop size and velocity from airborne platforms (see Chuang et al. 2008 for development of flight probe). Due to the measurement principle, this instrument overcomes many of the issues facing other existing cloud probes. In order to generate the drop concentrations and integrated quantities needed to better constrain models, the sample volume of a PDI must be accurately characterized. The

goal of Chapters 2 and 3 is to develop new methods of characterizing PDI sample volume. In Chapter 2, we characterize probe volume diameter empirically from *in situ* measurements and present algorithms which account for deviations from theoretical behavior. We show that our methods may be successfully applied to aircraft observation and, using artificially-generated data, show that our methods are accurate to within 1%. In Chapter 3 we characterize probe volume width, which has typically been assumed to be a fixed known value, using laboratory measurements. We show that probe volume width is not a fixed value but depends on drop size. We apply our methods to recently collected aircraft measurements using a dual-range PDI. To our knowledge, this is the first time dual-range PDI flight data has been analyzed to assess agreement between each channel. We show good number concentration agreement in the overlap region between the two channels, providing confidence that our characterization methods are accurate.

Finally, in Chapter 4, we show the versatility of the PDI by introducing a new emerging application in which the instrument is used to measure particulate matter (PM) emissions from drift droplets at two cooling towers. We measure drift droplet emissions by suspended the PDI over each cooling tower and collecting measurements at various locations across each tower. From our measurements, we generate a size distributions representative of total tower emissions and convert these distributions to PM emissions rates. We find that methods outlined by the EPA (EPA 1995) to estimate PM emissions grossly overestimates true emissions. We also find that the majority of drift droplet emissions generate particles that have a diameter < 2.5 µm ($PM_{2.5}$), which are currently unregulated by the EPA. These findings suggest that EPA methods may require revision to both reflect for lower total emissions and account for unregulated $PM_{2.5}$ emissions.

To my Aunt Mary,

You continue to inspire me.

Acknowledgments

My journey to reach this point in my professional career has been a long labor of love for me. None of it would have been made possible without the help and support of so many individuals and, for that, I am incredibly grateful.

I must first acknowledge my advisor, Dr. Patrick Chuang. To say that Patrick has been an extraordinary advisor would be an understatement. His patience, dedication, and guidance over the years allowed me to achieve this incredible accomplishment and I would like to think that some small portion of the awe-inspiring wisdom he possesses has been passed on to me. Along with being an incredible advisor, Patrick is a wonderful human-being who I am proud to call a friend. In my first phone call with Patrick, I asked him what he looks for in a graduate student. The first part of his response was what I expected - a smart and dedicated student who is capable of conducting impactful research. What surprised me was then next part of his response, where he very genuinely told me that one of the things he values most is the relationship he forms with his students. I did not realize it at the time, but this was the beginning of a life-long friendship which I cherish very deeply. I cannot speak more highly of Patrick and am incredibly grateful to have had such a wonderful advisor.

Next I would like to thank the remainder of my reading committee, Professor Nicole Feldl, Dr. Jan Kazil, and Dr. William Bachalo for their valuable guidance in my research endeavors. With their counsel, the quality of my research improved significantly and for that, I am very grateful. I would especially like to thank Dr. William Bachalo, who I worked with very closely in more recent years and will continue to work with in the future.

I would also like to thank the various people who made my field work possible. My work in Barbados during the Atlantic Tradewind Ocean–Atmosphere Mesoscale Interaction Campaign (ATOMIC) field campaign would not have been possible without Dr. Graham Feingold. I would also like to thank the National Oceanic and Atmospheric Administration (NOAA) P-3 hurricane hunter flight crew. My research in cooling tower particulate matter emissions was due to the tireless efforts of Professor Anthony Wexler and Chris Wallis as well as cooling tower and crane operators at the various power plants where measurements were collected. My research in San Diego, CA during the Southern California Interactions of Low Cloud and Land Aerosol (SCILLA) field campaign was due to efforts put forth by Assistant Professor Mikael Witte, who also commonly provided comedic relief when it was needed most. I would also like to thank the staff and pilots at the Center for Interdisciplinary Remotely-Piloted Aircraft Studies (CIRPAS) for their role in the various field campaigns used in this research as well as the staff at Artium Technologies, Inc. for their continued efforts in assisting me with my research.

I could not have accomplished this without the love and support of my family. To my dad, who instilled in me principle of dedication and hard work and who inspired me to make something of myself. If you're going to do something, do it right. To my mom, who continually supports me in every aspect of my life and constantly asks me questions about my research even though most of my answers only make her more confused. Despite this, I'm pretty sure she's becoming an expert in phase-Doppler interferometry. To my brother, Miles, for always looking after me and acting with my best interests in mind. He's someone I admire, love, and respect very much and, in many ways, I aspire to be more like him.

To my best friend and partner, Kelsie. Your love and support brings me comfort when I am most in need and you make me realize a better version of myself. I couldn't do this without you.

Lastly, to Nala & Jack. One a cloud, the other its shadow.

Previously published material:

The text of this dissertation includes reprints of the following previously published material:

Chapter Four: Leandro, Mason D., Christopher Wallis, Anthony Wexler, and Patrick Chuang.“Positive and negative emissions from cooling towers, part 1: Droplet measurements” Aerosol Science and Technology 57, no. 1 (2022): 1-11.

Chapter 1

Introduction

Earth's climate is a complex system consisting of a myriad of interconnected components. Of the numerous factors that regulate the Earth's climate, clouds play a critical role. Clouds redistribute water across the planet through precipitation and thus are a crucial link in the hydrological cycle. They alter Earth's energy budget through interactions with solar and terrestrial radiation and through the release of latent heat of condensation, which redistributes thermal energy and contributes to atmospheric circulation.

Despite their importance to Earth's climate, the representation of clouds in even the most sophisticated models remains a challenge, and this impedes our ability to accurately predict future climate. Global climate models attempting to forecast how clouds respond to warming yield different predictions (Bony and Dufresne 2005; Webb et al. 2006) and this response is a primary factor governing variations in our estimates of climate sensitivity (Bony et al. 2017; Medeiros et al. 2014; Medeiros et al.

2008; Vial et al. 2013; Webb et al. 2006). Even high spatial resolution models yield varying predictions for the same initial conditions (vanZanten et al. 2011; Matheou et al. 2011). This is partly due to the fact that individual drops cannot be represented explicitly due to the sheer number of drops present in a cloud. A small cloud can contain more that 10^{17} drops. Even with massive advances in computational processing power, it would be impossible to represent all drops explicitly in any climate or weather model. Therefore, such models must rely on microphysical parameterization schemes to represent cloud properties statistically. These schemes are often poorly constrained due to the complexity of cloud microphysical processes and a lack of observational measurements (see Morrison et al. 2020). Therefore, detailed and precise measurements of cloud properties are needed in order to better constrain parameterization schemes and improve our understanding of cloud microphysical processes.

There are a variety of instruments which are commonly used to obtain measurements of cloud properties from airborne platforms, each with their own set of limitations and issues. Many instruments are prone to drop shattering, in which particles shatter on the housing of the instrument which then pass through the measurement region, biasing results (e.g., Baker et al. 2009a; Baker et al. 2009b; Gardiner and Hallett 1985; Korolev et al. 2011; Korolev and Isaac 2005; Lawson 2011). Many probes have large uncertainty in their sample volume (e.g., Baumgardner and Korolev 1997; Baumgardner and Spowart 1990; Dye and Baumgardner 1984; Korolev 2007; Lance et al. 2010) or can experience significant sizing errors due to coincident events (e.g., Coelho et al. 2005; Brenguier 1989; Brenguier et al. 1994; Lance 2012). Additionally, many instruments have a limited range of drop sizes in which they are capable of measuring (see Chapter 5, Table 5.1 in Wendisch and Brenguier 2013). One instrument that overcomes many of the issues facing other instruments is the phase-Doppler interferometer (Fig 1.1).

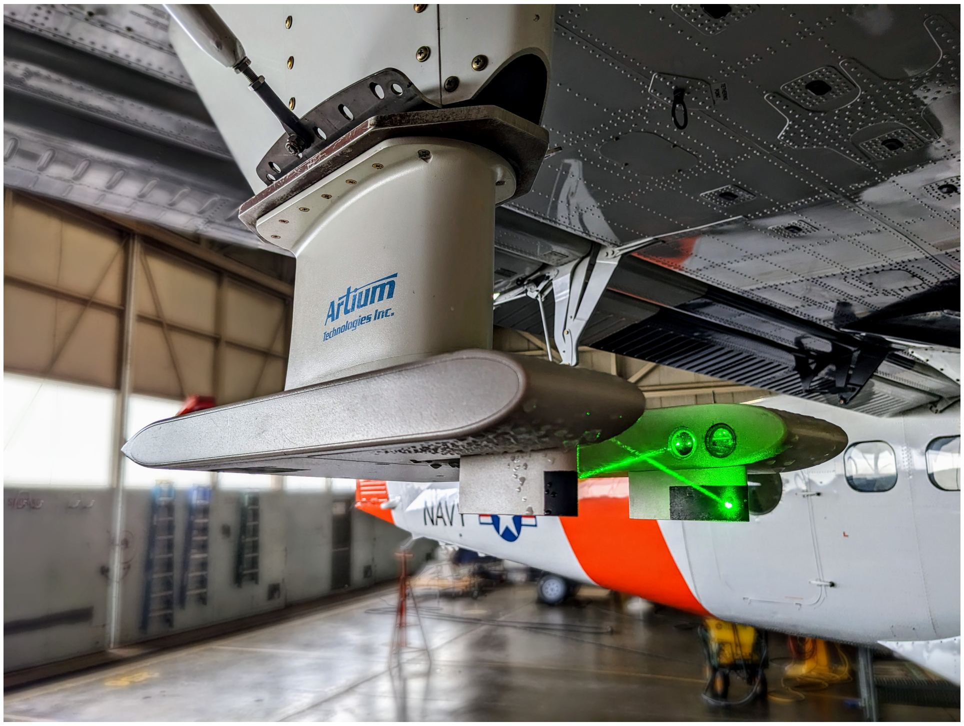

Figure 1.1: Image of a phase-Doppler interferometer.

A phase-Doppler interferometer (PDI) is an optical instrument based on the technique of phase-Doppler interferometry (Bachalo 1980; Bachalo and Houser 1987; Bachalo and Houser 1984; Bachalo and Houser 1987; Sankar et al. 1993; Sankar et al. 1991; Jackson 1990; Albrecht et al. 2013).It is used to measure the drop size and velocity of individual drops in a variety of applications including spray sciences, pollution and aerosol sciences, and atmospheric sciences. The measurement region is established by two identical lasers, each with a Gaussian intensity profile, which intersect each other at a known angle (Fig. 1.2). Constructive and destructive interference between the two intersecting beams causes a fringe pattern to form perpendicular to the beam axis (middle panel in Fig. 1.2). Drops passing through the fringe pattern scatter light towards multiple detectors where each detector records the time-varying intensity of the scattered signal (bottom panel in Fig. 1.2). The signal has Gaussian envelope, due to the Gaussian intensity profile of each beam, overlaid with a high-frequency sinusoidal signal, due to the fringe pattern. Velocity is measured from the frequency of the signal from any one of the detectors using the same technique as Laser Doppler Velocimetry (Wang 1988). Drop size is measured using the phase shift between each pair of detectors, which has a nearly monotonic, linear relationship with drop size (Bachalo and Houser 1984). Due to the measurement principle, a PDI instrument overcomes many of the issues facing other instruments. Because measurements are collected where beams intersect at a significant distance from the instrument housing (Fig 1.1), drop shattering is not a concern (Chuang et al. 2008). The technique also produces a well-defined sample volume, as will be discussed in great detail in Chapters 2 and 3, and is capable of measuring drops between 1 µm to 2 mm (or larger if the drops remain sufficiently spherical), a much larger range than most other instruments. Additionally, due to the unique signal generated when a drop transits the probe volume, issues in sizing error due to coincident events are less problematic and can be resolved with additional signal processing.

In order to derive integrated quantities from PDI measurements, accurate

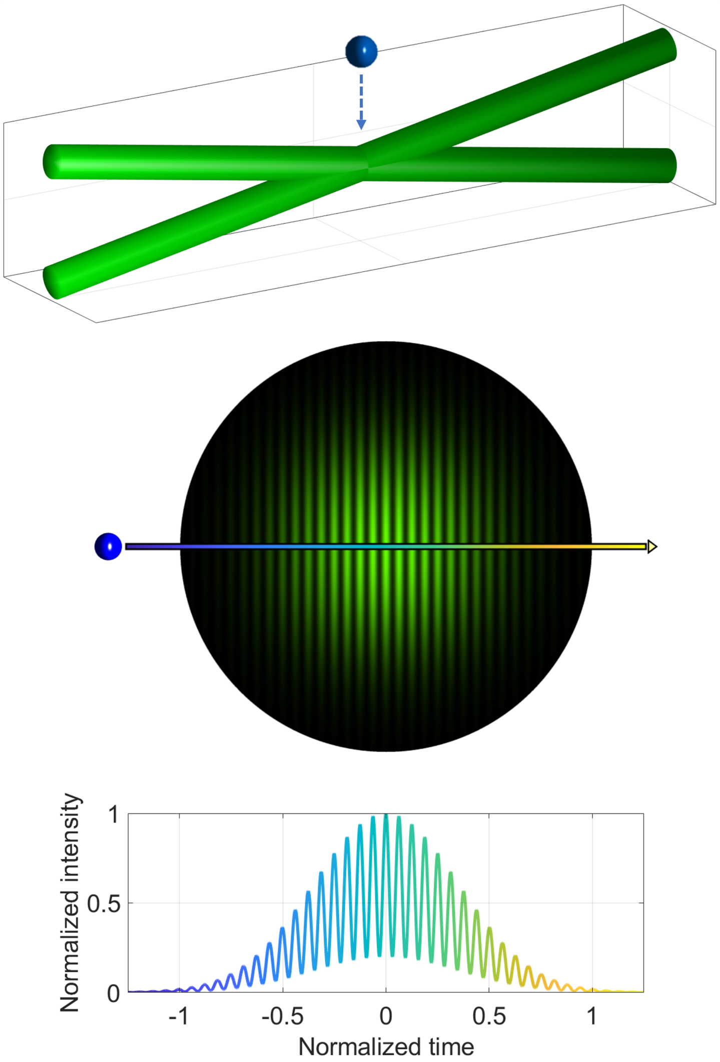

Figure 1.2: Diagram of the signal measured by a detector when a drop transits the measurement region. Top panel shows the intersection of the two beams, middle panel shows a cross-section of the intersecting beams, and bottom panel shows the time-varying intensity measured by a single detector.

estimates of the volume of space sampled by a PDI is required. The effective volume of space sampled by a PDI is determined by the instrument velocity relative to the atmosphere (i.e., true air speed of the aircraft) multiplied by the effective sample area of the instrument. The effective sample area of the instrument is composed of: (i) the diameter of the intersecting beams, referred to as the probe volume diameter, D_{beam}; and (ii) the probe volume width, W_c, which is determined by the optical configuration of the instrument (Fig. 1.3) and depends on drop size.

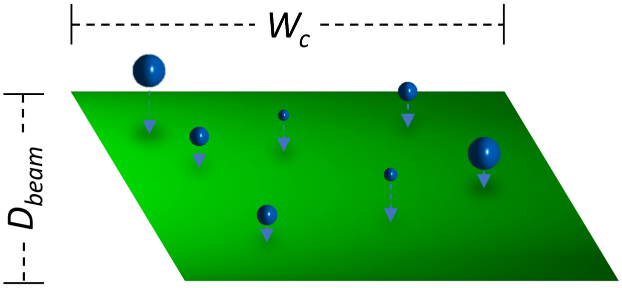

Figure 1.3: PDI effective sample area. Angle in the vertical axis is due to the collection angle in the receiver.

In this work, we first focus on characterizing each dimension of the PDI probe volume. In Chapter 2, we develop automated algorithms for probe volume diameter characterization using laboratory and aircraft measurements and assess variability in probe volume diameter for three field campaigns. In Chapter 3, we develop a novel technique to characterize probe volume width from laboratory measurements. We use a newer dual-range PDI, consisting of two channels which, when merged allow for accurate measurements across a large size range. We apply methods from Chapter 2 and Chapter 3 to recently collected flight data and assess number concentrations collected by each channel of the PDI, with particular emphasis on the overlap region. To our knowledge, this is the first time dual-range PDI flight data has been analyzed to assess agreement between each channel. Flight data used for Chapters 2 and 3 is briefly described in Section 1.1. In Chapter 4 we present a new PDI application in which drift droplet measurements are collected from cooling towers located at two separate power plants. We use our measurements to estimate particulate matter emissions from drift droplets and compare the results against emissions calculated using methods outlined by the United States Environmental Protection Agency.

1.1 Aircraft Observations Used in this Study

In Chapter 2, we apply our methods to data collected during three field campaigns: Marine Stratus Experiment (MASE), Physics of Stratocumulus Top (POST), and VAMOS (Variability of the American Monsoons) Ocean-Cloud-Atmosphere-Land Study (VOCALS-REx). MASE took place in July of 2005 off the coast of Monterey, CA. The overarching goal of the campaign was to better understand aerosol-cloud interactions in clean and perturbed marine stratocumulus (Lu et al. 2007). Of the 13 research flights that took place during MASE, we analyze PDI data from 8 flights in this work. The POST campaign took place in July and August of 2008 in the same vicinity as MASE. One goal of the campaign was to understand processes which take place at the interface between the stratocumulus-topped boundary layer and the free troposphere (Malinowski et al. 2013). Of the 20 research flights that took place during POST, we analyze PDI data from 16 flights in this work. VOCALS-REx took place in October and November of 2008, shortly after the conclusion of POST, off the coast of northern Chile in the Southeastern Pacific. VOCALS-REx had two main goals: (1) improve understanding of aerosol-cloud-drizzle interactions in the boundary layer and (2) improve simulation and predictive modeling capability in the Southeastern Pacific

(Wood et al. 2011). Of the 18 research flights that took place, PDI data from 15 flights are analyzed in this study.

In Chapter 3 we apply our methods to data recently collected during the Southern California Interactions of Low Cloud and Land Aerosol (SCILLA) campaign. The goal of this campaign gain a better understanding of the interactions between horizontal circulation, vertical mixing, aerosols and clouds in the Southern California Bight. We apply our methods to one flight from this campaign.

A brief description of the campaigns is given in Table 1.1.

Campaign	Time Period	Location	# of Flights Analyzed	Cloud Type
MASE	Jul 2005	Monterey, CA	8	Marine stratocumulus
POST	Jul-Aug 2008	Monterey, CA	16	Marine stratocumulus
VOCALS-REx	Oct-Nov 2008	Northern Chile	15	Marine stratocumulus
SCILLA	Jun 2023	San Diego, CA	1	Marine stratocumulus

Table 1.1: Field campaigns in which PDI data were acquired to be used for this work.

Chapter 2

An automated method for probe volume diameter characterization in phase-Doppler interferometry

Abstract

A phase-Doppler interferometer (PDI) is an instrument used to measure liquid water content, number concentration and drop size distribution in liquid water clouds. In order to derive these quantities, an accurate estimate of the volume of space sampled by a PDI must be acquired. Here we present an automated method of characterizing probe volume diameter, D_{beam}, which varies with drop size, d, empirically from *in situ* measurements. The method accounts for any changes in prevailing conditions as well as the presence of gate chop and short gate events. Applying our methods to laboratory measurements and various field campaigns yields confidence as results

align with theoretical prediction and suggests that our algorithms can be successfully implemented to aircraft observations. Our results indicate that the PDI exhibits very low day-to-day $D_{beam}(d)$ variability during flight acquisition. Using an artificially-generated data set, we find that our methods are robust and accurate to within 1%.

2.1 Introduction

2.1.1 Theoretical Framework

In this chapter, we will focus on one dimension of the instrument measurement region, D_{beam} (Fig. 1.3). D_{beam} is smaller for small drops and larger for large drops and thus is a function of drop size (d), varying by approximately an order of magnitude between small and large drops over the measurement range of a PDI (Bachalo and Houser 1984; Chuang et al. 2008). This is because: (i) the beam has a Gaussian intensity profile in which the greatest intensity is in the center of the beam; (ii) drop scattering intensity is proportional to d^2; and (iii) for a drop to be detected there is some minimum signal-to-noise ratio (SNR) that must be achieved. Thus a large drop can pass through the measurement region further from the center of the beam than a small drop and still be detected. Let us consider two scenarios: a) a population of large drops and b) a population of small drops, both with the same trajectories through the measurement region. These two scenarios are depicted in Fig. 2.1. Drops that have a trajectory further from the center of the beam will scatter less light (Bachalo and Sankar 1996). Because large drops scatter more light than small drops, a large drop passing far from the center of the beam will register a large enough SNR to be detected by the PDI whereas a small drop with the same trajectory will not be detected. This results in a functional dependence of D_{beam} on d.

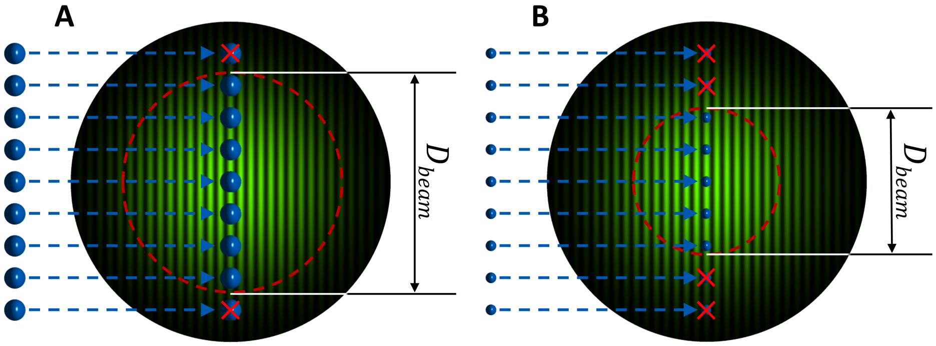

Figure 2.1: Vertical cross section of the intersecting lasers taken parallel to the direction of travel (i.e., an end view of the measurement region). The beam is most intense in the center and decreases in intensity moving radially away from the center. A population of a) large drops and b) small drops passes through the measurement region from left to right with different trajectories (blue dotted lines). A red "X" depicts a situation in with a drop is not detected and the red dashed line represents the detectable diameter of the laser for each drop size, illustrating the functional dependence of D_{beam} on d.

We can determine D_{beam} for a single drop size empirically by analyzing the distribution of transit lengths ($l_{transit}$) (Fig. 2.2). In practice, this analysis is done for a narrow range of drop sizes. For each individual drop, we calculate $l_{transit}$ as $t_g u_d$, where t_g and u_d are the measured gate time and velocity of an individual drop, respectively. Consider a population of monodisperse drops transiting through the measurement region (Fig. 2.2). The maximum transit distance ($D_{transit}$) for this drop size can be determined empirically by fitting the theoretical probability distribution function (PDF) P_t of transit lengths (Chuang et al. 2008):

$$P_t(x) = \frac{x}{\sqrt{1-x^2}} \text{ where } x = \frac{l_{transit}}{D_{transit}},\ x \in [0,1] \tag{2.1}$$

Because we know that the beam is circular in cross section, the best fit value of $D_{transit}$ yields D_{beam} for a single drop size. For the remainder of this chapter, we consider $D_{transit}$ and D_{beam} to be equivalent.

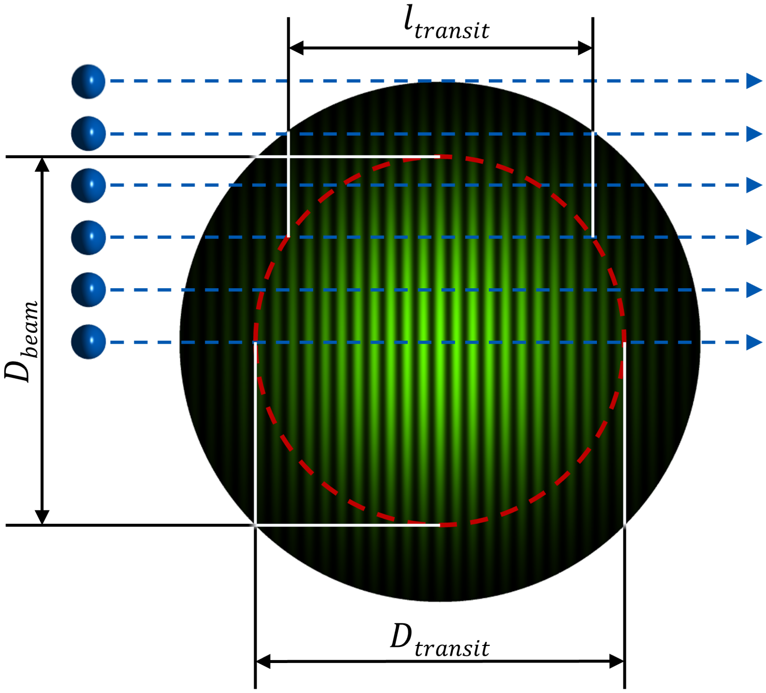

Figure 2.2: Cross section of the measurement region with six drops transiting the probe volume from left to right at different locations. The schematic illustrates that the $l_{transit}$ distribution will be strongly weighted in favor of $l_{transit}$ close to the maximum possible value, $D_{transit}$. The theoretical probability distribution is given by Eq. 2.1. D_{beam} is the desired dimension of the measurement region, and is obtained assuming $D_{transit} = D_{beam}$.

However, Eq. 2.1 goes to ∞ at $D_{transit}$ (Fig. 2.3), making curve-fitting routines problematic (i.e., the fitting process may not converge with a poor guess). To avoid issues with automated routines, curve-fitting has been previously done manually, a tedious and time-consuming process. We pose a new approach which is more suitable for automated curve-fitting. Instead of fitting to the PDF, we fit the theoretical cumulative distribution function (CDF) C_t (Fig. 2.3) which is simply the integral of Eq. 2.1.

$$C_t(x) = 1 - \sqrt{1 - x^2} \text{ where } x = \frac{l_{transit}}{D_{transit}},\ x \in [0, 1] \tag{2.2}$$

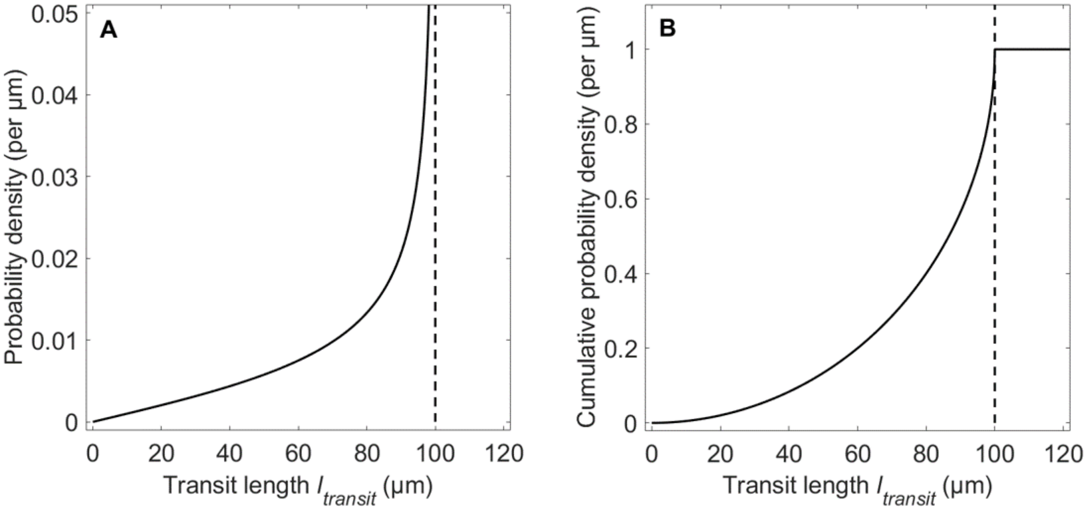

Figure 2.3: Theoretical a) PDF and b) CDF of $l_{transit}$ given by Eqs. 2.1 and 2.2, respectively, plotted as solid line, where the specified view volume diameter is 100 µm (dashed vertical line).

Once we have computed D_{beam} for each size bin, we use the theoretical prediction for the dependence of D_{beam} on d outlined in [Chuang2008] to ensure that our estimates are consistent with theory:

$$D_{beam}(d) = \sqrt{K_0 + K_1 \ln d} \tag{2.3}$$

where K_0 and K_1 are constants. The theoretical underpinning of this relationship are that: (1) laser intensity has a Gaussian distribution and (2) the minimum SNR required for a drop to be detected is the same across all drop sizes.

By automating the PDI sample volume processing method, we are able to obtain a more accurate estimate of $D_{beam}(d)$ and explore this relationship in further detail and over different time scales.

2.1.2 Deviations from Theoretical Behavior

Equation 2.2 is used for an idealized situation. However, conditions may exist which result in a faulty measured gate time record, altering the distribution of $l_{transit}$ and resulting in a poor D_{beam} estimate. Here, we describe the conditions which may cause a faulty gate time record.

Let us consider a situation in which three drops traverse the probe volume at slightly different times (Fig. 2.4). The idealized situation is displayed in Fig. 2.4a. As each drop traverses the probe volume, the time-varying scattered signal is sent to the detector (top panel in Fig. 2.4a). As each drop enters the probe volume, SNR and signal amplitude increases above a threshold and the gate opens, triggering the start of an event (bottom panel in Fig. 2.4a). As each drop exits the probe volume, SNR decreases below the threshold and the gate closes, which ends the event. Gate time t_g is the duration of time the gate is open for each event and inter-occurrence time (IOT) is the duration of time the gate is closed between events.

However, there are events which deviate from this ideal scenario. One example occurs when signal intensity is relatively low near the edges of the scattered signal. The signal may be masked by noise, causing a momentary decrease in SNR to just below the threshold. This triggers the gate to close prematurely, only to reopen again when SNR increases again above the threshold. This causes the same drop to be recorded multiple times, with each event registering a shorter gate time and an uncharacteristically short

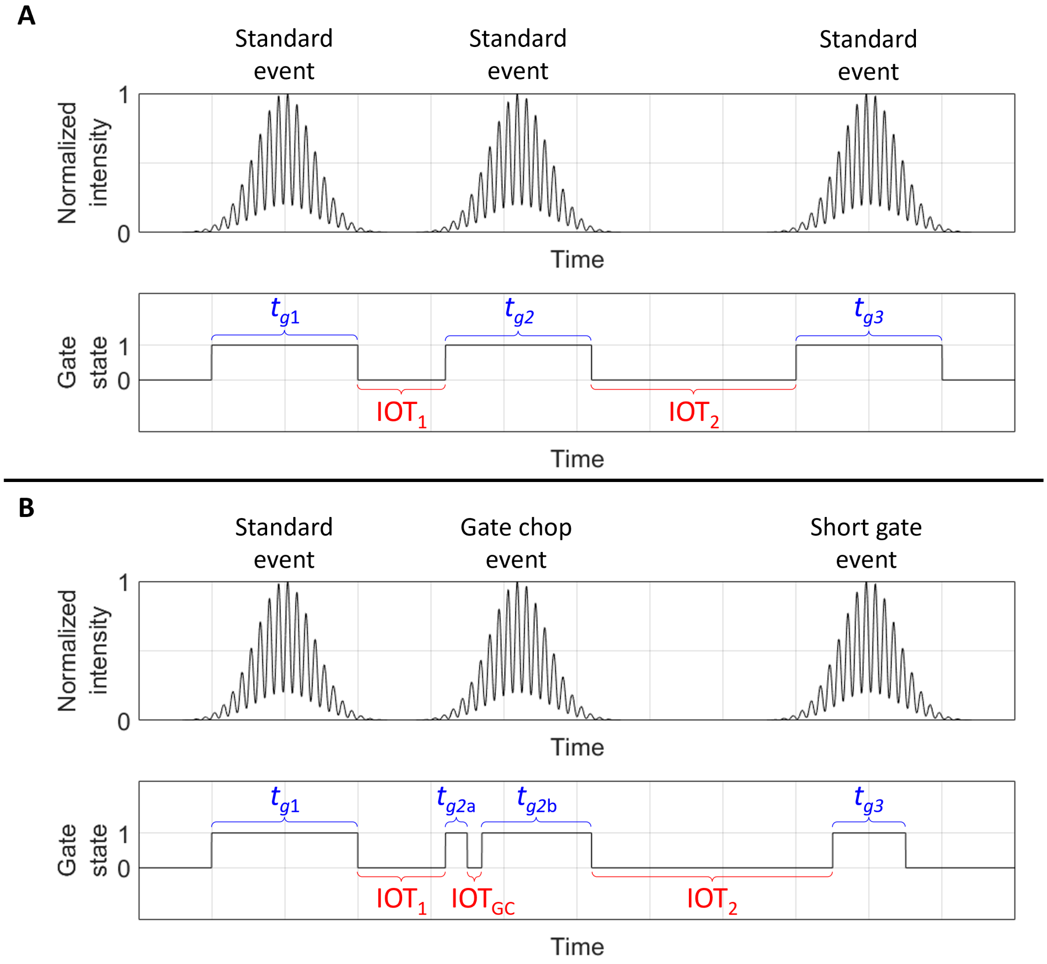

Figure 2.4: Time-varying intensity and gate state for three drops traversing the probe volume for a) an idealized case and b) a case with gate chop and short gate events. Each top panel represents the time-varying intensity as measured by and individual detector and each bottom panel represents the gate state, with a value of 0 corresponding to the gate being closed and a value of 1 corresponding to the gate being open. The gate time of each event is annotated in blue and the inter-occurrence time between each event is annotated in red.

IOT between events (second drop in Fig. 2.4b). This situation is referred to as a gate chop event. Alternatively, the gate may not reopen or the recording with the shorter gate time may not be validated, causing the drop to be recorded only once but with an artificially short gate time (third drop in Fig. 2.4b). This situation is referred to as a short gate event.

One can determine the presence of frequent gate chop or short gate events by generating a PDF of $l_{transit}$ for a narrow drop size range. If frequent gate chop or short gate occurs, then the PDF will be bimodal, with the first mode due to shorter gate times associated with gate chop and short gate events (Fig. 2.5). If our algorithm does not account for these events, drop concentrations will be inflated, due to overcounting in gate chop events, and D_{beam} will be underestimated.

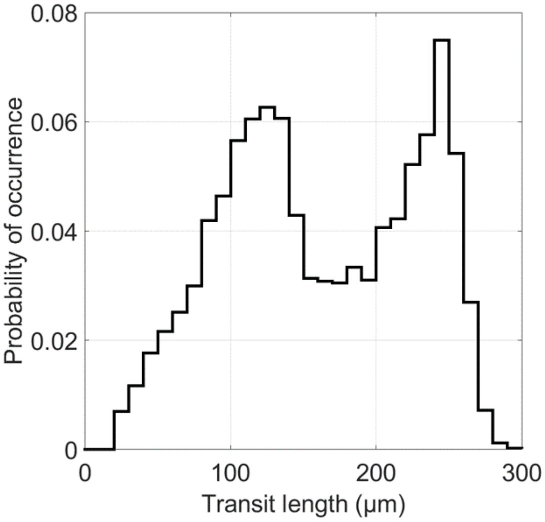

Figure 2.5: Probability distribution of transit lengths which displays bimodality due to gate chop and/or short gate for $16.9\ \mu m \le d < 18.9\ \mu m$. Data displayed is from the Nov-10 2008 flight of the VOCALS-REx field campaign.

To our knowledge, no research has been published describing methods to account for gate chop and short gate events. In Sections 2.3.1 and 2.3.2 we describe algorithms which account for the presence of gate chop and short gate events. A flow chart is provided describing the pathway for determining $D_{beam}(d)$ (Fig. 2.6).

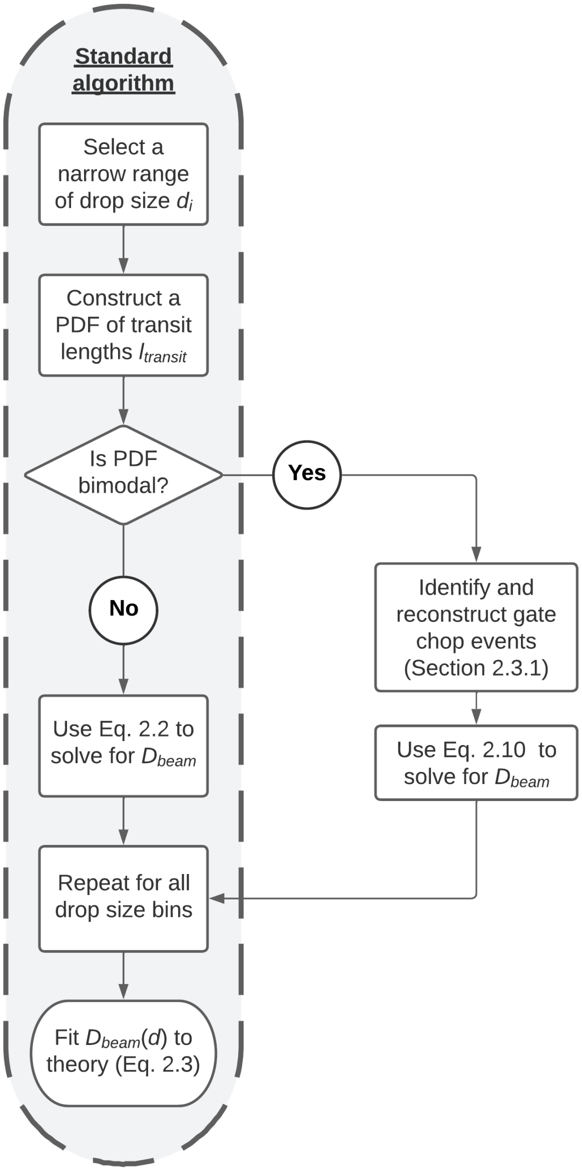
Standard algorithm
Select a narrow range of drop size d_i
Construct a PDF of transit lengths $l_{transit}$
Is PDF bimodal?
Yes
No
Identify and reconstruct gate chop events (Section 2.3.1)
Use Eq. 2.10 to solve for D_{beam}
Use Eq. 2.2 to solve for D_{beam}
Repeat for all drop size bins
Fit $D_{beam}(d)$ to theory (Eq. 2.3)

Figure 2.6: Flowchart describing our recommended pathway for determining $D_{beam}(d)$.

2.2 Applications of Standard Algorithm

In the absence of gate chop and short gates, we use our "Standard algorithm" to process PDI measurements (Fig. 2.6). Here, we present results from this algorithm applied to laboratory and flight data. Data is first binned by drop size into narrow size ranges. We require that each bin contains at least 100 events over a given time interval in order to acquire adequate statistics. Equation 2.2 is used to compute D_{beam} for each bin which meet the criteria. Eq. 2.3 is then fitted to our $D_{beam}(d_i)$ estimates to determine if the computed values are consistent with the theory.

2.2.1 Examples from Laboratory Data

We first present results for our Standard algorithm applied to data collected in a controlled laboratory setting. Figure 2.7 shows the determination of D_{beam} for each d bin through fitting the CDF (Eq. 2.2). Overall, the fitted curves exhibit good agreement with the measurements. Some deviation from the fit is expected and are likely due to measurement error. For example, there are $l_{transit}$ values which are larger than the computed D_{beam} value in each bin. This could be due to error in $l_{transit}$ or error in d, causing drops to be categorized into the wrong d bins. Fig. 2.8 shows the fitted $D_{beam}(d)$ function (Eq. 2.3). The excellent fit in Fig. 2.8 implies that the instrument is performing as theory predicts and provides confidence that our methods produce accurate results.

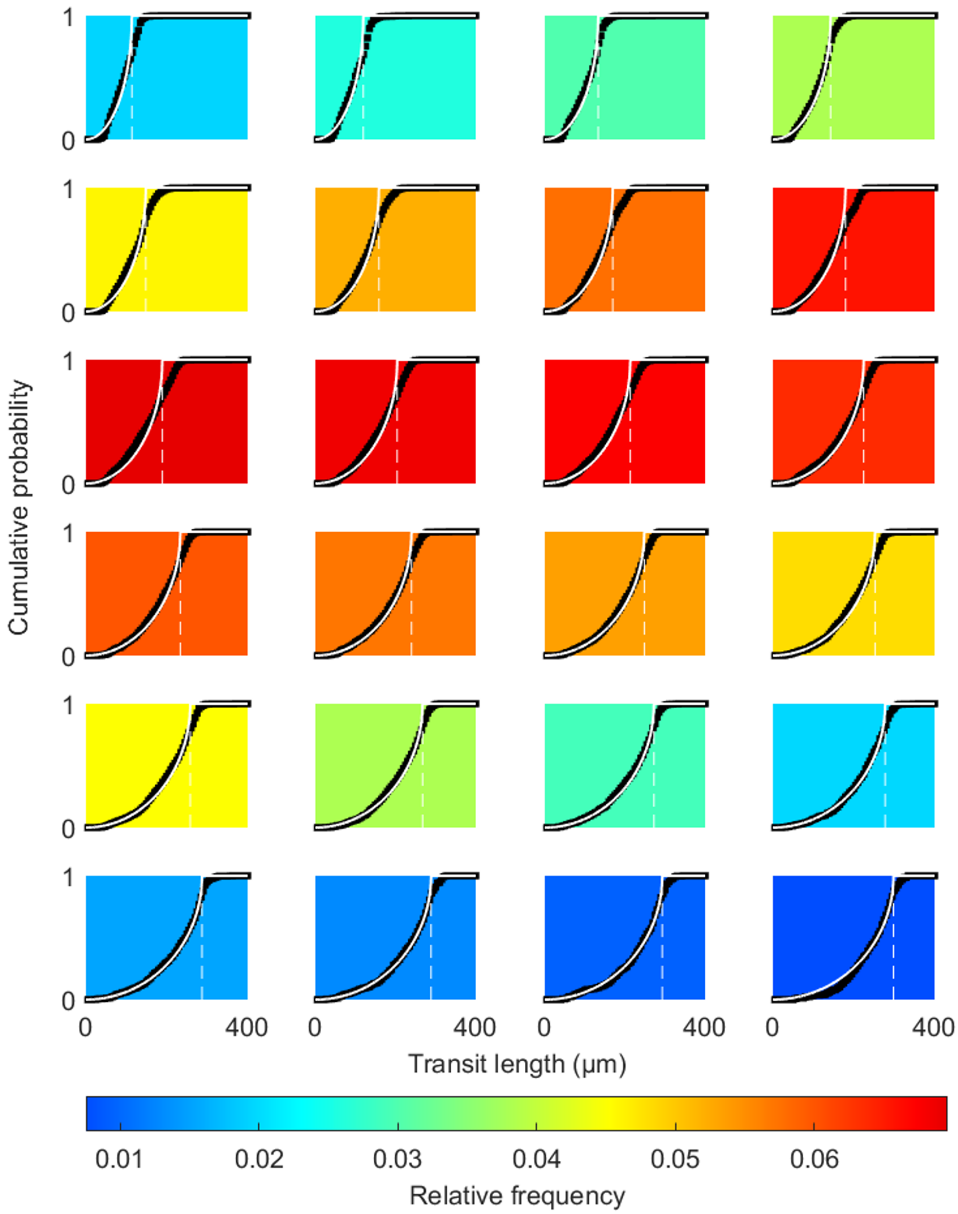

Figure 2.7: Cumulative distribution of $l_{transit}$ for each d bin used to determine $D_{beam}(d)$. Data was collected in a laboratory setting using a conical spray. Drop size bins increase from left-to-right and top-to-bottom. Black dots represent the measured cumulative distribution of $l_{transit}$ for each bin. Solid white line represents fitted curve and dashed white line represents D_{beam} for each d bin. Colored background in each plot represents relative frequency of drops for each bin. Of the $\sim 4.3 \times 10^4$ drops measured, $\sim 95.4\%$ were used for $D_{beam}(d)$ characterization.

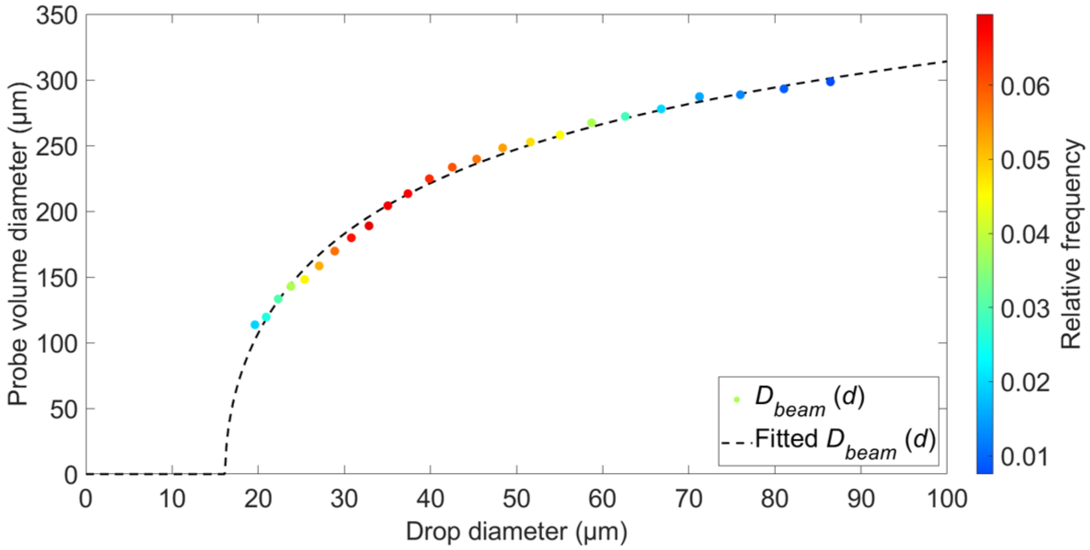

Figure 2.8: Determined $D_{beam}(d)$ relationship for data collected in a laboratory setting using a conical spray. Each point is derived from a single panel in Fig 2.7. Symbol colors represent relative frequency of drops for each bin. Of the $\sim 4.3 \times 10^4$ drops measured, $\sim 95.4\%$ were used for $D_{beam}(d)$ characterization. Black dashed line represents the theoretical fit to data.

2.2.2 Examples from Flight Data

Next, we present results of our Standard algorithm applied to data collected in-flight (Figs. 2.9 and 2.10). There are a number of differences between laboratory and aircraft conditions that make aircraft acquisition potentially more challenging. Relative velocity is approximately an order of magnitude higher on an aircraft. This is easily accommodated by implementing the appropriate signal processor settings. More importantly, the environment is much more noisy on an aircraft due to the various instrumentation present. This makes the PDI more prone to trigger on noise spikes and more likely to exhibit gate chop. Therefore, careful consideration must be taken when processing flight data.

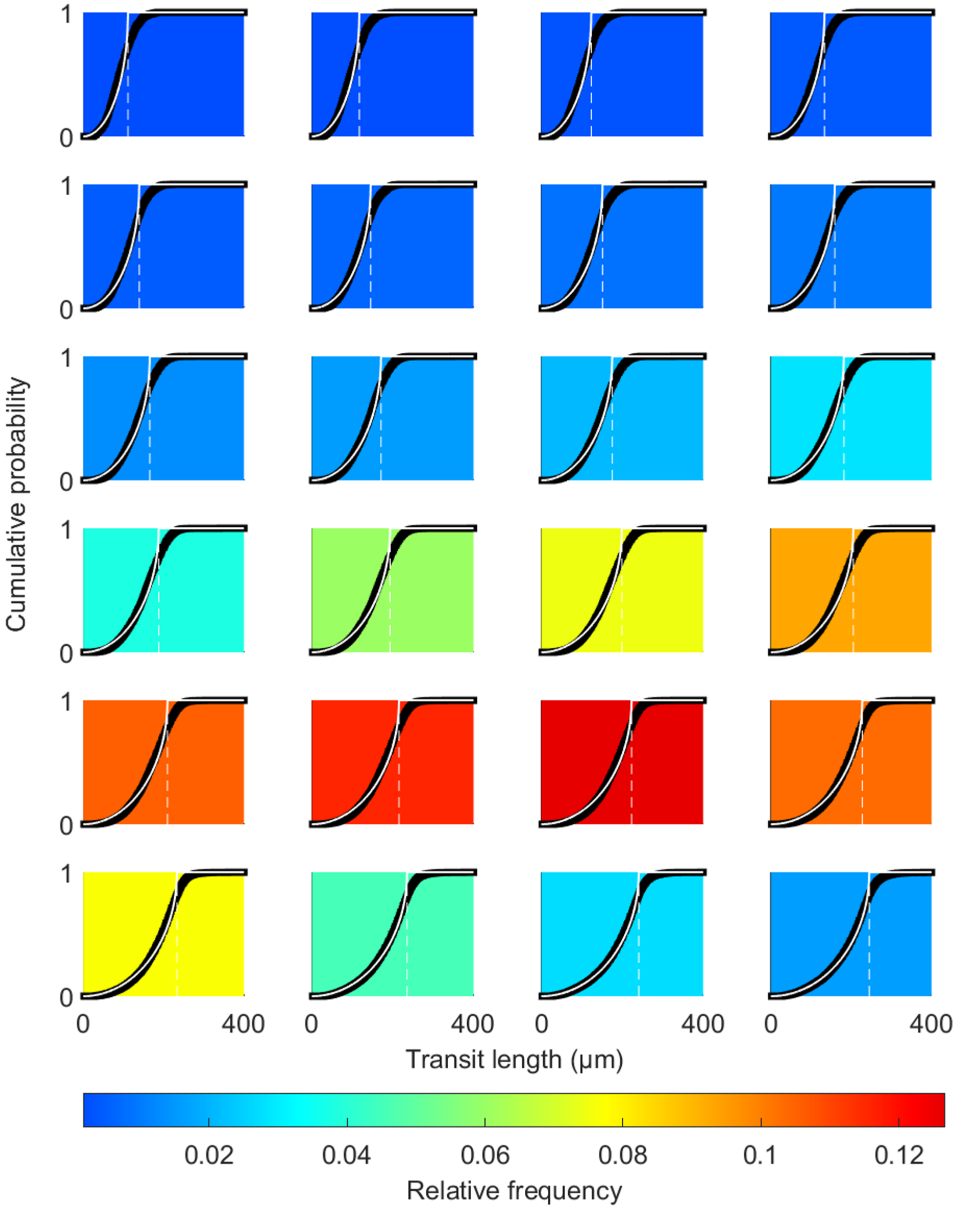

Figure 2.9: Cumulative distribution of $l_{transit}$ for each d bin used to determine D_{beam}. Data was collected on July-21, 2008, during the POST field campaign. Drop size bins increase from left-to-right and top-to-bottom. Black dots represent the measured cumulative distribution of $l_{transit}$ for each bin. Solid white line represents fitted curve and dashed white line represents D_{beam} for each bin. Colored background in each plot represents relative frequency of drops for each bin. Of the $\sim 1.5 \times 10^6$ drops measured, $\sim 97.5\%$ were used for $D_{beam}(d)$ characterization.

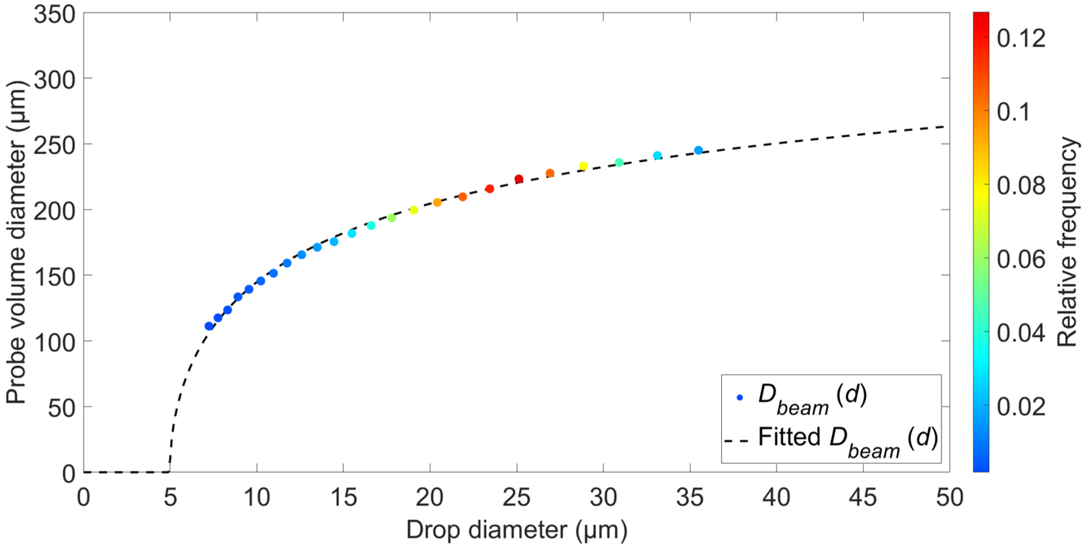

Figure 2.10: Determined $D_{beam}(d)$ relationship for data collected on July-17, 2008, during the POST field campaign. Each point is derived from a single panel in Fig 2.9. Symbol colors represent relative frequency of drops for each bin. Of the $\sim 1.5 \times 10^6$ drops measured, $\sim 97.5\%$ were used for $D_{beam}(d)$ characterization. Black dashed line represents the theoretical fit to data.

Figures 2.9 and 2.10 show our methods applied to data collected on July-21 2008 during the POST field campaign. For this case, there was no evidence of frequent gate chop or short gate. Results displayed in Figs. 2.9 and 2.10 show very good agreement with theoretical prediction and even exhibit better agreement than the laboratory results previously presented (Figs. 2.7 and 2.8). This is likely because much more data were used for the aircraft case, providing a higher level of statistical robustness. These results suggest that our Standard algorithm works well for aircraft observations when frequent gate chop or short gate events are not present.

2.3 Algorithm with Gate Chop and Short Gate Events

2.3.1 Accounting for Gate Chop

Let us first consider the impact of gate chop on the acquired data. Referring to Fig. 2.4, IOT is the duration of time in which the gate is closed between recorded events. The second drop in Fig. 2.4b experiences gate chop. It is recorded twice and generates an additional IOT (IOT_{GC} in Fig. 2.4)b which is uncharacteristically short. Therefore, if frequent gate chop occurs, a PDF of IOT will reveal two distinct modes, with the first mode attributed to gate chop events. We can therefore identify gate chop events by setting an IOT threshold at the upper end of the first mode and identify any events with an IOT less than the threshold as a gate chop event.

An example of a data set with frequent gate chop events can be seen in Fig. 2.11. A threshold for IOT is set at the upper end of first mode (denoted as the vertical dashed line in Fig. 2.11) and any observations with an IOT less than this value are identified as gate chop events.

After gate chop events have been identified, we reconstruct the event using information contained in each of the recorded observations that make up the drop. The arrival time of the reconstructed event is the arrival time of the first recorded event. The transit time is the duration between the gate initially opening and finally closing (i.e., $t_{g2\mathrm{a}} + \mathrm{IOT}_{1.5} + t_{g2\mathrm{b}}$ in Fig. 2.4b). Lastly, we use the drop size and velocity of the recording with the longest gate time as a longer interrogation time provides a more accurate measurement of these values.

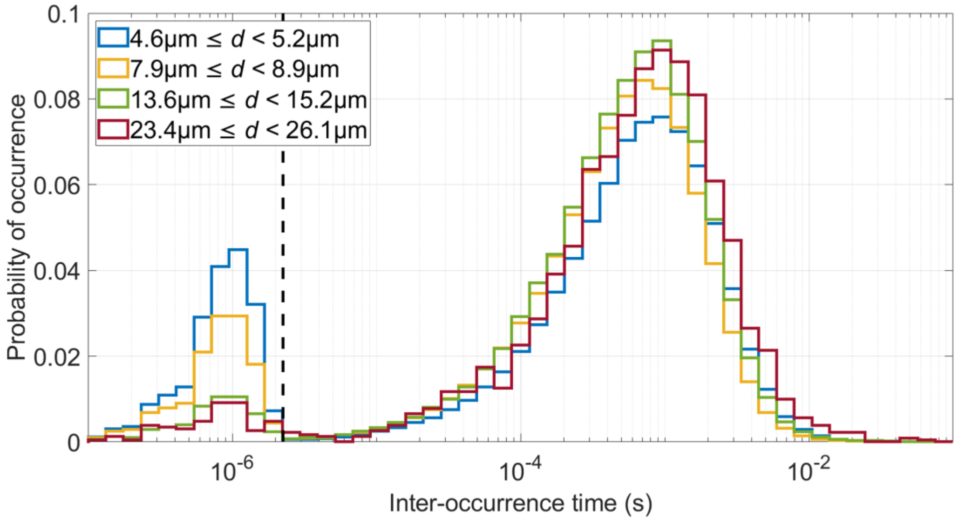

Figure 2.11: Probability distribution of inter-occurrence time for various narrow drop size ranges. Vertical black dashed line represents the threshold to identify gate chop events. Data displayed is from the Nov-10 2008 flight of the VOCALS-REx field campaign.

2.3.2 Accounting for Short Gates

Frequent short gate events generate a second mode in the distribution of transit lengths for a given drop size. The reason for this can be seen in Fig. 2.4 where the third drop registers an artificially short gate time, resulting in an artificially short transit length. This causes Eq. 2.2 to converge on a value of $D_{transit}$ which underestimates the true value. In this case, Eq. 2.2 must be augmented to account for the second mode, which becomes more prominent as short gate events become more frequent. This augmentation is performed by treating short gate events as a separate population. The Standard algorithm (Section 2.1.1) is augmented by fitting to a function which that is the sum of two separate populations, one representing short gate events and a second representing standard events (see Fig. 2.12 for examples).

Assuming that the distribution of transit lengths for short gate events is normally distributed, the CDF of transit lengths for short gate events, C_{sg}, is:

$$C_{sg}(l_{transit}) = \frac{1}{2}[1 + \mathrm{erf}(\frac{l_{transit} - \mu_{sg}}{\sigma_{sg}\sqrt{2}})] \tag{2.4}$$

where μ_{sg} and σ_{sg} are the mean and standard deviation of transit lengths for the population of short gate events. The CDF of transit lengths in the presence of short gate events, C, can then be approximated as the sum of Eqs. 2.2 and 2.4, multiplied by their respective fractional contributions:

$$C(l_{transit}) = (1 - \alpha)C_t + \alpha C_{sg} \tag{2.5}$$

where α is the fraction of C_{sg} contributed to C. Figure 2.12 displays the PDF and CDF of transit lengths with varying levels of α. The value of α allows us to estimate the relative frequency of short gate events in a given data set from a statistical standpoint. α is constrained to a value between 0 and 1.

To prevent the fitting routine from converging on a value of μ_{sg} which is greater than $D_{transit}$, which would contradict the physical process which generates short gate events, we can scale μ_{sg} with $D_{transit}$ through the equation:

$$\mu_{sg} = \beta D_{transit} \tag{2.6}$$

where β is the fractional magnitude of μ_{sg} relative to $D_{transit}$, constrained to a value between 0 and 1.

To prevent fitting routines from converging on an unreasonably high value of σ_{sg}, we can scale σ_{sg} with μ_{sg} through the equation:

$$\sigma_{sg} = \gamma \mu_{sg} \tag{2.7}$$

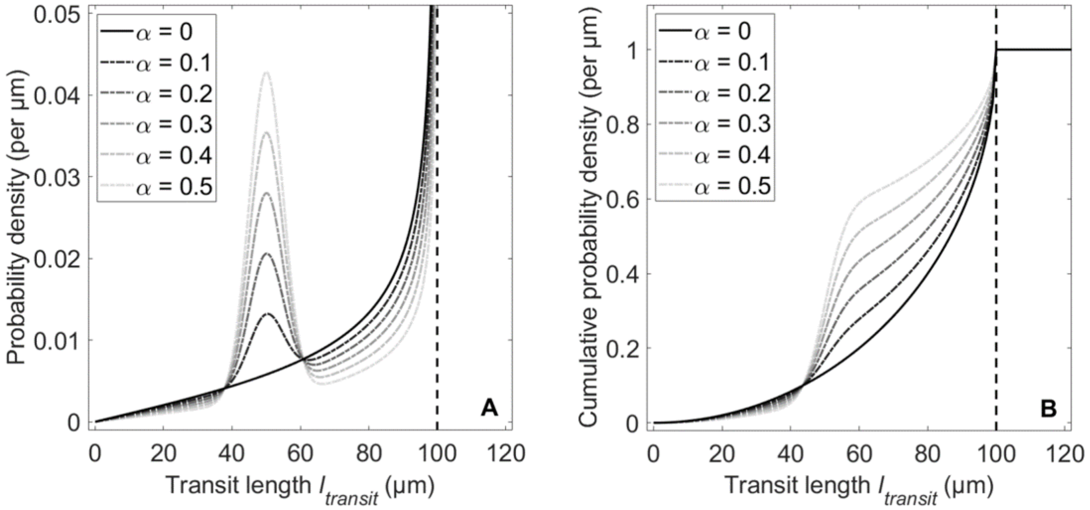

Figure 2.12: Theoretical a) PDF and b) CDF of $l_{transit}$ with varying levels of α, plotted as solid line, where the specified view volume diameter is 100 µm (dashed vertical line).

where γ is the fractional magnitude of σ_{sg} relative to μ_{sg}, constrained to a value between 0 and 1. This results in:

$$C(l_{transit}) = (1-\alpha)(1-\sqrt{1-\frac{l_{transit}}{D_{transit}}^2}) + \frac{\alpha}{2}[1+\mathrm{erf}(\frac{l_{transit}-\beta D_{transit}}{\gamma\beta D_{transit}\sqrt{2}})] \tag{2.8}$$

We then solve Eq. 2.8 for $D_{transit}$, α, β, and γ in a least-squares sense and use the best-fit value of $D_{transit}$ to determine D_{beam} for each drop size bin. From here, Eq. 2.3 is then fitted to our $D_{beam}(d_i)$ estimates to determine if the computed values are consistent with the theory.

2.3.3 Examples from Flight data

For the VOCALS-REx campaign, the PDI instrument experienced frequent gate chop and short gates events (see Figs. 2.5 and 2.11). Therefore, the augmented algorithm which accounts for gate chop and short gate events was implemented. Here we analyze results from the November-10, 2008, flight of the VOCALS-REx campaign.

Using the described methods, 17.5% of events were identified as gate chop events, with gate chop events occurring more frequently for smaller drop sizes. This result makes physical sense as smaller drops scatter less light than larger drops. Therefore, there is a higher probability that the scattered signal falls below the detection limit for smaller drops. Figure 2.13 shows the results of our method for determining D_{beam} for each d bin, displaying a very good fit between data and the least-squares solution obtained by applying Eq. 2.8. We find that short gate events occur more frequently in smaller d bins. We believe this happens for the same reason gate chop events occur more frequent in smaller d bins. Using the fitted values for α in Eq. 2.8, we estimate that $\sim 42\%$ of drops experienced short gate.

Figure 2.14 displays the fitted $D_{beam}(d)$ function using the computed values for each bin, exhibiting very good agreement with theory. This suggests that our method of determining D_{beam} for each d bin works well and that frequent short gate events do not significantly impact our ability to determine $D_{beam}(d)$.

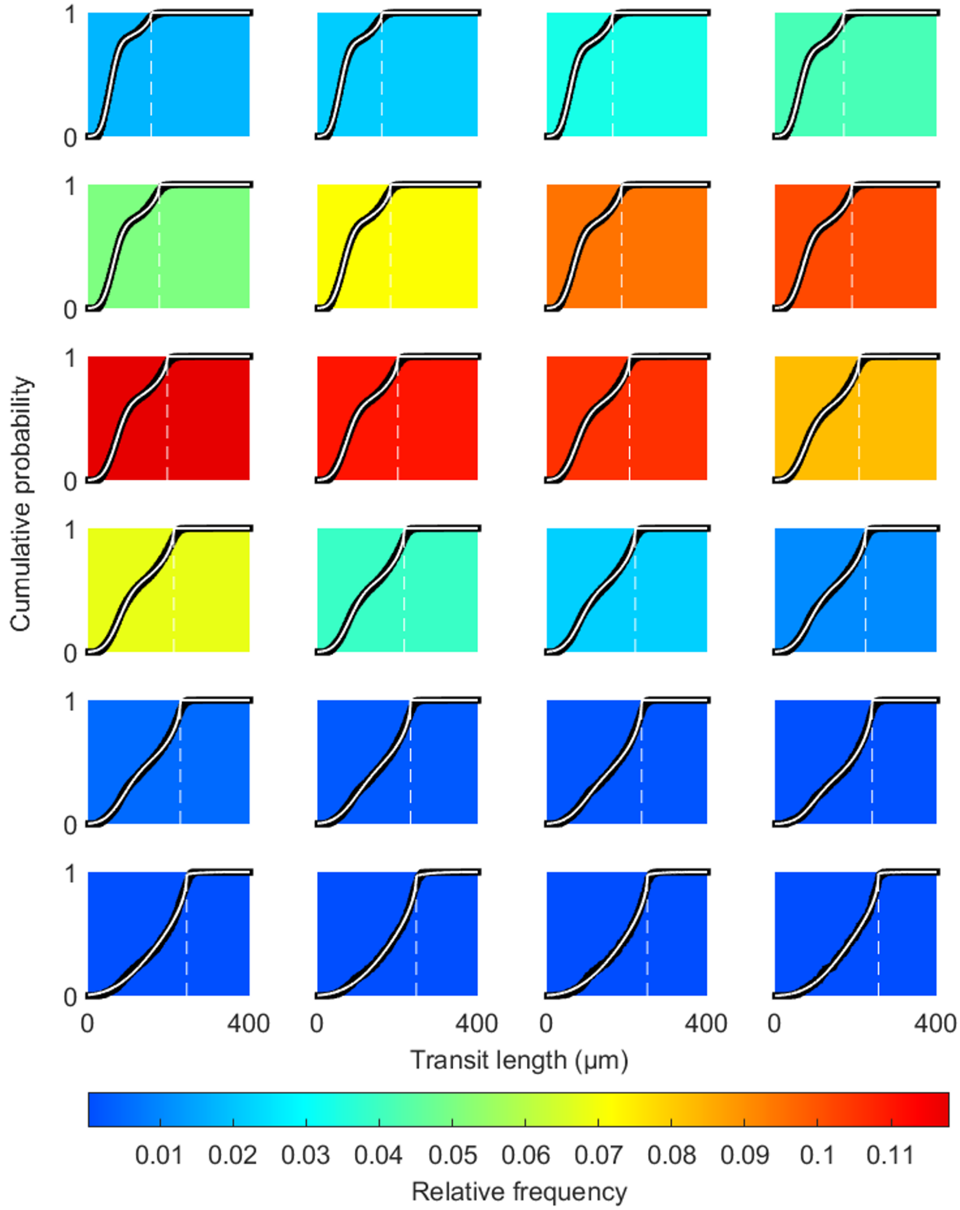

Figure 2.13: Cumulative distribution of $l_{transit}$ for each d bin used to determine D_{beam}. Data was collected on November-10, 2008, during the VOCALS-REx field campaign. Instrument encountered frequent gate chop and short gate events during this campaign. Drop size bins increase from left-to-right and top-to-bottom. Black dots represent the measured cumulative distribution of $l_{transit}$ for each bin. Solid white line represents fitted curve and dashed white line represents D_{beam} for each bin. Colored background in each plot represents relative frequency of drops for each bin. $\sim 2.9 \times 10^6$ drops were recorded, with 95.5% of data used for $D_{beam}(d)$ characterization.

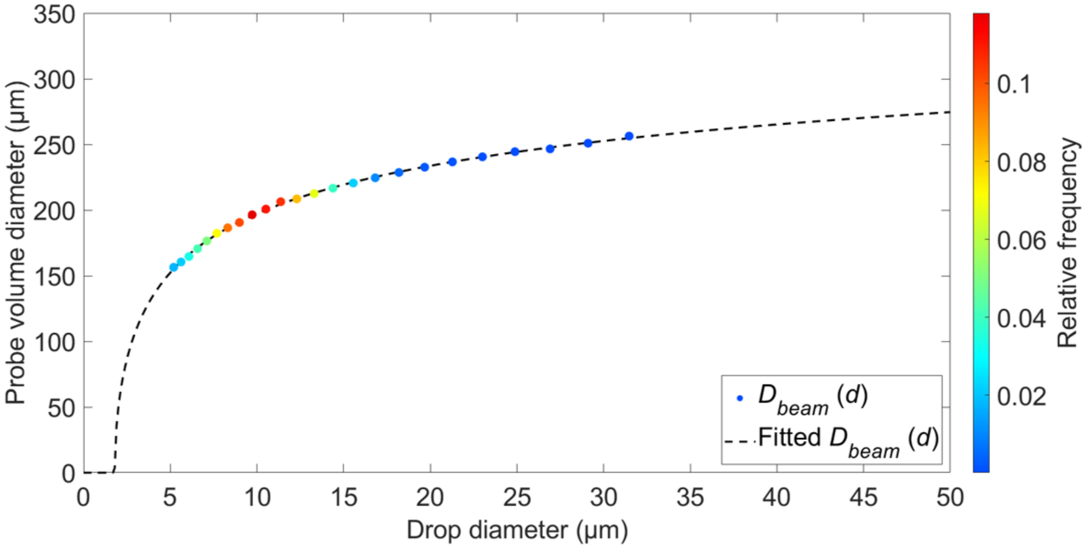

Figure 2.14: Determined $D_{beam}(d)$ relationship for data collected on November-10, 2008, during the VOCALS-REx field campaign. Each point is derived from a single panel in Fig 2.13. Symbol colors points represent relative frequency of drops for each bin. $\sim 2.9 \times 10^6$ drops were recorded, with 95.5% of data used for $D_{beam}(d)$ characterization. Black dashed line represents the theoretical fit to data.

2.4 Variability in Probe Volume Diameter

$D_{beam}(d)$ variability can be due to a variety of factors. Changes in the environmental electronic and optical noise level can impact SNR. Optical contamination on exterior windows can cause beam attenuation and decrease the intensity of the signal. For older lasers, temperature may impact beam output intensity. Additionally, it is possible for older lasers to not function properly and vary in output intensity over the course of a campaign. Finally, failure to optimize the signal processing settings, especially the detector gain setting, greatly impacts $D_{beam}(d)$. While significant advances have been made to resolve issues relating to contamination and beam quality in newer PDI models, data collected by older models are more prone to variability from these factors and can still occur in newer models if there are changes in the noise level of the environment or if signal processing settings are changed. Therefore, it is important to assess $D_{beam}(d)$ variability over time when re-processing the data.

The automation of the $D_{beam}(d)$ characterization of the sampled data allows us to assess variability over shorter timescales than was previously practical. Prior to this work, PDI data were processed using only one or two estimates of $D_{beam}(d)$ over the course of a campaign. Here we present day-to-day variability in $D_{beam}(d)$ for three field campaigns. When assessed over hourly timescales, we observed no evidence of $D_{beam}(d)$ variability, suggesting that $D_{beam}(d)$ does not vary over the course of any one individual flight (typically 4 to 5 hours in duration) in any of the campaigns analyzed.

Figure 2.15 displays $D_{beam}(d)$ variability during the VOCALS-REx campaign. The PDI laser was replaced immediately prior to this campaign. Figure 2.15 exhibits very little day-to-day variability over the course of the campaign, suggesting that the new laser was operating exceptionally well.

Figure 2.16 displays day-to-day variability in $D_{beam}(d)$ during the MASE field campaign. While $D_{beam}(d)$ variability was quite low, varying by $\sim 10\%$ for drops > 20 µm over the course of the campaign, variability is considered non-negligible. This highlights the importance of our ability to process PDI data on daily timescales. Variability exhibits no obvious temporal pattern, suggesting variability is due to unidentified causes, such as electronic noise in the aircraft environment or optical contamination.

Figure 2.17 displays day-to-day variability in $D_{beam}(d)$ during the POST field campaign which exhibited very high $D_{beam}(d)$ variability as well as a temporal pattern.

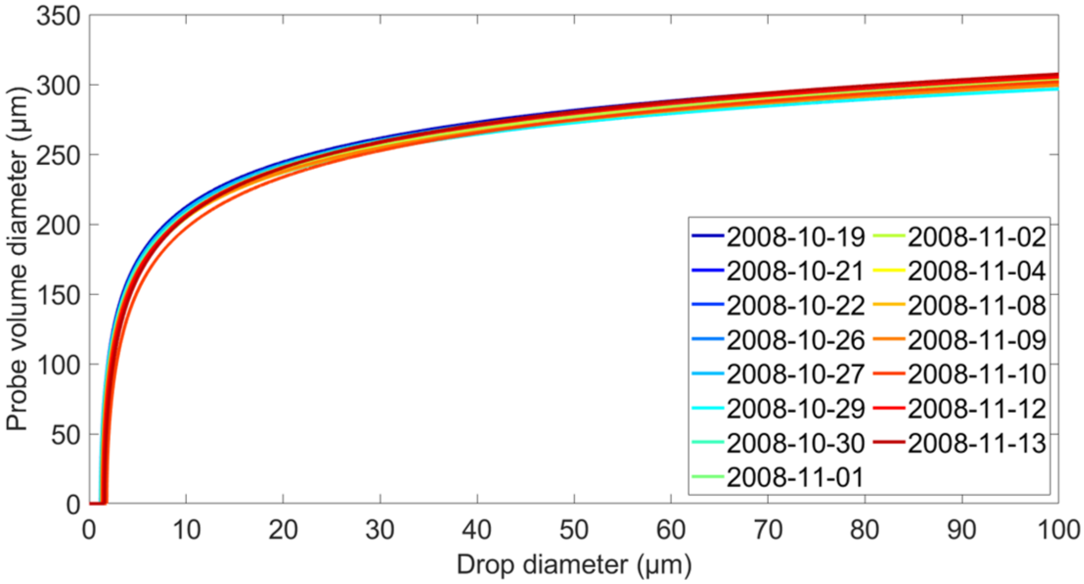

Figure 2.15: Daily variability in $D_{beam}(d)$ during the VOCALS-REx field campaign. Cooler colors represent days earlier in the campaign and warmer colors represent days later in the campaign.

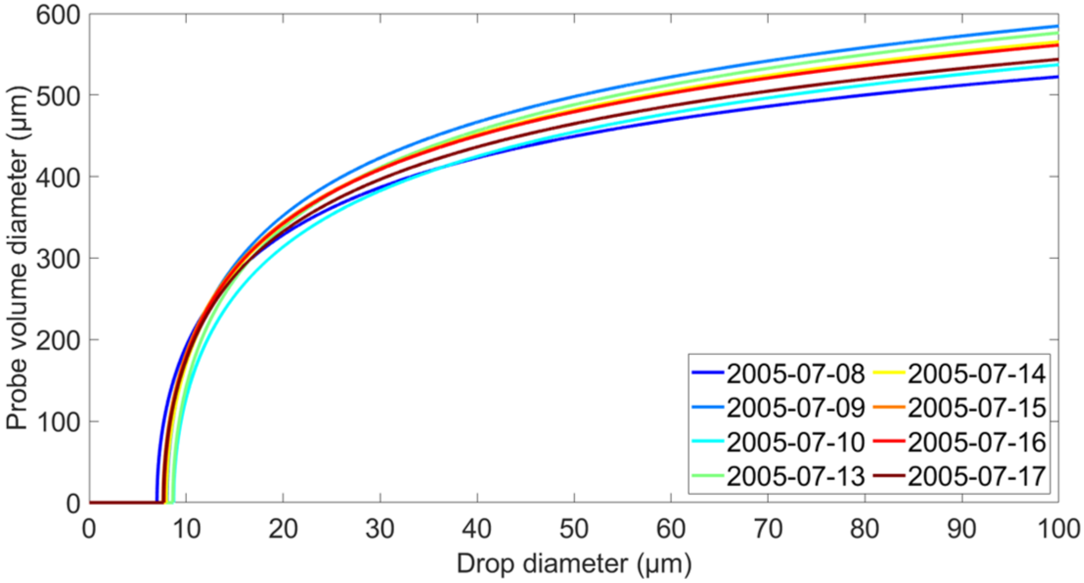

Figure 2.16: Daily variability in $D_{beam}(d)$ during the MASE field campaign. Cooler colors represent days earlier in the campaign and warmer colors represent days later in the campaign.

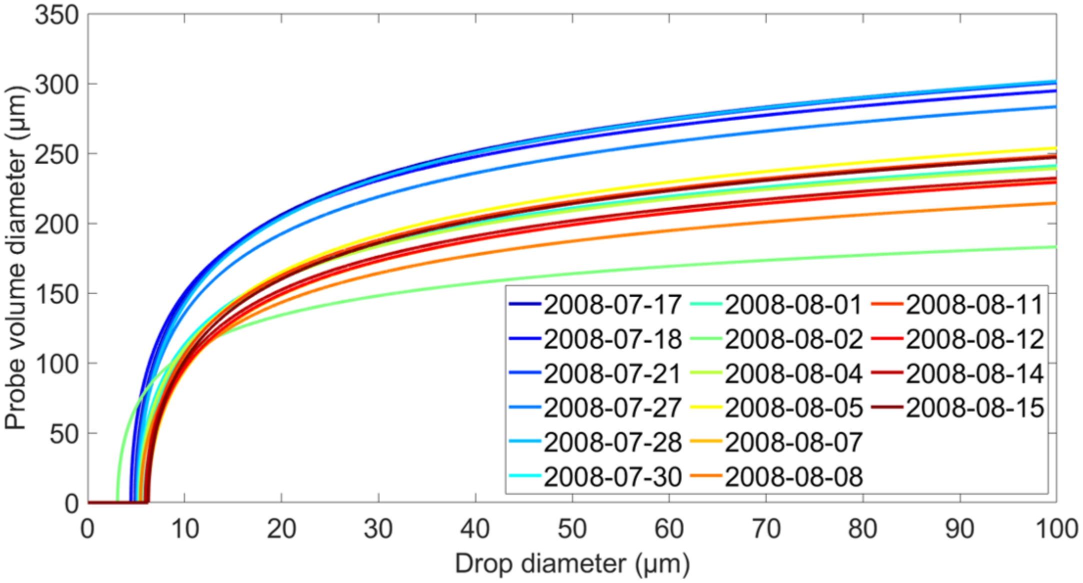

Figure 2.17: Daily variability in $D_{beam}(d)$ during the POST field campaign. Cooler colors represent days earlier in the campaign and warmer colors represent days later in the campaign.

While results from the first five flights look very similar to each other, exhibiting low variability, results change drastically through the remainder of the campaign. It was noted in flight reports that the laser was malfunctioning by the end of the campaign and needed replacement. Though it is difficult to determine when the laser began malfunctioning in in the field, our analysis provides details on instrument capability that allow us to determine when the malfunction began. Not only does variability in probe volume diameter increase drastically following the July-28, 2008 flight, but the $D_{beam}(d)$ fit also deteriorates substantially. While all flights preceding this one exhibited a similar level of agreement with theory as the results shown in Fig. 2.10, subsequent days exhibited a much poorer fit. This suggests that the laser likely began malfunctioning after the July-28, 2008 flight and data collected in subsequent flights should be treated with a greater level of uncertainty.

2.5 Error Analysis

2.5.1 Artificially-generated Data

To quantify the accuracy of our methods, we generate an artificial data set of drop observations in which $D_{beam}(d)$ is known and random error, ϵ, is applied to d, u_d, and t_g. The size distribution and inter-arrival times for the artificial data were chosen to approximate in-cloud observations. Transit length is determined by randomly distributing each drop across a probe volume with a known probe volume diameter, $D_{target}(d)$. $D_{target}(d)$ (Fig. 2.18) represents measurement specifications common in PDI flight probes. Gate time is then calculated from the transit length of each drop assuming a velocity of 55 m/s, a common aircraft velocity.

To test our methodology under conditions which allow gate chop to occur, a subset of the artificial data set is randomly selected to be simulated as gate chop events. Each of the selected events is fragmented into two observations separated in time. The gate time of each of the fragmented events as well as IOT between the two events is selected to reproduce observed gate chop events.

To test our methodology under conditions which allow short gate to occur, a subset of the artificial data set is randomly selected to be simulated as short gate events. The process of simulating short gate events is similar to that of gate chop but with one of the fragmented events removed and IOT recalculated accordingly.

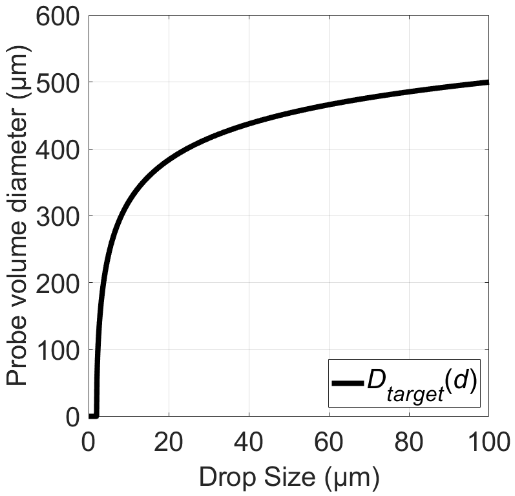

Figure 2.18: Target function chosen to generate artificial data set used to evaluate robustness and accuracy of methodology. K_0 and K_1 (Eq. 2.3) were chosen such that the minimum detectable drop size is 2 µm and D_{beam} reaches a value of 500 µm at a drop size of 100 µm.

We then apply random error to d and $l_{transit}$. Each error combination is simulated 100 times to determine the distribution and mean tendency of our results compared to the target.

2.5.2 Accuracy of Methods

We first assess the robustness of our Standard algorithm with unrealistically large error introduced to each variable. We consider the upper limit of realistic error to be 10% for d and 2% for $l_{transit}$. Therefore, to test the robustness of our Standard algorithm, these values are doubled to 20% error in d and 4% error in $l_{transit}$. Figure 2.19 displays percent error from the target function under these conditions with

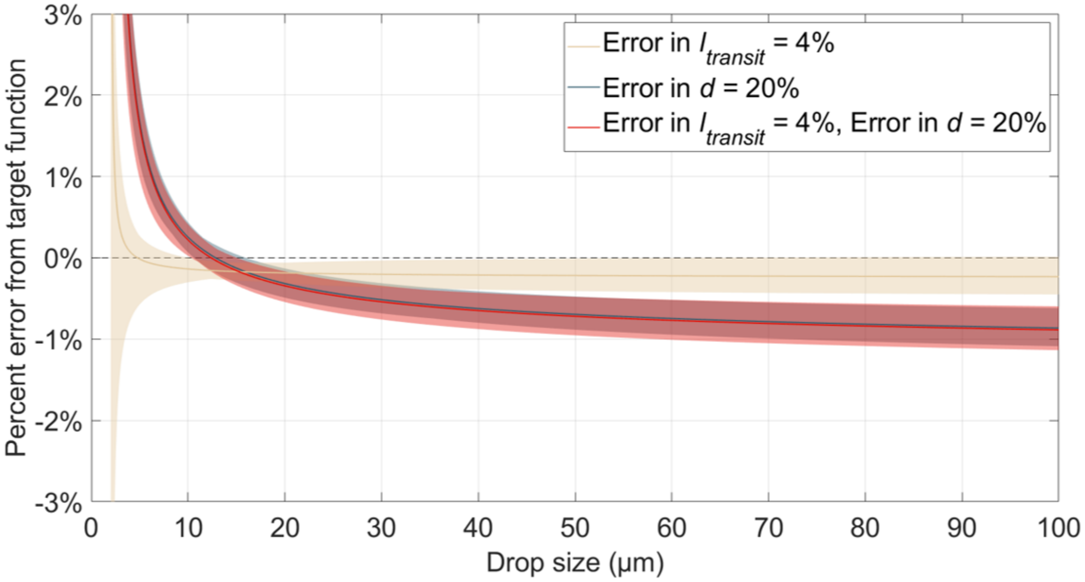

Figure 2.19: Results of methodology for determining probe volume diameter with random error introduced to each variable, displayed as % error from the target, D_{target}. Beige line and envelope represents the case where 4% error is introduced in $l_{transit}$, blue line and envelope represents the case where 20% error is introduced in d, and red line and envelope represents the case where 4% is introduced in $l_{transit}$ and 20% error is introduced in d. Solid lines represent the mean from all 100 simulations and the envelope surrounding each line displays the range of outcomes for the 100 simulations.

positive percent error representing an overestimate of $D_{target}(d)$. Figure 2.19 suggests that our ability to reproduce $D_{target}(d)$ is dominated by error in d as opposed to error in $l_{transit}$. This is evidenced by the fact that percent error is much higher when error is introduced to d measurements only and that these results are nearly indistinguishable to the case where error is introduced to both variables. Even with unrealistic error introduced to both variables, our method produces results that are within $\sim 3\%$ error for all drops greater than 4 μm, suggesting that the method is quite robust.

Next, we assess the accuracy of our algorithms with varying levels of error applied to both variables and with gate chop and short gates simulated (Fig. 2.20). In

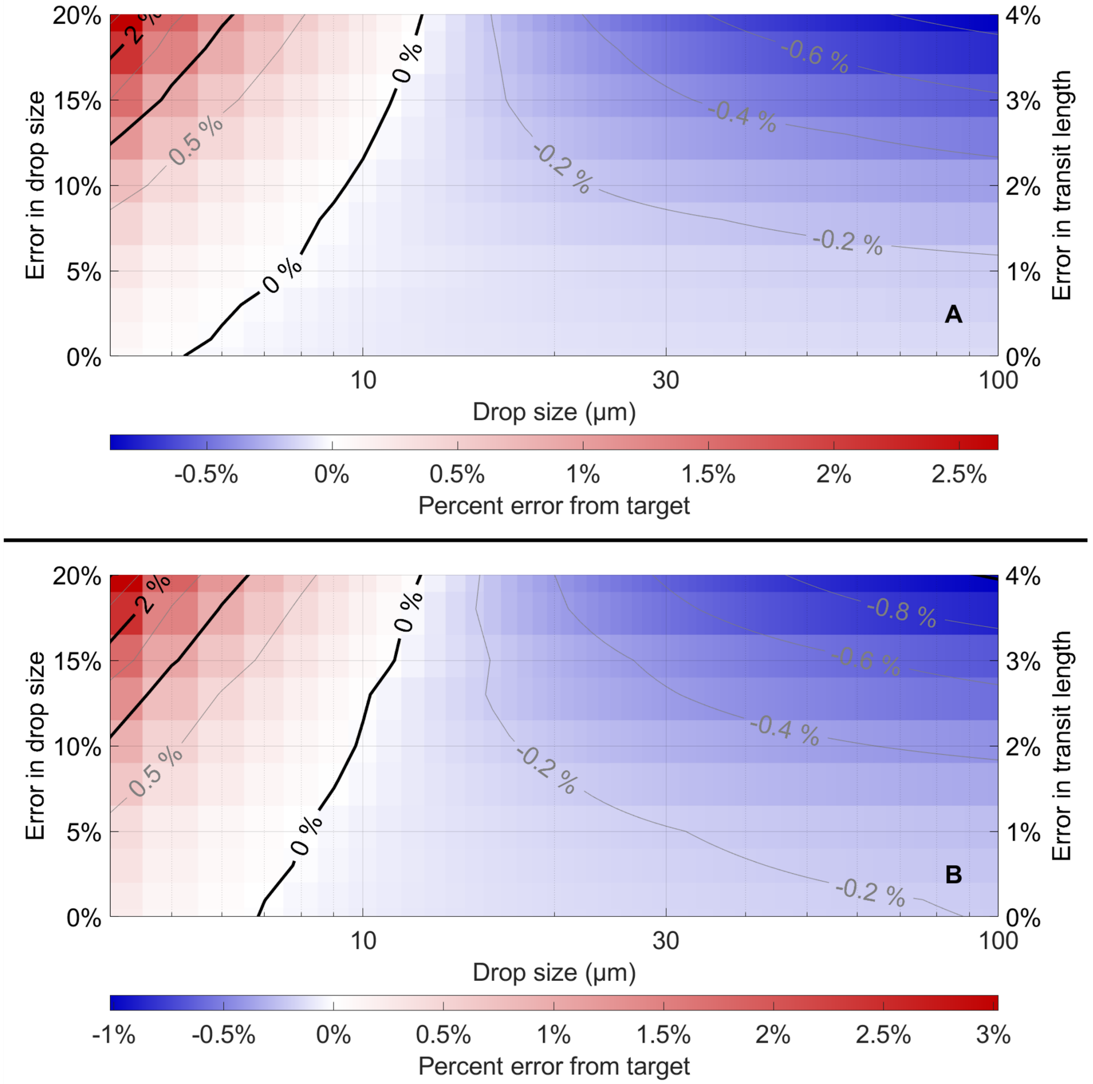

Figure 2.20: Percent error from the target function with various levels of proportional error applied to d and $l_{transit}$ for a) no gate chop or short gate events, b) 25% gate chop events and 25% short gate events. Red represents an overestimate of D_{beam} and blue represents an underestimate of D_{beam}. Black contour lines represent percent error from the target in 1% intervals and grey contour lines represent percent error from the target in 0.2% intervals for values $< 0\%$ and 0.5% intervals for values $> 0\%$.

order to visualize the results, we apply a combination of error to $l_{transit}$ and d where error applied to d is 5× the error applied to $l_{transit}$. Error in $l_{transit}$ ranges from

0%-4% and proportional error applied to d ranges from 0%-20%. Figure 2.20 displays percent error from the target as a function of drop size for a) no gate chop or short gate events and b) 25% gate chop events and 25% short gate events. Results suggests that our algorithms are highly accurate in estimating $D_{beam}(d)$, regardless of error applied to variables or in the presence of gate chop and short gate events. While error is slightly larger in the case with gate chop and short gate events simulated, results are very similar to the case without gate chop and short gate events, suggests that gate chop and short gate events do not significantly impact our ability to determine $D_{beam}(d)$. If we consider the upper limit of realistic error to be 10% for d and 2% for $l_{transit}$, the result of our algorithms are within 1% of the target for all d. Experiments conducted internally by Artium Technologies, Inc., suggest accuracy in d measurements is 2% or lower and a fraction of a percent in $l_{transit}$. For these values, our algorithms generate results which are nearly indistinguishable from the target. This suggests that our methods are highly accurate under realistic sampling conditions, regardless of the presence of gate chop and short gate events.

2.6 Conclusions

We present a new empirical method in which the determination of $D_{beam}(d)$ is automated using *in situ* PDI measurements. Methods to identify and reconstruct gate chop events are described and an augmented algorithm is presented to characterize $D_{beam}(d)$ in the presence of frequent short gate events.

Applying our methods to measurements collected in a controlled laboratory setting suggests that our methods produce favorable results and instrumentation is performing as theory predicts. When applied to aircraft observations, our results imply that the results of our methods align with theory and can be successfully implemented to aircraft measurements.

Our methods are applied to three field campaigns and suggest small day-to-day variability in $D_{beam}(d)$, likely due to variations in the electromagnetic noise in the environment. Using our methods, we are able to identify circumstances in which the PDI is not performing adequately due to laser malfunction. Our technique accounts for any prevailing conditions and can be used to accurately characterize $D_{beam}(d)$ in a variety of conditions.

The robustness and accuracy of the methodology are tested using an artificially-generated data set in which $D_{beam}(d)$ is known and random error is applied to each of the measured variables. We find that our methods are highly robust, even with unrealistic levels of error introduced to the measurements and the accuracy of our method is dominated by error in d measurements, as opposed to error in $l_{transit}$. Our method produces the most accurate results in the absence of gate chop and short gate events but exhibits a similar level of accuracy when these events are simulated. Under realistic conditions, we find that our method is accurate to within 1% or less.

Chapter 3

A Novel Technique to Characterize Phase-Doppler Interferometer Probe Volume Width from Laboratory Measurements

Abstract

To obtain accurate estimates of cloud properties from PDI measurements, probe volume width, W, characterization is essential. W has typically been assumed to be a known fixed value based on the optical configuration of the instrument. We seek to assess the validity of this assumption using theoretical calculations and laboratory measurements. Our theoretical calculations suggest a functional dependency of W on d. To explore this relationship, we constructed a device which can be used to

directly measure W in a laboratory setting. In order to account for any changes made to detector gain, we use the maximum intensity registered as a drop passes through the most intense region of the probe volume, I_{max}, as a metric for W. Our results suggest a well-constrained relationship between I_{max} and W and suggest that W is not a fixed value. When applying our methods to aircraft observations, we observe good agreement between each channel of a dual-range PDI, yielding confidence that our W characterization is accurate.

3.1 Introduction

While techniques have been developed to characterize D_{beam} empirically from *in situ* measurements (see Chapter 2), W has typically been assumed to be a known fixed value based on the optical configuration of the instrument (Chuang et al. 2008). Due to the use of a slit aperture, only drops that pass near the center of the beam intersection, along the beam axis, are detected by the PDI (Fig. 3.1). Drops transiting near the center of the intersecting beams scatter light which passes through the aperture (Fig. 3.1a) but drops passing further from the center of the beam intersection scatter light which is blocked by the aperture (Fig. 3.1b). The length of the aperture, L_{aper}, and detection angle, θ, therefore determine the distance along the beam axis in which drops may be detected. In practice, there is also a magnification factor which must be accounted for due to the ratio of the front and back focal lengths in the receiver, F_f and F_b, respectively. Therefore, the theoretical probe volume width, W_c, typically

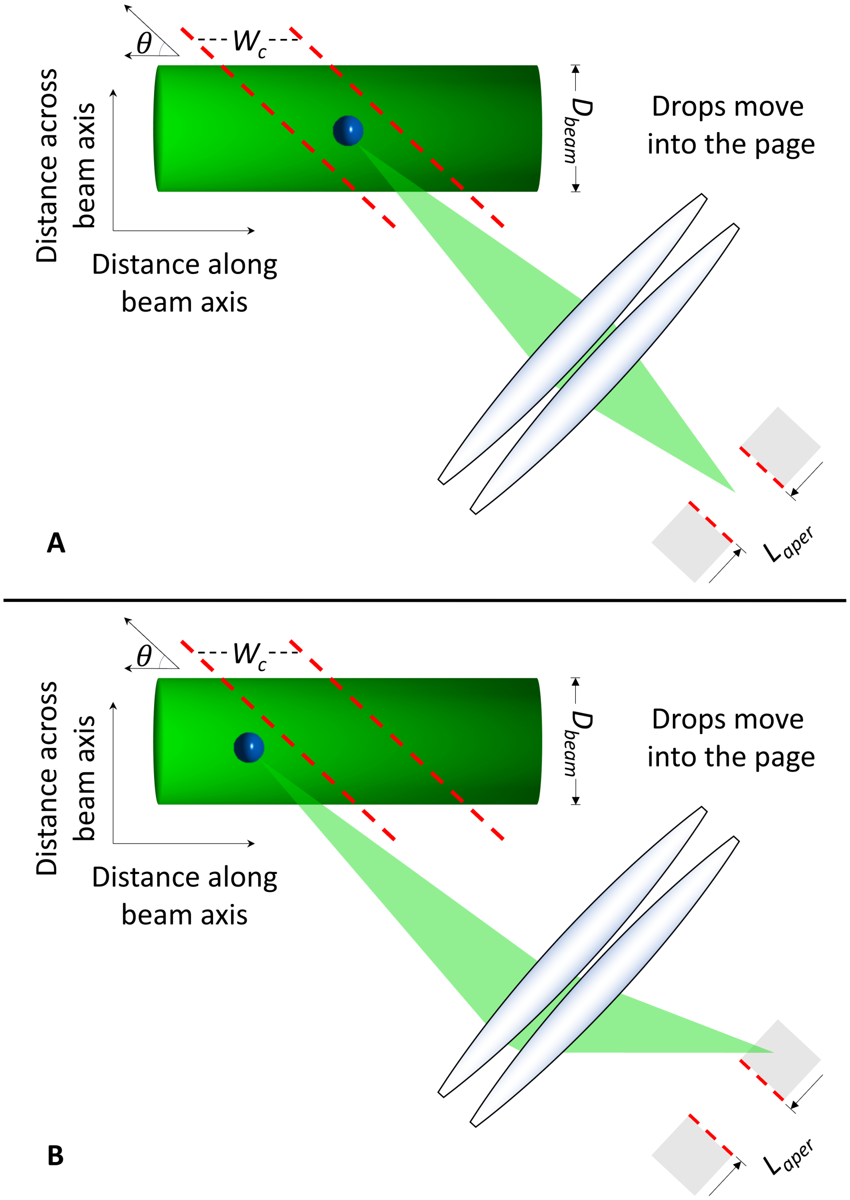
θ
W_c
Distance across beam axis
Distance along beam axis
D_beam
Drops move into the page
L_aper
A
θ
W_c
Distance across beam axis
Distance along beam axis
D_beam
Drops move into the page
L_aper
B

Figure 3.1: Diagram illustrating how a slit aperture is used to limit the spatial extent at which drops may be detected. The drop in a) transits the probe volume near the center of the intersecting beams and scattered light is allowed to pass through the aperture and the drop is detected. The drop in b) transits the probe volume further from the center of the intersecting beams and scattered light is blocked by the aperture and the drop is not detected.

used in data processing is:

$$W_c = \frac{L_{aper}}{\sin\theta} \times \frac{F_f}{F_b} \tag{3.1}$$

To our knowledge, research has not been published to confirm the accuracy of W_c.

A second assumption made is that W does not vary as a function of d. However, this is only the case if illumination is constant along the beam axis (i.e., intensity contours are parallel to the beam axis). As described in the next section, theory suggests that, for sufficiently small drops, this assumption may not be valid, suggesting that W may have a functional dependence on d for small drops. In this work, we test if W varies as a function of d through theoretical calculations and laboratory measurements.

3.2 Theoretical Calculations

Here, we establish a theoretical framework for understanding the relationship between W and d. Our goal is to determine theoretically the relevance of W variations with d for drop sizes relevant to the PDI.

We first construct a mathematical model which describes the three-dimensional distribution of intensity for two intersecting beams where each beam has a Gaussian intensity profile. The defined coordinate system used for our model is depicted in Fig. 3.2.

The irradiance profile of a single Gaussian beam is calculated as:

$$E(r) = E_0 e^{-2r^2/w(z)^2} \tag{3.2}$$

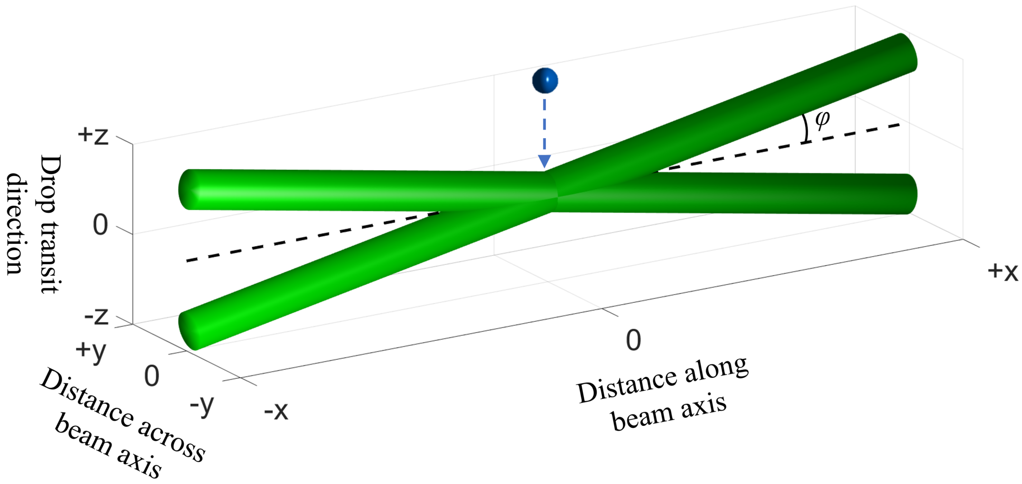

Figure 3.2: Intersection of two beams in the defined coordinate system. Two identical beams intersect each other at the origin of the coordinate system. Each beam axis is on the x-z plane with each respective beam intersecting the x-axis at an angle of φ and $-\varphi$. Using this coordinate system, the fringe plane is parallel to the x-y plane and drops transit the probe volume in the z-dimension.

where E is irradiance, E_0 is the peak irradiance located at the center of the beam, r is the perpendicular distance from the beam axis, and $w(z)$ is the radius at which beam irradiance decreases to $1/e^2$ of E_0. While $w(z)$ changes as the beam propagates through space, converging to a minimum value of w_0 referred to as the beam waist, here we assume $w(z) = w_0$ as lasers used in PDI are highly collimated, producing very low beam divergence. Additionally, due to the use of a collimated laser, we may assume irradiance is equal to intensity, I, and replace $E(r)$ and E_0 in Eq. 3.2 with $I(r)$ and I_0:

$$I(r) = I_0 e^{-2r^2/w_0^2} \tag{3.3}$$

The intensity at any point near the intersection is the sum of intensities contributed from each beam at that point. From Eq. 3.3, we can calculate the spatial distribution of intensity as:

$$I_p(r_1, r_2) = I_0(e^{-2{r_1}^2/{w_0}^2} + e^{-2{r_2}^2/{w_0}^2}) \tag{3.4}$$

where I_p is the intensity at point $p(x, y, z)$ and r_1 and r_2 is the perpendicular distance from point $p(x, y, z)$ to Beams 1 and 2, respectively. The model neglects to account for the fringe pattern produced by the two beams. For our purposes, this is permissible as the cross-sectional sample area of the measurement volume and the fringe plane are parallel to each other so sample area is unaffected by the fringe pattern.

The size of the effective sample volume is larger for large drops and smaller for small drops. This is because large drops scatter more light than small drops so they are able to transit less intense portions of the probe volume and still be detected, whereas a small drop with the same trajectory would not be detected. Therefore, contours of intensity reveal the geometry of the effective sample volume for different drops sizes. However, because we are only interested in the effective sample area, represented by the x-y plane in the defined coordinate system, and relative intensity peaks for the x-y plane where $z = 0$, taking a cross-section of the probe volume at $z = 0$ represents the intensity distribution of the sample area.

Figure 3.3 displays the normalized intensity distribution of the sample area. Larger contours represent the effective sample area for larger drops. We see that the horizontal length of each contour, representing W, does indeed decrease with decreasing d. If we include an aperture in the receiver of some arbitrary width (red dashed line in Fig 3.3), we see that W_c is a very good approximation of W for large drops, assuming drops are not detected outside of the aperture boundaries. However, for smaller drops, W becomes smaller than W_c and W_c is no longer a good approximation of W. This implies that, for drops smaller than some threshold value, W has a functional dependence on d.

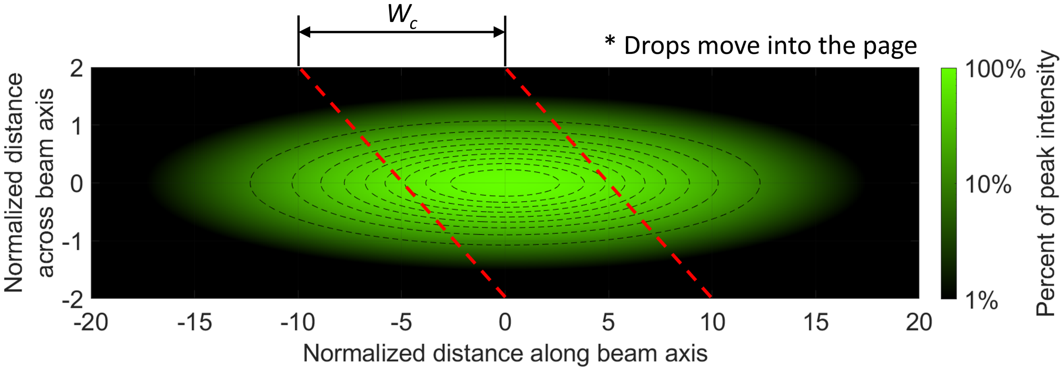

Figure 3.3: Intensity distribution of the effect sample area of a PDI. Black dashed lines represent contours of intensity in 10% intervals. Red dashed lines represent arbitrary aperture boundaries.

3.3 Experimental Methods

3.3.1 Overall Approach

Next, we seek to characterize W through laboratory measurements and apply the characterization to flight data. While $D_{beam}(d)$ may be characterized by analyzing the distribution of transit lengths, as was discussed in Chapter 2, there is currently no way to determine the location at which a drop passes through the sample volume in the dimension along the beam axis (i.e., the x direction in Fig. 3.2). Thus, new methods must be developed to characterize W.

One issue that arises in characterizing W as a function of d is that the relationship is not the same for all detector gain settings. Detector gain is a setting which amplifies or dampens the incoming signal. If the detector gain is increased then the effective sample area for all drop sizes increases, which changes the $W(d)$ relationship. Therefore, we introduce a new variable which can be used as a metric for W that is applicable across all gain settings, and exhibits a well-constrained relationship with W independent of detector gain and d.

We propose using the maximum intensity detected as a drop transits through the most intense portion of the measurement region, I_{max}, as our independent variable. I_{max} is a function of both detector gain and d. If well-constrained relationship exists between W and I_{max}, the relationship should remain the same independent of both detector gain and d. Additionally, I_{max} can be easily estimated from both laboratory and aircraft measurements and conveniently, we can characterize $W(I_{max})$ over a large range of I_{max} simply by varying either the detector gain or d.

In order to determine the relationship between W and I_{max} in controlled laboratory setting, we:

1. Transit a stream of monodisperse drops along the beam axis to directly measure W and I_{max} at a single detector gain setting.
2. Repeat over a range of drop sizes and detector gain settings to obtain W over a range of I_{max}.

Next, to apply the laboratory-measured relationship between W and I_{max} to aircraft measurements, we:

1. Determine I_{max} for each d bin by analyzing the distribution of aircraft-measured intensities.
2. Insert aircraft-measured I_{max} for each d bin into the laboratory-measured $W(I_{max})$ relationship to determine W for each d bin.

3.3.2 Measurement Technique

In order to obtain accurate W measurements, we designed and constructed a system which is capable of obtaining multiple W measurements at varying locations across the beam axis. The Probe Volume Scanner (hereafter "Scanner," Fig. 3.4) is composed of two one-dimensional stage micrometers which are fixed to each other at a 90° angle so that two-dimensional travel is achieved. Each stage is driven by an individual step motor which is controlled by a microcontroller programmed to perform a predefined pattern. A monodisperse drop generator (MDG), which projects a stable stream of monodisperse drops of known size, is connected to the 2-D stage setup. The MDG pumps water at an adjustable flow rate to a metal plate orifice. The metal plate orifice is connected to a piezoelectric transducer controlled by a frequency generator to initiate drop breakup at a known frequency (see Wu et al. 2007 for more information on MDGs). The known MDG frequency, f_{MDG}, and flow rate, Q_{MDG}, are then used to calculate drop size, d_{MDG} as:

$$d_{MDG} = \sqrt[3]{\frac{6Q_{MDG}}{\pi f_{MDG}\rho_w}} \tag{3.5}$$

where ρ_w is the density of water.

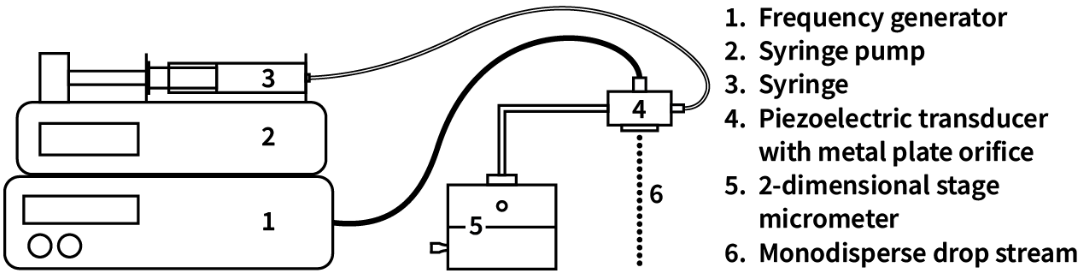
3
2
1
4
5
6
1. Frequency generator
2. Syringe pump
3. Syringe
4. Piezoelectric transducer with metal plate orifice
5. 2-dimensional stage micrometer
6. Monodisperse drop stream

Figure 3.4: Probe Volume Scanner schematic displaying key components.

There are multiple advantages to using the Scanner as opposed to measuring W manually with a single stage micrometer. First, the Scanner allows for faster measurement of each dimension. Because the MDG is less stable over longer time periods, faster measurements result in more accurate characterization. This method also allows us to collect multiple measurements of W at varying location across the probe volume which can then be averaged to provide a more accurate estimate of W.

Once the Scanner is appropriately aligned with the PDI, the stages are programmed to perform a raster pattern which allows the stream to enter and exit the probe volume at different locations across the beam axis and collect multiple measurements across the entire probe volume (Fig. 3.5).

Lastly, we calculate W for each leg by analyzing the time-resolved data rate measured by the PDI. The edges of detectability are defined as the timestamps in which the data rate increases above a threshold value and then decreases below at the other end. We define this threshold as being 50% of the f_{MDG} frequency. We then multiply the difference in time between the stream entering and exiting the probe volume by the translational velocity of the Scanner to get an estimate of W for each leg.

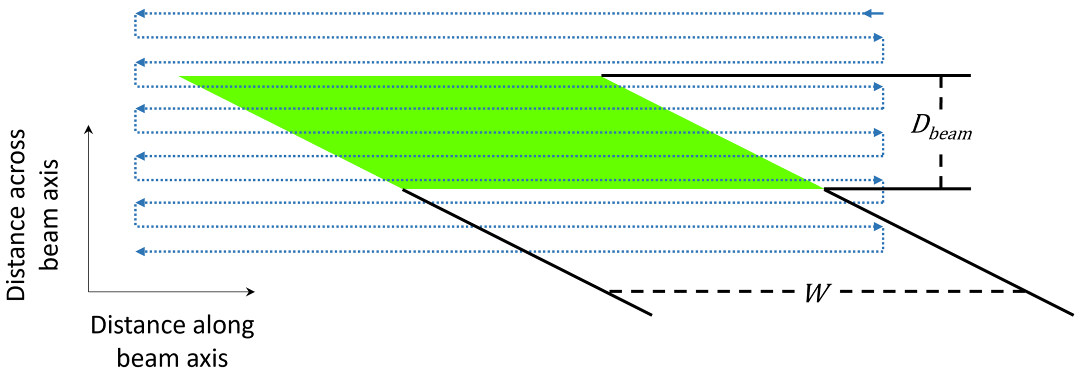

Figure 3.5: Diagram showing the raster pattern performed by the Scanner relative to the PDI sample area. Blue dotted line and arrows represent the pathway taken by the Scanner.

3.4 Results and Discussion

3.4.1 Laboratory measurements

We first analyze laboratory results of probe volume scans collected by the Scanner. Table 3.1 displays the relevant optical properties of the dual-range PDI instrument used for this analysis.

We first analyze the results of one leg from an individual scan collected on Channel 2 of the described instrument. Figure 3.6 displays the time-resolved data rate measured by the PDI as a percentage of f_{MDG} for one leg of the scan. As seen in Fig. 3.6, the measured PDI data rate rapidly increases to near 100% of f_{MDG} as the stream enters the probe volume, stabilizes at this value, and rapidly decreases to 0% as the stream exits the probe volume. Using a threshold of 50% of f_{MDG}, we identify the time stamps associated with the stream entering and exiting the probe volume. However, because edges are well defined, we estimate that W measurements are quite

	Channel 1	Channel 2
Slit Aperture, L_{aper}	400 µm	400 µm
Collection Angle, θ	30°	30°
Receiver Front Focal Length, F_f	100 mm	121 mm
Receiver Back Focal Length, F_b	75 mm	65 mm
Theoretical Probe Volume Width, W_c	1067 µm	1489 µm

Table 3.1: Relevant optical properties of the dual-range PDI instrument used in this study.

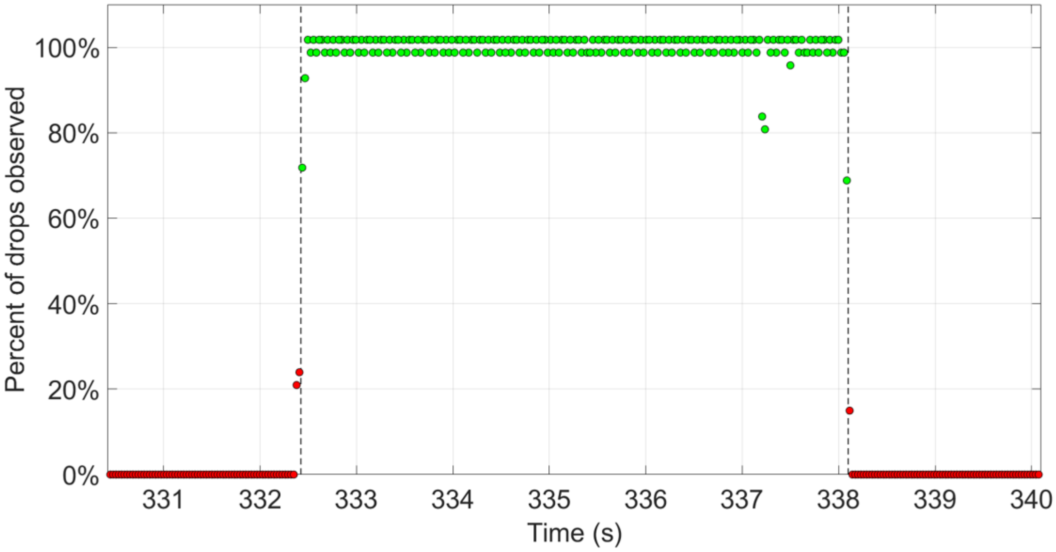

Figure 3.6: Time series of data rate measured by a PDI instrument as a percentage of MDG frequency for one scan leg. For this scan, the MDG was projecting a stable stream of 191 µm drops. Red points represent times when the measured data rate of the PDI was below 50% of f_{MDG} and green points represent times when the measured data rate of the PDI was above 50% of f_{MDG}. Vertical dotted lines represent the time stamps associated with the stream entering and exiting the probe volume according to our methods.

insensitive to this threshold.

Next we present results for our determination of I_{max} for the same scan. Figure 3.7 displays the time series of retrieved drop intensities. As expected, the time series of intensity for the scan exhibits a Gaussian envelope. This is because the beams have a Gaussian intensity profile. Legs which take place earlier or later in the scan will be near the edges of the Gaussian profile and register a lower intensity, with intensity peaking in the middle of the profile along the beam axis. We estimate I_{max} by taking the 99^{th} percentile of the intensity distribution for the centermost leg.

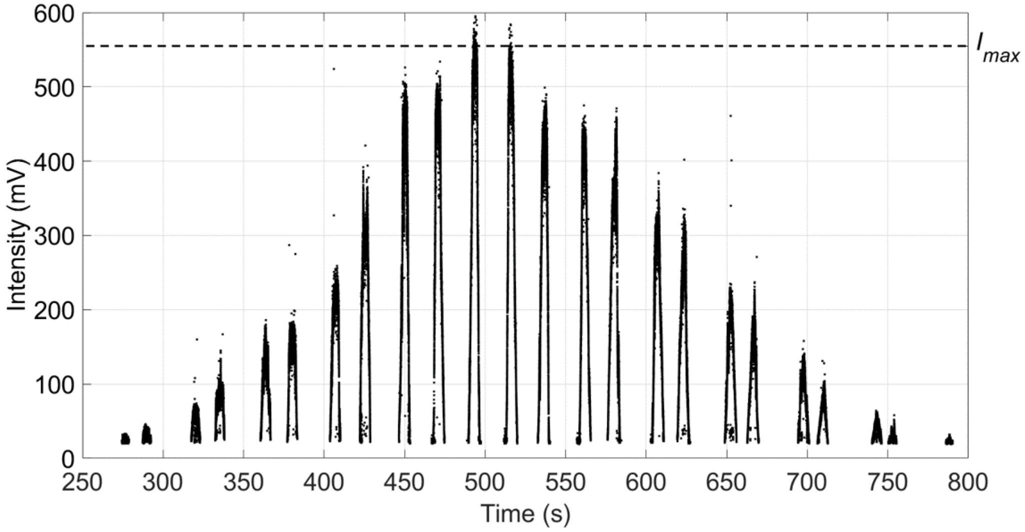

Figure 3.7: Time series of retrieved drop intensities from a single scan on Channel 2. Each "spike" is a single transit across the view volume, i.e., the width of each spike is a separate determination of W.

Here, we present Channel 1 scan results, varying both drop size and detector gain values so that we may determine $W(I_{max})$ (Fig. 3.8). As seen in Fig. 3.8, for values of I_{max} greater than 150 mV, W stabilizes to the theoretical value W_c. This is the expected result and implies that the aperture is very effective in blocking the scattered signal of drops that transit further from the center of the beam intersection, as intended. $W < W_c$ was measured for 0 mV $< I_{max} <$ 150 mV. This result confirms the prediction of our theoretical calculations (Section 3.2) that W_c is not constant for all d. In theory, however, W should decrease to a value 0 for I_{max} of the smallest detectable drop. More measurements are needed for $I_{max} <$ 150 mV in order to more accurately determine W in this region.

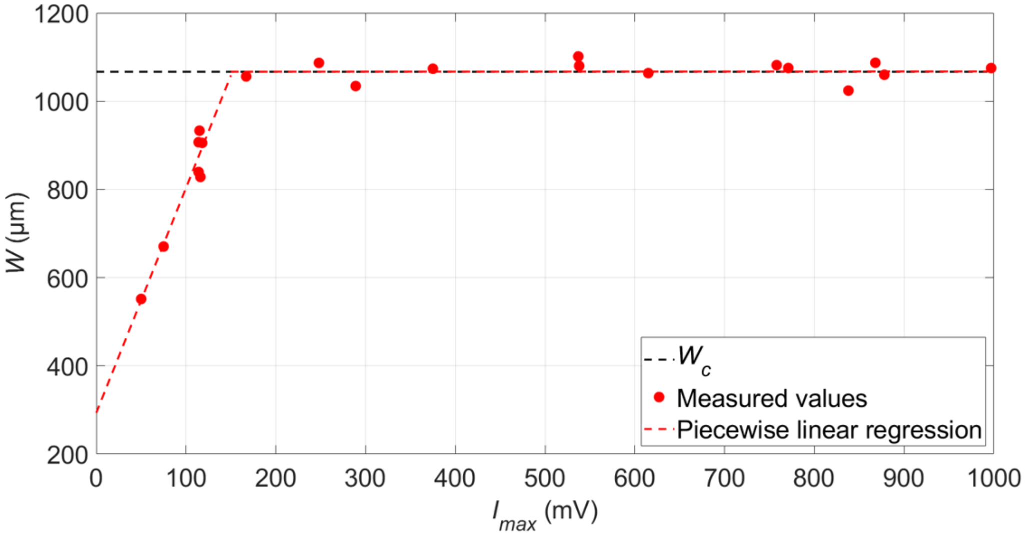

Figure 3.8: Measured and fitted relationship between W and I_{max} for Channel 1. Fitted relationship was obtained by performing piecewise linear regression with the boundary point set to 150 mV.

In order to use the laboratory-measured relationship between W and I_{max} to process flight data, we must estimate W for all values of I_{max} from the measurements. To estimate $W(I_{max})$, we perform a piecewise linear regression with the boundary point set to 150 mV. We believe this to be a good representation of $W(I_{max})$ for $I_{max} >$ 150mV as very little W variability occurs. However, for $I_{max} <$ 150mV very few measurements were acquired and the line of best fit does not reach a value of 0 as theory predicts. This may be because a linear relationship is not appropriate for $W < W_c$. More measurements are needed in this region to investigate the relationship in further detail. Until we can do so, our plan is to not report measurements at low values of I_{max} where W is highly uncertain.

Next, we present results from tests performed on Channel 2 (Fig. 3.9). The results are surprising as all measured values of W are larger than the theoretical value, W_c. While it is possible that this is the result of error in the values used to calculate W_c, this is unlikely as each variable is known with high accuracy and our measurements suggest a larger discrepancy than realistic error analyses could predict. Furthermore, our measurements suggest a nonlinear relationship between W and I_{max}. If the discrepancy were due to error in the estimate of W_c, one would expect W to plateau at a constant value.

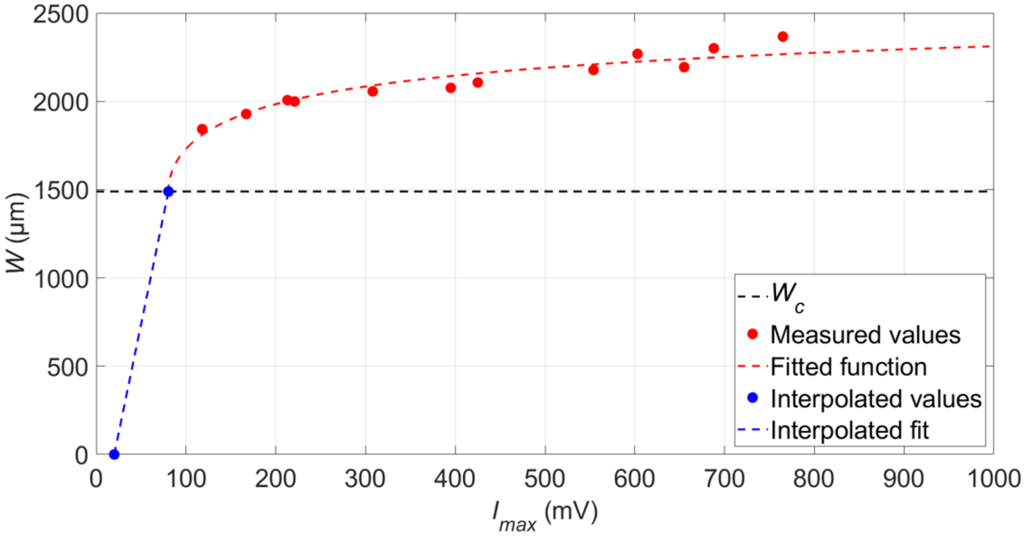

Figure 3.9: Measured and fitted relationship between W and I_{max} for Channel 2. Red dashed line represents the best fit to observations using Eq. 3.6. Blue points and dashed line represents interpolated values based on the red fitting and I_{max} for the smallest detectable drop.

These results imply that drops are being detected outside of aperture boundaries. This is a possibility if the image of the scattered signal is in poor focus or if the lens resolution is inadequate. Image blur is determined by the resolution of the receiving optics and if the resolution is less-than-ideal, the edges of the sample area will be ill-defined. This results in a so-called "circle of confusion", or "blur circle," which allows light scattered by drops that traverse the probe volume outside aperture boundaries to pass to the detector. While blur circles have been well documented in imaging applications (e.g., Lee 1990; Miks and Novak 2012; Sezan et al. 1991; Vivirito et al. 2002), the effect of a blur circle on the scattered signal for a PDI is unclear. However, we suspect a blur circle to be the cause of the discrepancy observed in Channel 2. This further highlights the need for direct W measurement.

Next, we attempt to establish the $W(I_{max})$ relationship using the acquired data. The interplay between the aperture and the blur circle and their effects on the scattered signal and W is not well-understood. However, the problem appears to be analogous to the relationship between D_{beam} and d as the it concerns the growth rate of a circle as a function of I_{max}, which is closely related to d. Therefore, we attempt to fit a function closely resembling Eq. 2.3, with a few modifications. We replace D_{beam} with W and d with $\sqrt{I_{max}}$, as I_{max} is proportional to d^2, and sum the result with W_c, as we must include the distance at which drops are detected within aperture boundaries. This yields:

$$W(I_{max}) = \sqrt{k_0 + k_1 \ln \sqrt{I_{max}}} + W_c \tag{3.6}$$

where k_0 and k_1 are constants. While more work is needed to determine if this is an accurate representation, applying this function yields good agreement with measured values (red dashed line in Fig 3.9). Because data was not collected for $I_{max} < 100$ mV, we must interpolate $W(I_{max})$ in this region. Theory predicts W should decrease to a value of 0 for I_{max} of the smallest detectable drop size. From analysis of the distribution of measured intensities, we estimate this value to be 20 mV. We then assume a linear fit between this value and the point where the fitting acquired using Eq. 3.6 intersects W_c (blue points and dotted line in Fig. 3.9). While additional measurements are required to confirm that the interpolation is accurate, we believe this to be a reasonable approach as the fitting provides very good agreement in the overlap region between the two channels, as will be discussed in the next section.

3.4.2 Application to Aircraft Measurements

Once $W(I_{max})$ is established by laboratory measurements, $W(d)$ may be determined by quantifying I_{max} for each d bin from in-flight data and applying the $W(I_{max})$ relationship. Here we apply our methods to data collected during the Southern California Interactions of Low Clouds and Land Aerosol (SCILLA) experiment which took place in June of 2023. Figures 3.10 and 3.11 show bivariate histograms of drop counts for the June 15, 2023, flight in drop size-scattering intensity space for Channels 1 and 2, respectively. To determine I_{max} for each bin, adequate statistics must be acquired. Therefore, only bins which recorded > 1000 drops for Channel 1 and > 100 drops in Channel 2 are included in the analysis. I_{max} is then computed for each drop size bin which meet the criteria as the 99^{th} percentile of measured intensities for that bin (red points in Figs. 3.10 and 3.11). A 2^{nd}-degree polynomial is fitted to the data to determine $I_{max}(d)$. A 2^{nd}-degree polynomial is appropriate here as scattering intensity is proportional to d^2. The fitted function displays as the dashed red lines in Figs. 3.10 and 3.11 which show very good agreement with the measured values, suggesting that the obtained measurements are performing as theory predicts. After $I_{max}(d)$ has been established from in-flight measurements, the laboratory-derived $W(I_{max})$ relationship is used to determine $W(d)$.

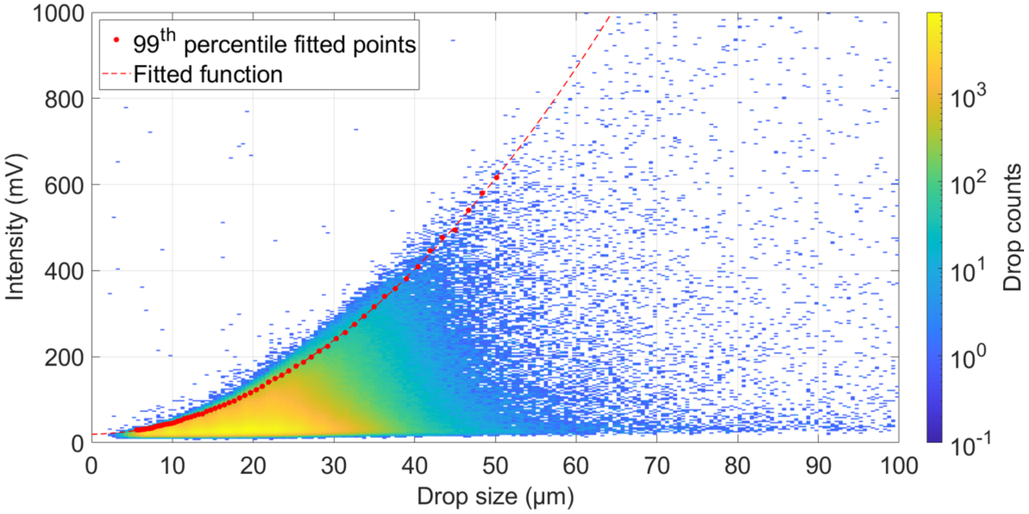

Figure 3.10: Bivariate histogram of drop counts in drop size-scattering intensity space for Channel 1 for data collected of the June 15, 2023, flight of the SCILLA field campaign. Red points represent the 99^{th} percentile for each d bin and red dashed line represent the best fit 2^{nd} degree polynomial to the points.

Using $W(d)$ and $D_{beam}(d)$, determined using methods outlined in Chapter 2, drop size distributions were then calculated. Here we focus on size distributions measured by each individual channel, with particular emphasis on the overlap region between channels to validate our methods. We would like to emphasize that, although each channel is contained within the same housing, the only similarity between the two

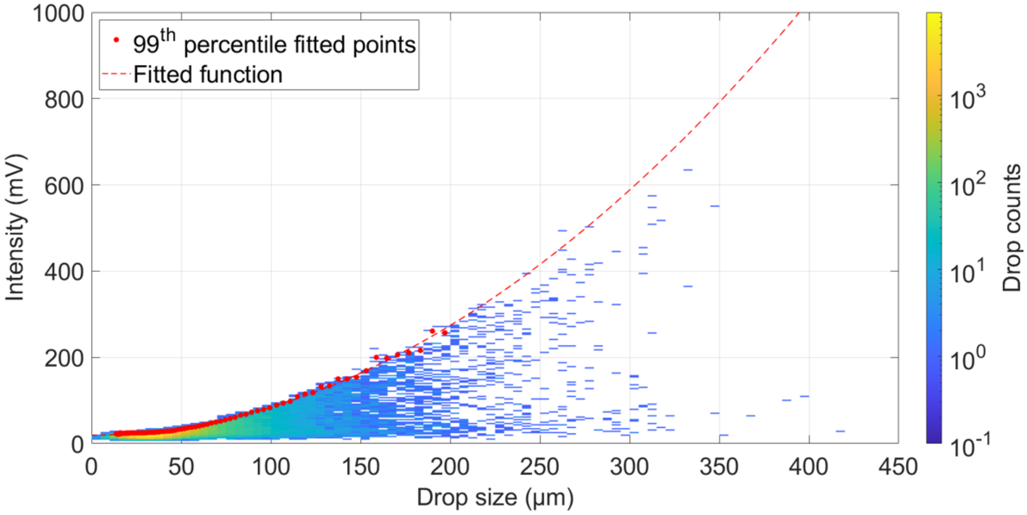

Figure 3.11: Bivariate histogram of drop counts in drop size-scattering intensity space for Channel 2 for data collected of the June 15, 2023, flight of the SCILLA field campaign. Red points represent the 99^{th} percentile for each d bin and red dashed line represent the best fit 2^{nd} degree polynomial to the points.

channels is that they use the same laser. However, after the laser is split, each channel contains its own transmitting optics, receiving optics, aperture, set of detectors, and signal processor and each channel is calibrated separately. Therefore, the two channels may be regarded as two separate instruments nearly independent of each other and comparison between the two channels may be regarded as comparison between separate instruments.

Figure 3.12 displays number concentration as a function of drop size calculated for each respective channel averaged over the June 15, 2023, flight. Results show very good agreement in the overlap region between the two channels (shaded area in Fig. 3.12). This yields confidence that our methods of determining W in each of the channels are valid. Small discrepancies do exist between the two channels in which Channel 2 slightly overestimates drop concentration relative to Channel 1 in the drop

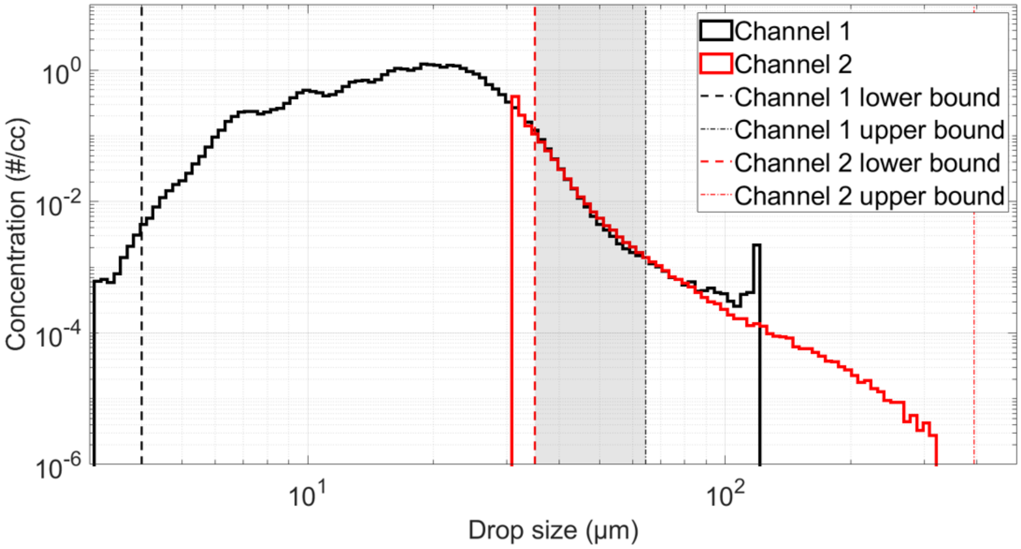

Figure 3.12: PDI-measured number concentration for each respective channel averaged over the June 15, 2023, flight of the SCILLA field campaign. Vertical dashed lines represent the upper and lower bounds for each respective channel and the shaded area represents the overlap region. Upper boundaries were determined as the drop size in which I_{max} reaches saturation at 1000 mV in Figs. 3.10 and 3.11. Lower boundaries were determined estimated as 4 µm and 35µm for Channels 1 and 2, respectively, from $D_{beam}(d)$ analysis.

size range of 45 µm to 63 µm. However, these discrepancies are quite small, peaking at 29% overestimation in Channel 2 relative to Channel 1 at a drop size of 56 µm. This is likely due to the interpolation performed in the $W(I_{max})$ analysis for Channel 2 (Fig. 3.9). Our findings also suggest that the upper boundary and lower boundary of Channels 1 and 2, respectively, may be extended as agreement between the two channels extends outside of the determined overlap region, down to 32 µm at the lower end and up to 80 µm at the upper end. Lastly, we emphasize that measurements obtained for Channel 1 in the overlap region are considered highly accurate as D_{beam} and W experience very small deviations over this range. While Channel 2 D_{beam} and W is confronted with much larger variability over the same range, concurrence with

Channel 1 yields confidence that our methods of determining $W(I_{max})$ are justified and produce accurate results.

3.5 Conclusions

In this work, we explore the relationship between W and d through theoretical calculations and laboratory measurements. While W has typically been assumed to be a known fixed value based on the optical configuration of the instrument, we hypothesize that W is a function of d. To test this hypothesis from a theoretical standpoint, we generate a simple mathematical model which describes the distribution of intensity for two intersecting beams and find that theory predicts a functional dependency of W on d. To investigate this relationship further, we designed and constructed a device which, when used in conjunction with a PDI, allows for direct W measurement in a controlled laboratory setting. The device is composed of two stage micrometers anchored to a MDG which projects a stream of monodisperse drops that transit each dimension of the probe volume. As the stream passes through the probe volume, PDI data is collected and the time-varying data rate is analyzed to determine the edges of detectability, allowing for direct W measurement.

To account for any changes made to detector gain and allow laboratory-measured data to be applied to aircraft measurements, we introduce a new variable, I_{max}, which is used as a metric for W in place of d. We determine the relationship between W and I_{max} for each channel of a dual-range PDI through laboratory measurements and present our results. For Channel 1, our measurements suggest that W

is less than W_c at lower values of I_{max}. This result is consistent with the findings of our theoretical calculations and implies a functional dependence of W on d. For values of I_{max} greater than 150 mV, W plateaus to the theoretical value, suggesting that the aperture is effective in blocking the scattered signals of drops not intended to be measured. For Channel 2, all measurements of W were greater than W_c. We interpret this as the result of less-than-ideal resolution in the receiving optics which generates a blur circle and allows drops to be detected outside the spatial range dictated by the aperture. These results further highlight the need for direct W measurement.

Lastly, we apply the laboratory-measured $W(I_{max})$ relationship to aircraft data collected during the SCILLA field campaign. When comparing drop number concentration measured by each respective channel, we find very good agreement in the overlap region between the two channels. Measurements obtained by Channel 1 in the overlap region are considered highly accurate as variability in both W and D_{beam} is very low in this region. While Channel 2 is confronted with much higher variability over the same region, concurrence with Channel 1 suggests that W characterization in Channel 2 is accurate, yielding confidence in our methods.

Chapter 4

Particulate Matter Emissions from Cooling Tower Drift Droplets

Abstract

Wet cooling towers are used in industrial processes, power plants, and heating, ventilation, and air conditioning systems. Their purpose is to reject waste heat from a system through evaporative cooling of process water. Due to their design, a small fraction of process water is emitted from the tower exit, termed "spray drift." Dissolved solids contained within spray drift droplets are regulated as particulate matter emissions by the US EPA via AP-42. Here, we use a novel instrumentation package to measure particulate emissions from drift droplets at two cooling towers located at separate power plants. We find that drift droplet properties depend on the sampling position over the tower so multiple positions need to be sampled to accurately estimate emissions. We estimate 11 and 3.3 grams of particulate matter (PM) with a diameter < 10 µm

(PM_{10}) are emitted from each tower per hour, with 78% and 87% of PM_{10} emissions also qualifying as PM with a diameter < 2.5 µm ($PM_{2.5}$). AP-42 overestimates PM_{10} emissions by a factor of 2.4 for one tower and nearly 300 for the other. These results suggest that AP-42 may require revision to both accurately reflect lower PM_{10} emissions and account for unregulated $PM_{2.5}$, which constitute the majority of emissions.

4.1 Introduction

A wet cooling tower is a specialized heat exchanger in which warm water comes into contact with air, causing evaporative cooling of the water. Their primary function is to cool water used in industrial processes, power plants, and in heating, ventilation, and air conditioning systems. High demand for waste heat rejection has resulted in the extensive use of cooling towers across the globe, with more than two million cooling towers estimated to be operational in the United States alone (National Academies of Sciences Engineering and Medicine 2020). In order to maximize the rate of evaporation, the water is dispersed into the air within the tower as a spray. Ideally, cooling tower emissions only comprise warmed, humidified air. However, in reality a number of mechanisms lead to a small fraction of the spray droplets also being emitted from the tower, termed “spray drift”. These drift droplets can impact local and regional air quality, and so the EPA regulates their emissions via AP-42 (EPA 1995). The California Emission Inventory and Reporting System, overseen by the California Air Resources Board, estimates that 2017 emissions of PM_{10} from cooling towers in California were on the order of 2.9 tons/day. This is roughly equivalent to exhaust emissions from approximately 18 million passenger vehicles (Hellstrom and Ivarson 2008).

In this study, measurements are conducted at induced-draft counterflow wet cooling towers (Fig. 4.1), although our methodology could be applied to all types of wet cooling towers. An axial fan located at the top of the tower pulls ambient air into the tower through slots located near the bottom. The air then flows through the rain zone, the fill zone, and the spray zone. Warm water is pumped to the top of the tower and distributed by a system of spray nozzles to a lattice-structured fill material. The fill material increases the surface area of the water to allow for maximum contact with the passing air. The water then falls from the bottom of the fill zone into the rain zone and is deposited into a basin. When the water comes into contact with air in all three zones, there is mass and heat transfer which cools the water via evaporation, while warming and moistening the air. Approximately 10-20% of heat transfer takes place in the rain zone, while the remainder occurs in the fill zone (Kröger 2004).

For small droplets, the updraft velocity may exceed the terminal settling velocity in which case these droplets will be entrained into the air stream and potentially exit the top of the tower as a drift droplet. To minimize this loss, drift eliminators between the axial fan and the spray nozzles reduce the number of droplets exiting the tower with the air stream, mainly through inertial impaction. However, drift eliminators are not 100% effective and some droplets still exit the tower. Modern drift eliminators are rated to have an efficiency of $5 \times 10^{-4}\%$, defined as the percentage of circulating water which leaves the system as spray drift. Drift droplets typically evap-

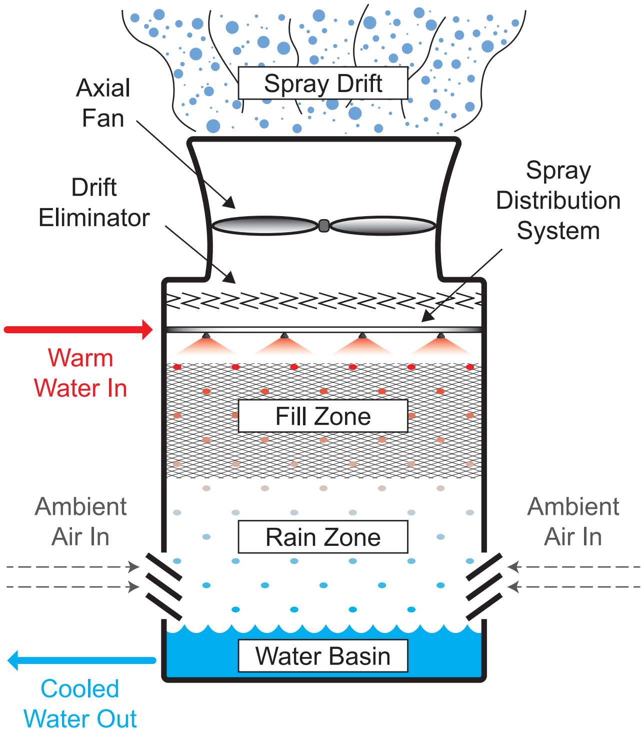
Spray Drift
Axial Fan
Drift Eliminator
Spray Distribution System
Warm Water In
Fill Zone
Ambient Air In
Rain Zone
Ambient Air In
Water Basin
Cooled Water Out

Figure 4.1: Schematic of an induced-draft counter flow cooling tower.

orate upon leaving the tower and any impurities present in the droplets remain in the atmosphere as suspended PM.

Despite the small fraction of recirculating water that is lost as drift, PM emissions may be considerable and cooling tower operators may need to purchase emission reduction credits to offset emissions. In the United States, the emission of PM_{10} from cooling towers is calculated using the methodology described by the EPA in AP-42 (EPA 1995). This regulation does not distinguish between PM_{10} and $PM_{2.5}$. This method of estimating PM_{10} emissions is based on decades old measurements (Kinsey 1991), considered “conservatively high” and is given the lowest level of acceptable confidence by the EPA (EPA 1995). AP-42 estimates PM_{10} emissions from wet cooling towers as the product of the total liquid drift factor and the total dissolved solid (TDS) concentration in recirculating water. It assumes that all droplets evaporate before being deposited onto the ground and that all drift droplets produce particles that can be classified as PM_{10}, regardless of droplet size and TDS concentration. EPA (1995) also neglects the potential scrubbing effect of cooling towers, which is the process by which PM suspended in the ambient air passing through the tower is washed out in the rain and fill zones and thereby removed from the ambient air.

PM emissions from wet cooling towers depend on the size distribution of drift droplets and the concentration of TDS in the water. Studies seeking to characterize the size distribution of drift droplets have found inconsistent results (Meroney 2006), likely due to diversity in cooling tower design and/or uncertainty in measurement techniques. Large drift droplets with high TDS concentrations may produce particles with diameters greater than 10 µm upon evaporating and therefore do not qualify for emission regulation. Two previous studies (Reisman and Frisbie 2002; Micheletti 2006) both conclude that EPA (1995) neglected to account for this effect, potentially overestimating PM_{10} emissions by 85% or more. Ruiz et al. (2013) measured the size distribution of drift droplets exiting an experimental forced draft cooling tower using a sensitive paper technique. They found that the methods outlined in EPA (1995) overestimate PM_{10} emissions by about an order of magnitude. In this study, we seek to quantify PM_{10} and $PM_{2.5}$ emissions by collecting *in situ* measurements of drift droplets as they exit wet cooling towers using high-accuracy, modern instrumentation.

4.2 Methods

4.2.1 Instrumentation and Deployment

In order to directly measure PM emissions, we constructed an instrument package designed to be lifted and held in place by crane about a meter above a cooling tower. The instrumentation package is capable of sampling wet and dry emissions in the plume above the tower. Wallis et al. (2022) describe in detail the entire instrument package. We describe next specific aspects of this package most relevant to this study.

Wet emissions, i.e. drift droplets, were sampled *in situ* using a phase-Doppler interferometer (PDI). This instrument relies on phase-Doppler interferometry, a well-established technique which has been described in great detail in the literature (e.g., Bachalo 1980; Bachalo and Houser 1984; Davis and Schweiger 2002; Chuang et al. 2008) and used extensively in the spray sciences and cloud microphysics communities. A PDI measures the size and velocity of liquid water droplets between 0.5 and 2500 µm in diameter. Droplets passing through the instrument's detection region, consisting of two intersecting laser beams, act as a lens and project an image of the interference pattern produced by the two beams. A small droplet will act as a lens with large curvature and project a larger image than a large drop. Multiple detectors measure the phase shift of the projected image which has a linear relationship to droplet size. Droplet velocity is derived with high accuracy from the frequency of the scattered signal from any one of the detectors. For more information on how a PDI derives these values, see Chuang et al. (2008). To generate droplet size distributions, the volume of air sampled by the

PDI must be accurately determined. For this, we follow methods outlined in Chapter 2 in determining probe volume diameter and use the theoretical probe volume width as instrument probe volume width was not characterized prior to this study. Plume updraft velocity, V_{up}, is determined by averaging the velocities of all droplets for each position sampled. Our estimate for V_{up} does not account for the terminal velocity of the droplets, but this contributes at most a 1% bias. Once droplet size distributions have been generated, various population level statistics can be calculated, such as median volume diameter (MVD), the median droplet size of the volume distribution, droplet number concentration (N_d), the number of droplets in a given volume of air, and liquid water content (LWC), the integrated mass of drift droplets in a given volume of air. Temperature and relative humidity probes were installed alongside the PDI to measure plume conditions in situ and a standard meteorological package measuring temperature, relative humidity, wind speed and direction was used to measure ambient conditions at a nearby location uninfluenced by the cooling tower.

The described instrumentation package was deployed above cooling towers located at two separate California power plants; "Tower 1," located in Northern California, and "Tower 2," located in Southern California. Table 4.1 provides a summary of some of the properties relevant to drift emissions for each tower. The described sampling unit was deployed above each tower at a height of ~ 1 meter above the tower exit.

	Tower 1	Tower 2
Construction year	2004	1957
Fan diameter	10 m	4 m
Nominal outlet diameter	11.5 m	4 m
Specified nominal air flow rate	800 m^3/s	220 m^3/s
Measured air flow rate	570 m^3/s	45 m^3/s
Specified circulating water flow rate	1.1 m^3/s	0.32 m^3/s
Specified drift eliminator efficiency	0.0005%	0.2%
Measured water TDS	1230 ppm	433 ppm

Table 4.1: Summary table of cooling tower properties relevant to drift emissions.

4.2.2 Estimation of PM Emissions

To estimate PM_{10} and $PM_{2.5}$ emissions from drift droplets at each tower, we (a) measure the drift droplet size distribution at various locations across the tower outlet; (b) convert the wet droplet size distribution to a dry PM emission rate at each location; and (c) integrate PM emissions over all locations to generate a total emissions rate from the tower. Characterization of recirculating tower water is critical to prediction of tower emissions. To determine the TDS concentration of recirculating water, we collected samples of recirculating water from each tower for later chemical analysis. An estimated 1-2% of recirculating water is lost to evaporation as it cycles through the tower and must be replenished with makeup water that is supplied by a variety of sources. This evaporation results in constantly increasing TDS concentration in the recirculating water since dissolved solids are not lost during evaporation and only a relatively small amount is lost in spray drift. To manage TDS, towers must undergo blowdown, where recirculating water is purged and replaced with makeup water. High TDS may result in increased emissions as well as precipitation and buildup of minerals inside the tower.

To convert wet droplet sizes to dried particle sizes, we make the following assumptions:

1. Drift droplets contain the same TDS concentration as source water.
2. Each drift droplet produces a single dry, spherical particle upon evaporating.
3. The density of the resultant dry particle is 2.6 g/cm3, which was determined by averaging salt densities from the major anions and cations in the TDS analysis. We estimate that this value is within ±0.2 g/cm3.
4. Drift droplets evaporate entirely before leaving the facility fence line.

To generate a representative size distribution for the entire tower, we sampled at positions transiting from one edge of the stack to the other, crossing over the center. Figure 4.2 shows an example of the positions sampled across the top of the tower. We assume that droplet measurements at each location are representative of half of the annulus in which that position is located or, in the case of the center position, the entire center circle. We then generate a size distribution representative of emissions from the entire tower by averaging measurements at each position, weighting for both area and V_{up}. The total flowrate Q_{tot} of the tower is computed as:

$$Q_{tot} = \sum_{j=1}^{m} A_j V_{up,j} \tag{4.1}$$

where j represents each position (all of which are half-annular in shape except for the middle position), and A_j is the area of that position.

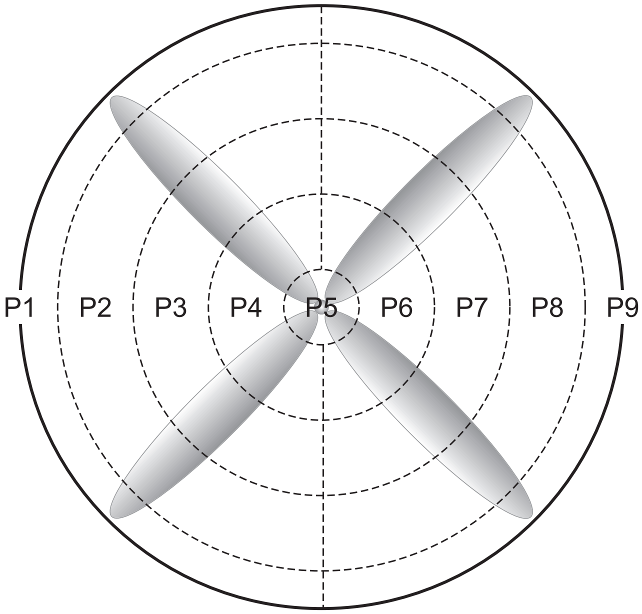

Figure 4.2: Bird's-eye view of idealized positions sampled over a cooling tower. Each position, denoted P1-P9, is assumed to represent the emissions for the area in which that position is bounded by dashed lines.

To compute a tower-averaged wet drift droplet size distribution $\overline{n}(D_p)$, we weight the size distributions measured at each position $n_j(D_p)$ by the flowrate at that position:

$$\overline{n}(D_p) = \frac{1}{Q_{tot}} \sum_{j=1}^{m} A_j V_{up,j} n_j(D_p) \tag{4.2}$$

We note that we use $\overline{n}(D_p)$ interchangeably with dN/dlogD_p in the text and figures. From the wet droplet size distribution, we can calculate a dry PM$_{10}$ mass emission rate E_{10} (in units of mass per unit time) as:

$$E_{10} = Q_{tot} \cdot \int_0^{10\,\mu m} \frac{\pi}{6} D_p^3 c_{TDS} \overline{n}(D_p) dD_p \tag{4.3}$$

where c_{TDS} is the TDS concentration (units of mass of TDS per volume of water). A similar equation with different integration limits is used for dry PM$_{2.5}$ emission rates.

For Tower 1, we sampled at nine positions, as shown in Fig. 4.2, sampling at each position for 3 minutes in the north to south direction. We also sampled at two additional positions, slightly outside of the stack and equidistant from P1 and P9, but recorded no drift droplets in these positions. For Tower 2, we employed a similar sampling technique as shown in Fig. 4.2, but with seven positions instead of nine, due to the smaller size of the stack and in the east-by-northeast to west-by-southwest direction. Each position at Tower 2 was sampled for 5 minutes. Localized regions of both uncharacteristically high and uncharacteristically low drift emissions likely occur at tower outlets. Because only a limited number of samples were collected at each tower, the described sampling technique likely neglects to account for these localized regions. For future studies, we plan to refine the sampling strategy to obtain drift droplet size distributions which account for these localized regions and more closely represent cooling tower emissions.

4.3 Results and Discussion

4.3.1 Plume Measurements

In collecting measurements during transits across each tower, we observed a strong radial dependence on the measured drift droplet properties. Figures 4.3 and 4.4 show how V_{up}, MVD, LWC, and N_d varied radially for Towers 1 and 2, respectively. Tower radius was nondimensionalized for better comparison between the two towers.

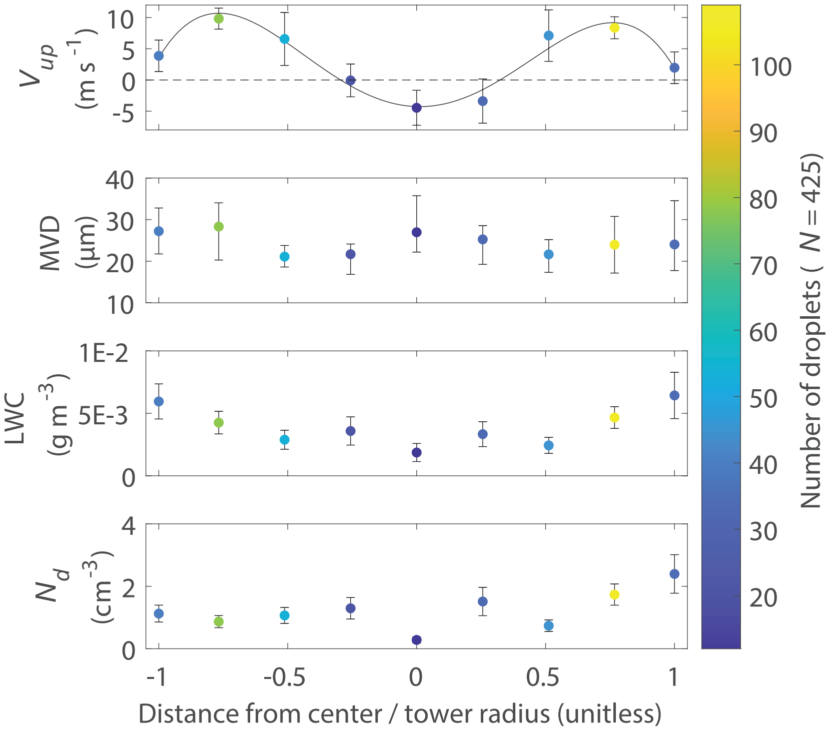

Figure 4.3: Radial dependence of measured properties for Tower 1. Color bars and corresponding colored points represent the frequency of droplets encountered at each position, for each tower, with N total droplets observed at each tower. Error bars in the first row represent ± one standard deviation in V_{up} and the solid line represents a 4th-degree polynomial fit to the points. Error bars in the second row represent the 25th and 75th percentiles of median volume diameter at each position. Error bars in the third and fourth rows represent error in liquid water content and number concentration, respectively, relating to Poisson counting uncertainty for each position.

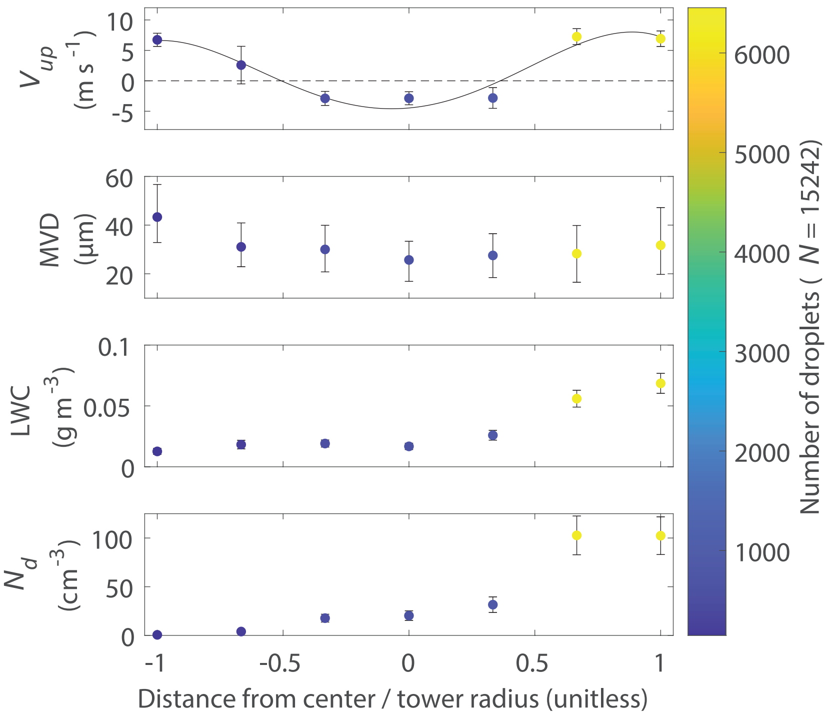

Figure 4.4: Radial dependence of measured properties for Tower 2. Color bars and corresponding colored points represent the frequency of droplets encountered at each position, for each tower, with N total droplets observed at each tower. Error bars in the first row represent ± one standard deviation in V_{up} and the solid line represents a 4th-degree polynomial fit to the points. Error bars in the second row represent the 25th and 75th percentiles of median volume diameter at each position. Error bars in the third and fourth rows represent error in liquid water content and number concentration, respectively, relating to Poisson counting uncertainty for each position.

One feature in Figs. 4.3 and 4.4 is that the updraft velocity at each tower becomes negative (i.e. air flows downwards) near the center of the tower. This is a known feature of axial fans, and results in negative PM emissions towards the center of the tower, i.e. particles enter rather than exit the tower. We also noticed an asymmetry in all other properties across the tower where one might expect symmetry in these properties. These asymmetries are more notable in Tower 2 compared to Tower 1. Because Tower 2 is much older than Tower 1, these asymmetries may be the result of inadequacy in tower design and/or poor maintenance of drift eliminators causing buildup of mineral and regions of localized emissions.

From a droplet emissions perspective, the two towers look very different from each other. Both the liquid water content and number concentration are approximately an order of magnitude larger in the second tower compared to the first. This can likely be attributed to differences in tower design such as the type of drift eliminators installed, spray nozzle design, number and orientation of fan blades, fan speed, and water recirculation rate. Also, mineral buildup in the internal components of the tower can impact the size distribution of drift droplets and thus drift eliminator efficiency. Environmental factors such as relative humidity, wind speed, and wind direction may also impact these properties, as will be discussed in Section 4.3.2.

4.3.2 Environmental Conditions During Sampling

Environmental conditions at the time of sampling have the potential to impact measurements and compromise assumptions. Table 4.2 summarizes the environmental conditions averaged over the sampling period for each tower. Reported error represents ± one standard deviation for each of the described values. Mean and standard deviation of the ambient wind azimuth angle was calculated using methods outlined in Yamartino (1984). Large standard deviation reported in the plume updraft velocity is due to the strong radial dependence of this property. Due to a malfunction in the ambient relative humidity and temperature sensors during sampling of Tower 1, values reported represent meteorological data from the nearest weather station. We would like to note that the ambient temperature reported here is higher than the measured plume temperature. This is not consistent with the physical processes by which cooling towers operate and is likely due to temperature discrepancies between the site location and weather station.

	Tower 1	Tower 2
Ambient temperature	28.9°C*	22.8±0.4°C
Ambient relative humidity	19%*	75.5±1.2%
Wind Speed	2.5±0.9 m/s	2.0±1.0 m/s
Wind azimuth angle	218±29°	188±39°
Plume temperature	27.9±0.3°C	28.4±0.3°C
Plume relative humidity	98.9±2.7%	100.7±0.2%
Plume updraft velocity	5.5±4.2 m/s	3.6±4.4 m/s

Table 4.2: Summary table of environmental and plume conditions averaged over the sampling period for each tower.
*data reported by nearest weather station

We first examine the potential for wind speed and direction to influence the measurements. Wind speed and direction can influence the trajectory of the plume to a degree that increases with distance from the tower exit. Figure 4.5 shows wind roses from data acquired during the sampling period as well as the direction of transit across each tower, as indicated by the circled arrows in the lower right corner of each plot. Wind conditions were relatively calm during sampling at each tower, averaging

2.5 m/s and 2.0 m/s for Towers 1 and 2, respectively, with gusts never exceeding 4 m/s and 5 m/s for each respective tower. Mean wind speed was 45% of updraft velocity for Tower 1 and 55% of updraft velocity for Tower 2. Because measurements were taken very near to the tower outlet, $\sim$ 1 meter above, ambient wind likely influenced the trajectory of the plume by approximately 0.5 m relative to the tower outlet. Thus wind likely did not play a large role in the uncertainty of measurements obtained. Furthermore, two additional positions were sampled outside of the Tower 1 outlet, approximately 1.4 m from the north and south edges. No droplets were detected in either position, supporting the claim that wind did not significantly influence the trajectory of the plume prior to samples being collected. In Tower 2, we observed an asymmetry in LWC and N_d (Fig. 4.4) that could potentially be attributed to wind. However, increases in both LWC and N_d were observed on the west-by-southwest side of the tower and prevailing winds had a strong southwesterly component, especially during sampling where these higher values were observed. Therefore, if winds were to cause the asymmetry in these properties, one would expect a pattern opposite of the observations. This further supports the claim that asymmetries observed in Tower 2 are due to tower design and upkeep rather than environmental factors.

Differences in temperature and relative humidity between the plume and environment also have the potential to influence the measurements as they may cause droplets to change size. As a moist plume rises and cools, water vapor will condense onto existing droplets causing them to grow. However, because samples were collected approximately 1 m above the tower outlet and cooling is very small over this distance,

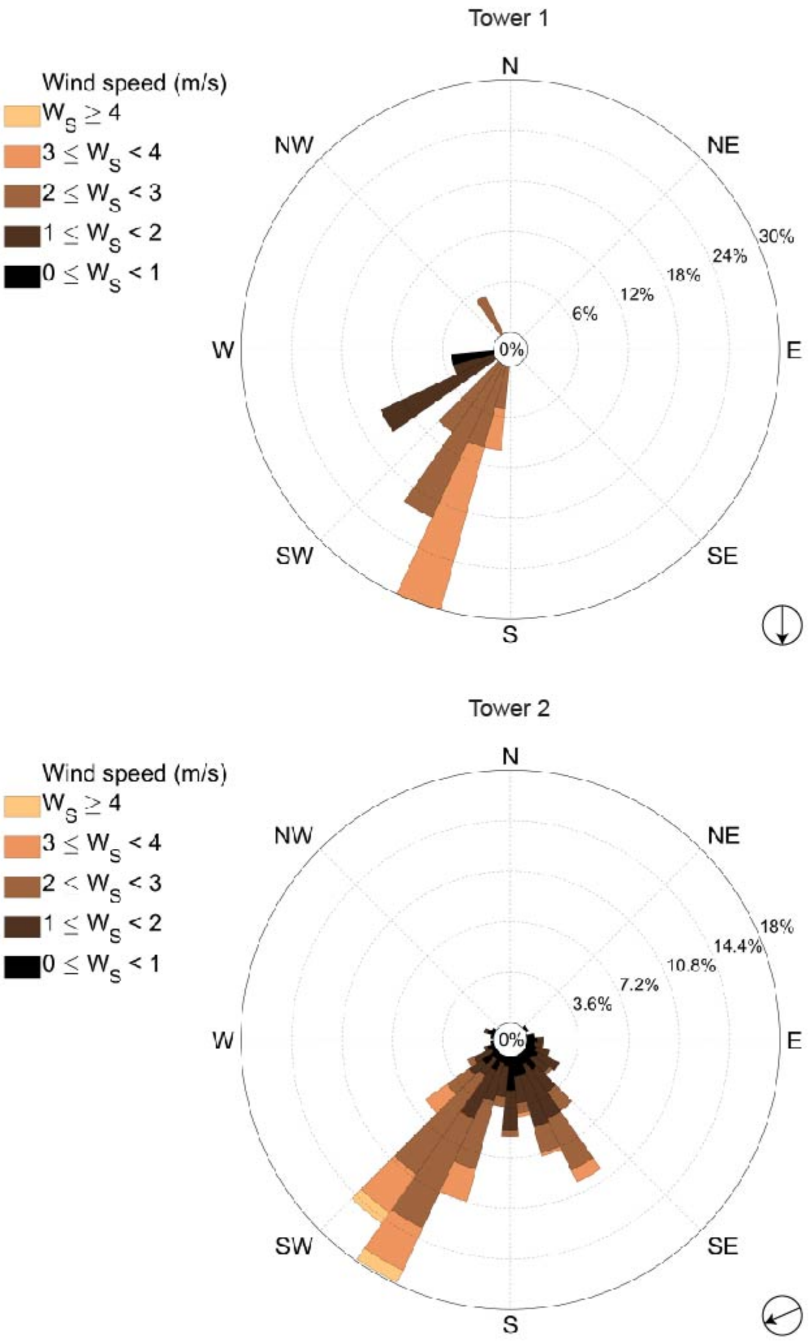

Figure 4.5: Wind roses during sampling for each tower. Wind direction is indicating where the wind originates, concentric circles indicate the frequency of wind, and the color scale on the left-hand side indicates wind speed. The direction of transit across each tower is indicated by the circled arrow in the lower right of each plot.

condensational growth of droplets due to adiabatic cooling is considered negligible. Growth of droplets due to collision-coalescence is unlikely to impact our measurements considering the low droplet number concentrations observed and proximity of the sampling unit to the tower outlet. If droplet growth by collision-coalescence does occur however, parent droplets would contain the same concentration of TDS and would produce a droplet with an identical TDS concentration, which is not of concern. Entrainment near the edges of the plume will bring ambient, typically drier air into the plume causing evaporation and a decrease in droplet size. However, if evaporation of droplets due to entrainment significantly impacted the measurements, one would expect a decrease in LWC near the edges of the towers. There is no evidence of entrainment in Tower 1 as Fig. 4.3 shows an increase in LWC near the edges of the tower. As previously noted, Tower 2 exhibits an asymmetry in LWC so the same case cannot be made here. However, environmental conditions at Tower 2 were likely less favorable for entrainment (e.g., slower plume updraft velocity and wind speed) and evaporation (e.g., higher relative humidity) so it is unlikely that evaporation due to entrainment significantly impacted the measurements obtained.

4.3.3 Comparison with Previous Studies

A representative size distribution of drift droplets was estimated for each tower from our measurements, and then compared to size distributions presented in previous studies (Fig. 4.6). The solid black line in Fig. 4.6 represents test data presented in Reisman and Frisbie (2002) provided by Brentwood Industries, a drift eliminator

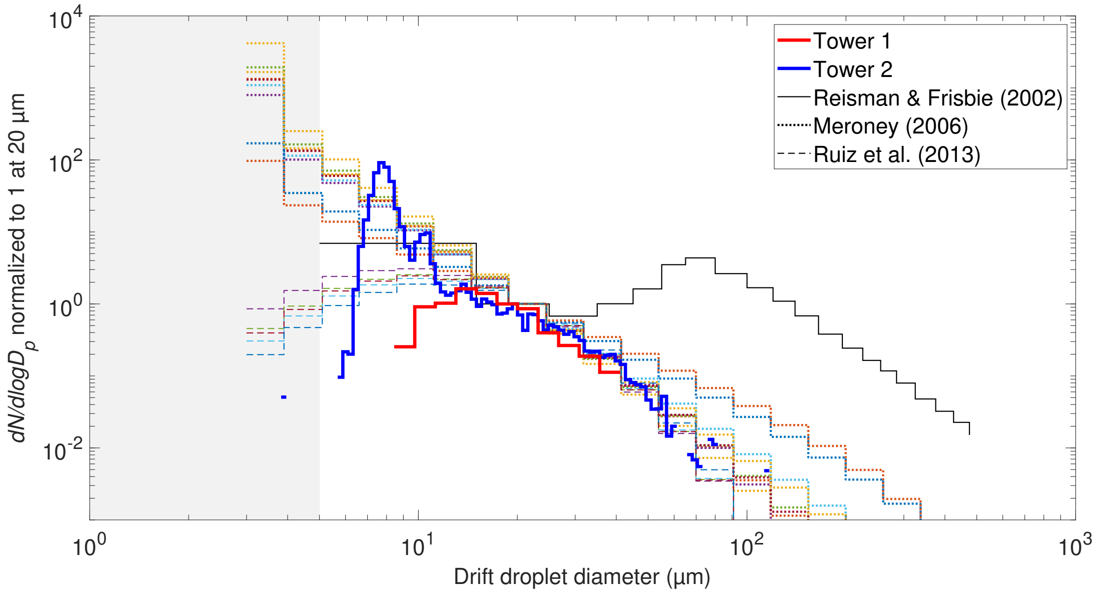

Figure 4.6: Representative size distribution for drift droplets at each tower compared to size distributions reported in previous studies.

manufacturer. Colored dotted lines were reconstructed using mean droplet diameters and shape parameters for Rossen-Rammler mass distributions as reported by Meroney (2006). These parameters were fitted to data collected at seven mechanical draft cooling towers, one natural draft cooling tower, and one idealized case. Colored dashed lines were reconstructed using mean droplet diameters and standard deviations for log-normal mass distributions as reported by Ruiz et al. (2013). These parameters were fitted to experimental data from five repeated tests on a mechanical draft cooling tower using the sensitive paper technique for measuring droplet size distributions. Ruiz et al. (2013) found the log-normal function to be the most suitable fit to the experimental data collected, hence it is shown here. For better comparison, each distribution has been normalized by bin width and to a dN/dlogD_p value of 1 at a droplet diameter of 20 µm. This normalization permits easier comparison of the shapes of the size distributions. Our measurements for Towers 1 and 2 are presented with different size bin widths because the lower number of droplets measured in Tower 1 requires larger bins to have the same counting statistics. The gray area in the background of Fig. 4.6 represents the size range in which assumptions inherent to the PDI begin to break down, thus decreasing our confidence in the measurements obtained. The size distribution representative of each tower closely resembles certain ones described by Meroney (2006) and Ruiz et al. (2013), but with distributions peaking at slightly different sizes. The distribution reported by Reisman and Frisbie (2002) exhibits a second mode in the droplet size range of 70-80 µm, a feature not observed in any other distribution. This feature led Reisman and Frisbie (2002) to suggest that PM_{10} emissions could be decreased by increasing TDS concentrations in order to generate PM larger than 10 µm. This finding is not consistent with our measurements. Meroney (2006) suggests that drift droplet size distributions may be bimodal, with the second peak occurring at larger droplet sizes, due to "inadequacies in design or subsequent maintenance of drift eliminators." We did not see any evidence of bimodality in either of the towers surveyed.

4.3.4 Drift Eliminator Efficiency

From our measurements, we can compute the drift eliminator efficiency of each tower and compare these values to manufacturer specifications. We use the representative size distributions derived by our measurements along with the water recirculation rate for each tower as specified by the manufacturer (refer to Table 4.1 for water recirculation rate). For Tower 1, our measurements suggest a drift eliminator efficiency of 0.00021%, roughly a factor of 2.4 better than the reported nominal efficiency of 0.0005%. For Tower 2, we estimate a drift eliminator efficiency of 0.00068%, an estimate more consistent with values reported for modern drift eliminators and roughly 300 times better than the reported value of 0.2%. These calculations assume that the water recirculation rate is that from the tower specifications. If the actual flow rate is lower than specified, then our estimates of drift eliminator efficiency should be increased proportionally.

4.3.5 PM Emissions from Drift

We estimate PM_{10} and $PM_{2.5}$ emission rates for each tower using the derived size distributions along with measured TDS concentrations (Fig. 4.7). Vertical dashed lines represent the drift droplet size threshold in which droplets smaller than this value would produce $PM_{2.5}$ upon evaporating. All drift droplets produce PM_{10} upon evaporating, as the threshold for producing PM with a diameter greater than 10 µm is $\sim$ 128 µm and $\sim$ 182 µm for Towers 1 and 2, respectively, and no droplets greater than these sizes were observed. Our measurements suggest that the large majority of drift droplets produce $PM_{2.5}$ upon evaporating, with 78% and 87% of the total PM_{10} emissions qualifying as $PM_{2.5}$ emissions for Towers 1 and 2, respectively. Assuming that the towers are operated continuously at the capacity measured, emissions of PM_{10} at Towers 1 and 2 are estimated as 11 and 3.3 g/hr, respectively, and emissions of $PM_{2.5}$ are 8.3 and 2.9 g/hr, respectively. These emission rates are for a single cooling tower cell only. Typical power plants will have a number of cooling tower cells. If we normalize emissions by the concentration of TDS in recirculating water, emissions for each of the two towers look remarkably similar. Towers 1 and 2 have emission rates of 8.6×10^{-3} and 7.7×10^{-3} grams of PM_{10} per hour per unit TDS, respectively. Because these two towers have major design and operational differences, more measurements are needed to determine if this similarity is meaningful or coincidental.

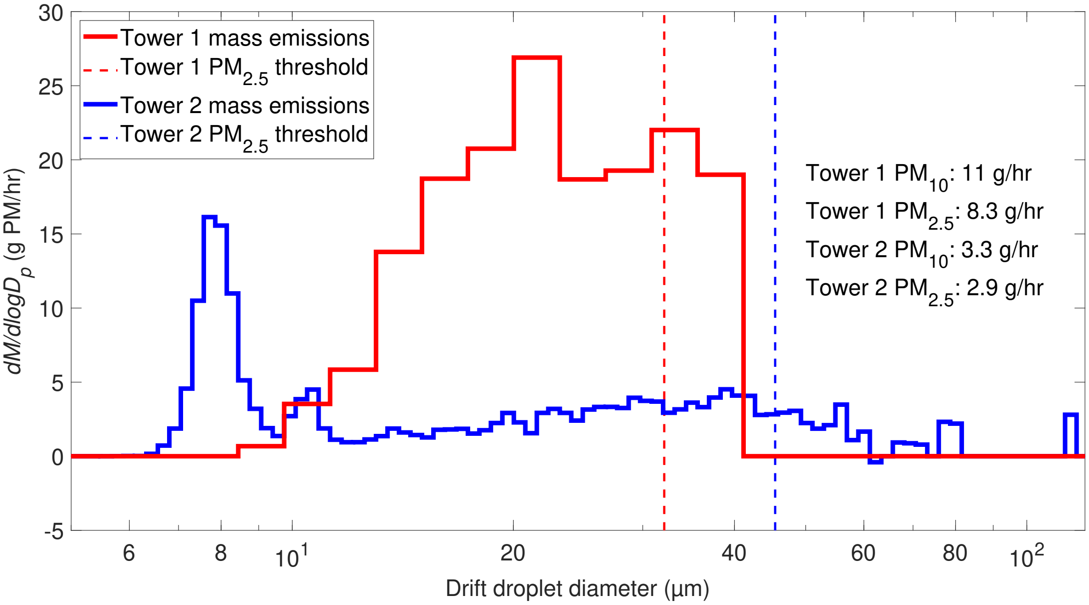

Figure 4.7: PM emission rate from drift droplets for each tower as a function of drift droplet diameter. Vertical dashed lines represent the threshold for drift droplets which would produce $\mathrm{PM}_{2.5}$ upon evaporating based on measured TDS concentration at each respective tower. Total PM_{10} and $\mathrm{PM}_{2.5}$ emission rates are summarized in text.

Currently the EPA only regulates PM_{10} emissions from cooling towers but our measurements show that the majority of these emissions count as $\mathrm{PM}_{2.5}$. This suggests that both PM_{10} and $\mathrm{PM}_{2.5}$ emissions should be considered when regulating cooling tower emissions.

Some assumptions are made in estimating these emissions. These calculations use the estimated dry particle density of 2.6 g/cm3. Based on the species comprising TDS, this estimated density is likely to be within ±10% of the actual value. Also, EPA regulations specify that emissions are counted at the fence line and therefore any droplets that settle to the ground before reaching the boundary of the property are not considered emissions. From our measured drift droplet diameters, the maximum realistic settling velocities are a few centimeters per second. Given typical wind speeds and distances to the fence line, these drift droplets will fall at most a few meters before exiting the property. Since typical wet cooling towers are at least 10 meters tall and the drift emissions have an initial upward velocity, it is safe to assume that almost all droplets should be considered emissions.

Next, we compare the PM_{10} emissions rates estimated for each tower to that which would be calculated using methods outlined in EPA (1995). For Tower 1, we find that EPA (1995) overestimates the PM_{10} emission rate by 140%. This overestimate is similar in magnitude to previous studies (Reisman and Frisbie 2002; Micheletti 2006). For Tower 2, the emission rate calculated using methods outlined in EPA (1995) would represent an overestimate of approximately 29,000% - a value many orders of magnitude larger than what's been reported in previous studies. The main reason for the large discrepancy between measurements and the EPA estimate for Tower 2 emissions is the large value for the drift efficiency of Tower 2. Tower 1 has a value of 0.0005%, which is typical of modern drift eliminators. In contrast, the drift efficiency of Tower 2 was specified as 400 times larger, 0.2%, a value typical of drift eliminators during the time of tower construction. However, our estimate for drift eliminator efficiency for Tower 2 suggests drift eliminators at this tower are performing much better than specified and are operating with a similar efficiency as modern drift eliminators. This implies the possibility that other drift eliminators are also performing much better than specified, with commensurate discrepancies in the estimated emissions. While our findings agree with previous research that EPA (1995) grossly overestimates PM_{10} emissions, we find that the reason for that overestimation differs from previous studies. Reisman and Frisbie (2002) and Micheletti (2006) argue that EPA (1995) overestimates emissions due to the false assumption that all drift droplets produce PM_{10} upon evaporating. Their hypothesis is not consistent with our results as our measurements suggest that nearly all droplets would produce PM_{10} upon evaporating. Instead, we find that EPA (1995) overestimates emissions because they overestimate the mass flux of droplets exiting the tower.

Reisman and Frisbie (2002) suggests that increasing the TDS of recirculating water could result in PM emissions larger than 10 µm upon drift droplet evaporation, producing PM emissions that would not qualify as PM_{10}. TDS concentrations would need to increase ~ 30 fold and ~ 4 fold in each respective tower before even the largest droplets observed would produce particles larger than 10 µm. However, increasing TDS concentrations to these values would proportionally increase PM_{10} emissions for all other droplets. In order to ultimately decrease PM_{10} emissions, TDS concentrations would need to be increased to unreasonably high values ($\sim 10^3$ increase to near equal parts TDS and water) so that the increase in PM_{10} due to higher TDS is offset by the a decrease in PM_{10} due to particles exceeding this size range. Therefore, increasing

TDS is not an effective strategy for decreasing PM_{10} emissions in either of the towers sampled.

4.4 Summary and Conclusions

In this study, we report particulate emissions from two cooling towers using measurements from a novel instrument package (Wallis et al. 2022). The most relevant instrument for this study is the phase-Doppler interferometer (Chuang et al. 2008), which measures the ambient wet diameter of drift droplets, as well as their velocity. By locating the PDI at different positions across the cooling tower outlet, total tower drift emissions can be computed. There is strong radial dependence of spray drift droplet properties so it is important to sample at various places across the tower outlet for accurate emission estimates.

We find that the measured drift droplet emissions for Tower 1 suggests that drift eliminator efficiency is roughly a factor of 2.4 better than the drift eliminator specifications, while for Tower 2, this value is 300 fold better than specifications. Water TDS values are combined with the measured size distribution to estimate PM_{10} and $\mathrm{PM}_{2.5}$ emissions (which, by definition, are dried particles), which for Tower 1 are 11 and 8.3 g/hr, respectively, while for Tower 2 are 3.3 and 2.9 g/hr, respectively. EPA AP-42 overestimates PM_{10} emissions by 140% for Tower 1 and nearly 29,000% for Tower 2. The large discrepancy for Tower 2 is due to drift eliminators performing much more efficiently than specified. This implies the possibility that emissions estimates from other cooling towers experience a similar degree of overestimation, further highlighting the need for direct measurements. Cooling tower $PM_{2.5}$ emissions are not regulated, but our measurements suggest that they can be a large fraction of total particulate emissions, suggesting that regulation may be needed. Previous research has suggested that purposefully increasing TDS may result in the particulate emissions to be larger than PM_{10}, and thus be outside the regulated size range. The results from these two towers imply that this strategy would require $\sim 10^3$ increases in TDS which is unrealistic.

Chapter 5

Summary and Conclusions

The research presented in this dissertation first focuses on improving probe volume characterization techniques through simulations, laboratory and aircraft measurements. We then present an emerging PDI application in which the instrument is used to estimate particulate matter (PM) emissions from drift droplets at two cooling towers.

In Chapter 2, we develop an automated method for characterizing PDI probe volume diameter, D_{beam}, which varies with drop size, d, empirically from *in situ* measurements. Our method of determining $D_{beam}(d)$ relies on fitting the cumulative distribution function (CDF) of transit lengths, $l_{transit}$, for each d bin. We first present a "Standard algorithm" used to characterize $D_{beam}(d)$ when the PDI is operating as theory predicts. Next, we describe situations in which PDI behavior deviates from theory, resulting in gate chop and short gate events, and present an alternative algorithm to account for these occurrences. We apply the Standard algorithm to data collected in a controlled laboratory setting and to flight measurements and find very good agreement between the results of our methods and theoretical prediction, providing confidence that our Standard algorithm produces accurate results and can be successfully applied to aircraft observations. Next we apply the alternative algorithm, which accounts for the presence of gate chop and short gate events, to flight data which exhibited deviations from theoretical behavior. We find that our methods work well and that frequent gate chop and short gate events do not significantly impact our ability to characterize $D_{beam}(d)$. We then assess $D_{beam}(d)$ variability for three field campaigns. Our results suggest that modest daily variability can occur, highlighting the importance of automated $D_{beam}(d)$ characterization. Lastly, we test the robustness and accuracy of our methods using artificially-generated, noisy data. These tests suggest that our algorithms are very robust and accurate to within 1%.

In Chapter 3, our focus shifts towards characterizing PDI probe volume width, W, which has typically been assumed to be a known fixed value based on the optical configuration of the system, which we denote as W_c. Theoretical calculations are performed and suggest that W is not a fixed value but exhibits a dependence on d for small drops. Inspired to explore this in further detail, we design and construct an instrument which traverses a stream of monodisperse drops along the probe volume so that direct measurements may be obtained. We present a new independent variable, the maximum intensity as a drop passes through the most intense portion of the probe volume, I_{max}, to be used as a metric for W and accounts for changes in detector gain. We then measure W directly in a controlled laboratory setting for each channel of a dual-range PDI. We find the I_{max} provides a well-constrained relationship with W and that W is not a fixed value, confirming the prediction of our theoretical calculations. We also measure W greater than W_c in Channel 2 and attribute this to the existence of a blur circle due to poor focus of the receiving optics which allows drops to be detected outside the spatial range dictated by the aperture. This further highlights the importance of direct W measurement. Lastly, we process data from one flight of a recent field campaign and find very good agreement in the overlap region between the two channels. Because the only similarity shared between the two channels is the housing unit and the laser, each channel may be regarded as a separate instruments. Agreement between channels provides confidence the our methods for characterizing W yield accurate results. Furthermore, measurements collected in the overlap region of Channel 1 are considered highly accurate so the fact that Channel 2 concurs with Channel 1 in this region further increases our confidence in the methods.

Lastly, we present a new emerging PDI application in Chapter 4 in which the instrument is used to measure PM emissions from drift droplets at two separate cooling towers. In this work, we suspend the PDI above each cooling tower and collect measurements of drift droplets emissions at discrete locations across the top of each tower to obtain representative size distributions of drift droplets. We find that the location at which samples are collected greatly impact our measurements so careful consideration must be given to sampling locations. We then use the total dissolved concentration (TDS) of source water and volumetric flow of each tower to convert the measured distributions to PM emission rates. While the EPA only regulates emissions of PM with diameter of < 10 μm (PM_{10}), we find that the majority of PM emissions have a diameter of < 2.5 μm ($PM_{2.5}$) in both towers. When comparing our measured emission rates to what would be estimated using methods outlined by the EPA, we find that the EPA grossly overestimates PM_{10} emissions. Our findings suggest that the EPA estimates of PM emissions may require revision to both reflect lower PM_{10} emission and account for unregulated $PM_{2.5}$ emissions.

Bibliography

Albrecht, H.-E., N. Damaschke, M. Borys, and C. Tropea (2013). *Laser Doppler and phase Doppler measurement techniques.* Springer Science & Business Media.

Bachalo, W. D. and M. J. Houser (1984). "Phase/Doppler Spray Analyzer For Simultaneous Measurements Of Drop Size And Velocity Distributions". In: *Optical Engineering* 23.5.

Bachalo, W. and M. Houser (1987). "Spray drop size and velocity measurements using the phase/Doppler particle analyzer". In: *International Journal of Turbo and Jet Engines* 4.3-4, pp. 207–216.

Bachalo, W. and S. Sankar (1996). "Phase Doppler particle analyzer". In: *The Handbook of Fluid Dynamics, CRC, Idaho Falls*, pp. 37–1.

Bachalo, W. D. (1980). "Method for measuring the size and velocity of spheres by dual-beam light-scatter interferometry". In: *Applied Optics* 19.3, p. 363.

Baker, B., Q. Mo, R. P. Lawson, D. O'Connor, and A. Korolev (2009a). "Drop Size Distributions and the Lack of Small Drops in RICO Rain Shafts". In: *Journal of Applied Meteorology and Climatology* 48.3, pp. 616–623.

Baker, B., Q. Mo, R. P. Lawson, D. O'Connor, and A. Korolev (2009b). "The Effects of Precipitation on Cloud Droplet Measurement Devices". In: *Journal of Atmospheric and Oceanic Technology* 26.7, pp. 1404–1409.

Baumgardner, D. and A. Korolev (1997). "Airspeed Corrections for Optical Array Probe Sample Volumes". In: *Journal of Atmospheric and Oceanic Technology* 14.5, pp. 1224 –1229.

Baumgardner, D. and M. Spowart (1990). "Evaluation of the Forward Scattering Spectrometer Probe. Part III: Time Response and Laser Inhomogeneity Limitations". In: *Journal of Atmospheric and Oceanic Technology* 7.5, pp. 666 –672.

Bony, S. and J.-L. Dufresne (2005). "Marine boundary layer clouds at the heart of tropical cloud feedback uncertainties in climate models". In: *Geophysical Research Letters* 32.20.

Bony, S. et al. (2017). "EUREC4A: A Field Campaign to Elucidate the Couplings Between Clouds, Convection and Circulation". In: *Surveys in Geophysics* 38.6, pp. 1529–1568.

Brenguier, J. L. (1989). "Coincidence and Dead-Time Corrections for Particles Counters. Part II: High Concentration Measurements with an FSSP". In: *Journal of Atmospheric and Oceanic Technology* 6.4, pp. 585 –598.

Brenguier, J. L., D. Baumgardner, and B. Baker (1994). "A Review and Discussion of Processing Algorithms for FSSP Concentration Measurements". In: *Journal of Atmospheric and Oceanic Technology* 11.5, pp. 1409 –1414.

Chuang, P. Y., E. W. Saw, J. D. Small, R. A. Shaw, C. M. Sipperley, G. A. Payne, and W. D. Bachalo (2008). “Airborne Phase Doppler Interferometry for Cloud Microphysical Measurements”. In: *Aerosol Science and Technology* 42.8, pp. 685–703.

Coelho, A. A., J.-L. Brenguier, and T. Perrin (2005). “Droplet Spectra Measurements with the FSSP-100. Part II: Coincidence Effects”. In: *Journal of Atmospheric and Oceanic Technology* 22.11, pp. 1756–1761.

Davis, J. E. and G. Schweiger (2002). “The airborne microparticle : its physics, chemistry, optics, and transport phenomena”. In: Berlin New York: Springer, p. 833. ISBN: 9783540433644.

Dye, J. E. and D. Baumgardner (1984). “Evaluation of the Forward Scattering Spectrometer Probe. Part I: Electronic and Optical Studies”. In: *Journal of Atmospheric and Oceanic Technology* 1.4, pp. 329 –344.

EPA, U. S. (1995). “AP-42, Compilation of Air Pollutant Emission Factors”. In: *Stationary Point and Area Sources* 1.

Gardiner, B. A. and J. Hallett (1985). “Degradation of In-Cloud Forward Scattering Spectrometer Probe Measurements in the Presence of Ice Particles”. In: *Journal of Atmospheric and Oceanic Technology* 2.2, pp. 171 –180.

Hellstrom, E and M Ivarson (2008). “Average annual emissions and fuel consumption for gasoline-fueled passenger cars and light trucks”. In: *United States Environment Protection Agency.*

Jackson, T. A. (1990). *Droplet sizing interferometry.* ASTM International.

Kinsey, J. S. (1991). *Development Of Particulate Emission Factors For Wet Cooling Towers*. Tech. rep. Midwest Research Institute.

Korolev, A. V., E. F. Emery, J. W. Strapp, S. G. Cober, G. A. Isaac, M. Wasey, and D. Marcotte (2011). "Small Ice Particles in Tropospheric Clouds: Fact or Artifact? Airborne Icing Instrumentation Evaluation Experiment". In: *Bulletin of the American Meteorological Society* 92.8, pp. 967–973.

Korolev, A. (2007). "Reconstruction of the Sizes of Spherical Particles from Their Shadow Images. Part I: Theoretical Considerations". In: *Journal of Atmospheric and Oceanic Technology* 24.3, pp. 376–389.

Korolev, A. and G. A. Isaac (2005). "Shattering during Sampling by OAPs and HVPS. Part I: Snow Particles". In: *Journal of Atmospheric and Oceanic Technology* 22.5, pp. 528–542.

Kröger, D. G. (2004). *Air-cooled heat exchangers and cooling towers*. Vol. 1. PennWell Books.

Lance, S., C. A. Brock, D. Rogers, and J. A. Gordon (2010). "Water droplet calibration of the Cloud Droplet Probe (CDP) and in-flight performance in liquid, ice and mixed-phase clouds during ARCPAC". In: *Atmospheric Measurement Techniques* 3.6, pp. 1683–1706.

Lance, S. (2012). "Coincidence Errors in a Cloud Droplet Probe (CDP) and a Cloud and Aerosol Spectrometer (CAS), and the Improved Performance of a Modified CDP". In: *Journal of Atmospheric and Oceanic Technology* 29.10, pp. 1532–1541.

Lawson, R. P. (2011). “Effects of ice particles shattering on the 2D-S probe”. In: *Atmospheric Measurement Techniques* 4.7, pp. 1361–1381.

Lee, H.-C. (1990). “Review of image-blur models in a photographic system using the principles of optics”. In: *Optical Engineering* 29.5, pp. 405 –421.

Lu, M.-L., W. C. Conant, H. H. Jonsson, V. Varutbangkul, R. C. Flagan, and J. H. Seinfeld (2007). “The Marine Stratus/Stratocumulus Experiment (MASE): Aerosol-cloud relationships in marine stratocumulus”. In: *Journal of Geophysical Research: Atmospheres* 112.D10.

Malinowski, S. P., H. Gerber, I. J.-L. Plante, M. K. Kopec, W. Kumala, K. Nurowska, P. Y. Chuang, D. Khelif, and K. E. Haman (2013). “Physics of Stratocumulus Top (POST): turbulent mixing across capping inversion”. In: *Atmospheric Chemistry and Physics* 13.24, pp. 12171–12186.

Matheou, G., D. Chung, L. Nuijens, B. Stevens, and J. Teixeira (2011). “On the Fidelity of Large-Eddy Simulation of Shallow Precipitating Cumulus Convection”. In: *Monthly Weather Review* 139.9, pp. 2918–2939.

Medeiros, B., B. Stevens, and S. Bony (2014). “Using aquaplanets to understand the robust responses of comprehensive climate models to forcing”. In: *Climate Dynamics* 44.7-8, pp. 1957–1977.

Medeiros, B., B. Stevens, I. M. Held, M. Zhao, D. L. Williamson, J. G. Olson, and C. S. Bretherton (2008). “Aquaplanets, Climate Sensitivity, and Low Clouds”. In: *Journal of Climate* 21.19, pp. 4974–4991.

Meroney, R. N. (2006). “CFD prediction of cooling tower drift”. In: *Journal of Wind Engineering and Industrial Aerodynamics* 94.6, pp. 463–490.

Micheletti, W (2006). “Atmospheric emissions from evaporative cooling towers”. In: *CTI JOURNAL* 27.1, p. 60.

Miks, A. and J. Novak (2012). “Dependence of camera lens induced radial distortion and circle of confusion on object position”. In: *Optics Laser Technology* 44.4, pp. 1043–1049. ISSN: 0030-3992.

Morrison, H. et al. (2020). “Confronting the Challenge of Modeling Cloud and Precipitation Microphysics”. In: *Journal of Advances in Modeling Earth Systems* 12.8.

National Academies of Sciences Engineering and Medicine (2020). *Management of Legionella in Water Systems*. Washington, DC: The National Academies Press. ISBN: 978-0-309-49947-7.

Reisman, J. and G. Frisbie (2002). “Calculating realistic PM10 emissions from cooling towers”. In: *Environmental Progress* 21.2, pp. 127–130.

Ruiz, J., A. Kaiser, M. Ballesta, A. Gil, and M. Lucas (2013). “Experimental measurement of cooling tower emissions using image processing of sensitive papers”. In: *Atmospheric Environment* 69, pp. 170–181.

Sankar, S., A. Inenaga, and W. Bachalo (1993). “Trajectory dependent scattering in phase Doppler interferometry: minimizing and eliminating sizing errors”. In: *Laser Techniques and Applications in Fluid Mechanics*, pp. 75–89.

Sankar, S., B. Weber, D. Kamemoto, and W. Bachalo (1991). "Sizing fine particles with the phase Doppler interferometric technique". In: *Applied Optics* 30.33, pp. 4914–4920.

Sezan, M. I., G. Pavlovic, A. M. Tekalp, and A. T. Erdem (1991). "On modeling the focus blur in image restoration." In: *ICASSP*. Vol. 91, pp. 2485–2488.

vanZanten, M. C. et al. (2011). "Controls on precipitation and cloudiness in simulations of trade-wind cumulus as observed during RICO". In: *Journal of Advances in Modeling Earth Systems* 3.2, n/a–n/a.

Vial, J., J.-L. Dufresne, and S. Bony (2013). "On the interpretation of inter-model spread in CMIP5 climate sensitivity estimates". In: *Climate Dynamics* 41.11-12, pp. 3339–3362.

Vivirito, P., S. Battiato, S. Curti, M. L. Cascia, and R. Pirrone (2002). "Restoration of out-of-focus images based on circle of confusion estimate". In: *Applications of Digital Image Processing XXV*. Ed. by A. G. Tescher. Vol. 4790. International Society for Optics and Photonics. SPIE, pp. 408 –416.

Wallis, C. D., M. D. Leandro, P. Y. Chuang, and A. S. Wexler (2022). "An instrument for direct measurement of emissions: cooling tower example". In: *Atmospheric Measurement Techniques* 15.8, pp. 2547–2556.

Wang, C. (1988). "Laser Doppler velocimetry". In: *Journal of Quantitative Spectroscopy and Radiative Transfer* 40.3. Special Issue on Quantitative Spectroscopy and Laser Diagnostics, pp. 309–319. ISSN: 0022-4073.

Webb, M. J. et al. (2006). “On the contribution of local feedback mechanisms to the range of climate sensitivity in two GCM ensembles”. In: *Climate Dynamics* 27.1, pp. 17–38.

Wendisch, M. and J.-L. Brenguier, eds. (2013). *Airborne Measurements for Environmental Research*. Wiley.

Wood, R, C. Mechoso, C. Bretherton, R. Weller, B Huebert, F Straneo, B. Albrecht, H Coe, G Allen, G Vaughan, et al. (2011). “The VAMOS ocean-cloud-atmosphere-land study regional experiment (VOCALS-REx): Goals, platforms, and field operations”. In: *Atmospheric Chemistry and Physics* 11.2, pp. 627–654.

Wu, W. D., K. C. Patel, S. Rogers, and X. D. Chen (2007). “Monodisperse Droplet Generators as Potential Atomizers for Spray Drying Technology”. In: *Drying Technology* 25.12, pp. 1907–1916. eprint: `https://doi.org/10.1080/07373930701727176`.

Yamartino, R. J. (1984). “A Comparison of Several “Single-Pass” Estimators of the Standard Deviation of Wind Direction”. In: *Journal of Climate and Applied Meteorology* 23.9, pp. 1362–1366.